PROBING THE SPATIOTEMPORAL DYNAMICS OF RAS GTPASES ON THE CELL MEMBRANE WITH HIGH-THROUGHPUT SINGLE-MOLECULE MICROSCOPY

By

Yerim Lee

A DISSERTATION

Presented to the Department of Biomedical Engineering and the Oregon Health & Science University School of Medicine in partial fulfillment of the requirements for the degree of

DOCTOR OF PHILOSOPHY
September 2019

School of Medicine

Oregon Health & Science University

Certificate of Approval

This is to certify that the Ph.D. Dissertation of

Yerim Lee

"*Probing the spatiotemporal dynamics of Ras GTPases on the cell membrane with high-throughput single-molecule microscopy*"

Has been approved

_____

Mentor: Xiaolin Nan, Ph.D

_____

Member/Chair: Philip Stork, MD

_____

Member: Daniel Zuckerman, Ph.D

_____

Member: Laura Heiser, Ph.D

_____

Member: Joe Gray, Ph.D.

_____

Member: Xubo Song, Ph.D

Contents

Chapter 1

Introduction

1.1 Ras Biology

1.1.1 Ras in cell signaling and cancer

Rat sarcoma viral oncogene homolog (Ras) proteins are important signaling molecules ubiquitously expressed in eukaryotes and are key regulators of normal proliferation and differentiation [1]. The Ras family is a group of small GTPases that reside on the membrane and are involved in multiple cell signaling cascades [2, 3] (Figure 1.1.1).

They transmit growth signals from cell surface receptors, such as tyrosine kinase receptors, by switching between GTP or GDP bound states [4]. Ras is inactive when GDP bound, but stimulation by upstream factors results in the exchange of GDP for GTP with the aid of guanine exchange factors (GEFs). GTP bound Ras is able to bind and recruit downstream effectors to the membrane. Although Ras is able to hydrolyze GTP to GDP, the endogenous reaction is slow and is catalyzed by GTPase-activating proteins (GAPs). A third of all human cancers have a constitutively active Ras mutation, making Ras one of the most frequently mutated oncogenes [2, 3, 5]. Oncogenic Ras mutations are single base substitutions that stabilize GTP-bound state which results in constitutive activation of Ras and its target proteins, leading to several hallmarks of cancer [3, 5].

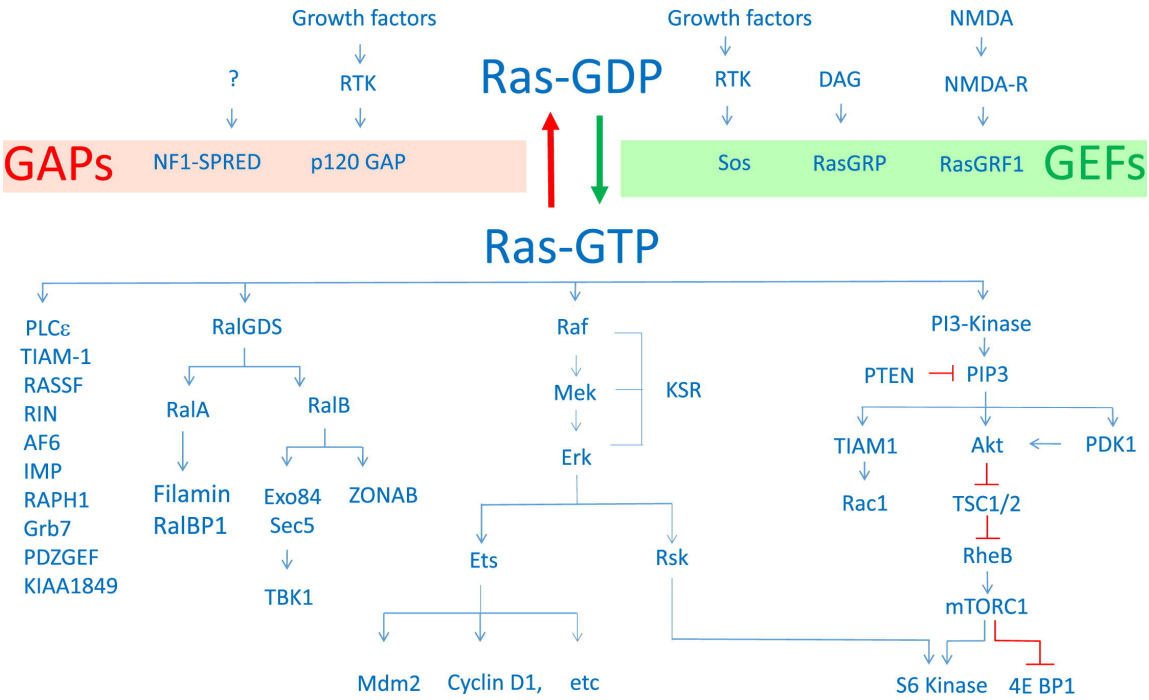

Figure 1.1.1: Ras Signaling Pathways. Reprinted from [2].

Although the Ras proteins are involved in multiple cascades, the mitogen-activated protein kinase (MAPK) pathway is frequently mutated in cancer and is a major driver of cancer progression [2, 3, 5]. The MAPK cascade is an evolutionarily conserved signaling pathway that transmits extracellular signals to the nucleus resulting in changes to the transcriptome [3, 5] (Figure 1.1.2). Located downstream of receptor tyrosine kinases, such as the epidermal growth factor receptor, components of the Ras-MAPK pathway include rapidly accelerated fibrosarcoma (RAF), MAPK kinase (MEK) and extracellular signal-regulated kinase (ERK). Each kinase recruits and activates its substrate via phosphorylation [3, 5]. This culminates in phosphorylated ERK (pERK) that translocates into the nucleus and activates multiple transcription factors resulting in the regulation of cell proliferation, differentiation, migration and apoptosis. Although the biochemical aspects of this pathway have been relatively well studied, recent work suggests that spatial regulation is also a critical step in Ras activation.

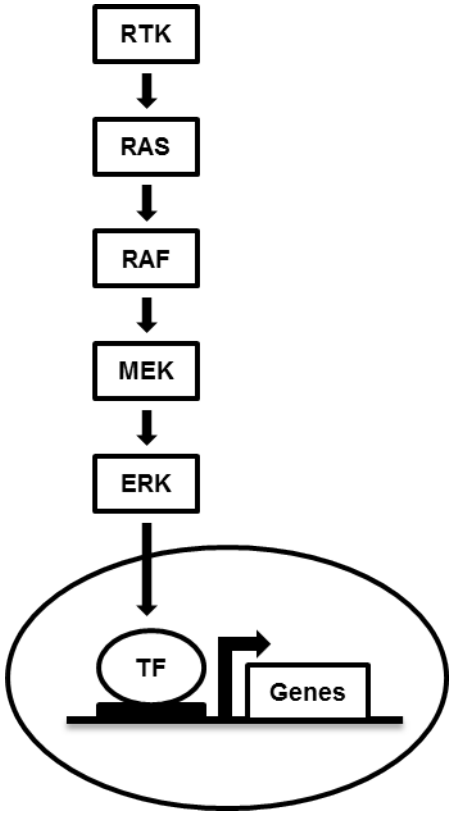

Figure 1.1.2: Simplified MAPK Pathway. Ligand bound receptor tyrosine kinases (RTKs), i.e. epidermal growth factor receptor bound to the epidermal growth factor, activate RAS and change the cell transcriptome.

1.1.2 Isoform specific Ras properties and biological activity

The Ras superfamily is mainly divided into five major branches (Ras, Rho, Rab, Ran and Arf) based on functional and sequence similarity [6, 7]. All Ras are small GTP-binding proteins that function as signal transducers that propagate signals initiated by some environmental stimuli [6, 7, 8]. The most well-known human oncogenes within the Ras subfamily are the three RAS genes (K, H and N) that function as transducers and propagators of multiple signaling pathways [2, 3]. KRas further has two different splice variants, KRas 4A and KRas 4B, with the latter being the most highly expressed splice variant. Although the Ras isoforms are highly conserved,

especially in the effector binding G domain region, they have different biological functions. For example, KRas knock out is embryonic lethal while H and NRas are not [2]. In addition, there are significant differences in the presence of the isoforms in human cancers [2, 3]. KRas mutation is much more frequent than N or HRas, and the mutation rates also differ by cancer types. Almost all pancreatic cancers exhibit KRas mutation while NRas is the most common Ras mutation in melanoma. Further, Ras GTPases are known to activate over 20 different signaling pathways, but Ras isoforms have different preferences for different signaling pathways [9, 8]. For example, KRas primarily activates MAPK while the PI3K pathway is activated more strongly by HRas [10, 8]. Although the mechanism is unclear, these differences indicate that Ras isoforms have distinct biological functions.

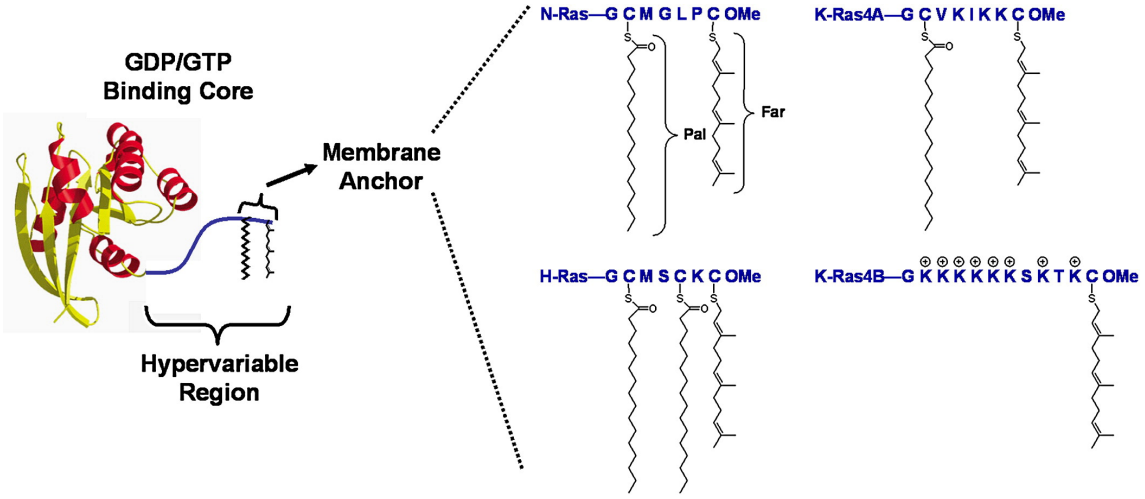

Figure 1.1.3: Ras Isoform Structural Differences. Reprinted from [11]

Ras is composed of two regions, the G domain and the hypervariable region (HVR) (Figure 1.1.3) [2, 11, 8, 12, 13]. The G domain is the catalytic domain that is responsible for the loading and the hydrolysis of GTP [2, 11, 8, 12, 13]. The structure of the G domain of the Ras isoforms is virtually identical and almost all of the structural differences come from the HVR [2, 12, 13, 11, 8]. The hypervariable region, located at the C-terminal end of Ras, undergoes post-translational lipid modications that results in dierent lipid tails for each isoform [2, 11, 13, 12, 8]. Two palmitoyl

chains and a farnesyl chain are appended to the HRas tail [2, 13, 12, 11, 8]. NRas and KRas 4A both are modified with the addition of one palmitoyl and a farnesyl chain respectively, while KRas 4B is farnesylated and contains six lysine residues that interact with the negatively charged phospholipids to facilitate KRas 4B interaction with the membrane (Figure 1.1.3). Given the prevalence of KRas 4B, KRas will be used to refer to KRas 4B from here on.

1.1.3 Role of the membrane in isoform-specific Ras biology

Due to their structural and functional variability, it was hypothesized that the Ras isoforms have non-redundant biological functions with the largest structural difference in the HVR, which contains the membrane targeting motif. As such, it was hypothesized that the Ras isoforms segregate to different regions of the membrane and this segregation could cause the observed diversity in Ras activated signaling pathways [9, 8].

Far from a homogenous sea of lipids, it is becoming clear that the membrane is a complicated, heterogeneous system [14, 8]. In addition to lipids and cholesterol, the membrane is crowded with proteins and carbohydrates. The picket fence model states that membrane compartmentalization is achieved by a meshwork of filamentous proteins such as actin and regular arrays of transmembrane proteins anchored to the underlying cytoskeleton that hinder lateral diffusion [14, 8]. Other features of the membrane include lipid rafts, which are hypothesized to be small membrane domains on the order of nanometers that are enriched in cholesterol, sphingolipids and lipid raft associated proteins, such as Glycosylphosphatidylinositol-anchored proteins (GPI-APs) [15, 8]. Aside from lipid rafts, there are other membrane microdomains. Caveolae invaginations are known to form their own high density microdomains with components similar to lipid rafts [16]. Another example of non-raft microdomains include pools of anionic phospholipids, such as phosphatidylserine, that interact with positively charged proteins through electrostatic interactions [17, 18, 18]. Further, there is evidence suggesting that these microdomains function as signaling platforms for membrane proteins, and that these microdomains can be either transient or sta-

ble structures [19, 20, 21]. Therefore, it is becoming evident that the membrane has an elaborate organization with many different components.

Multiple studies have shown that Ras isoforms indeed differ in their dependence on different membrane structures [22, 23, 24, 25, 26]. More specifically, GTP loaded HRas was observed to associate with lipid rafts and co-localize with caveolin, the primary component of caveolae which are involved in endocytosis [26] (Figure 1.1.4). However, HRas-GDP did not, indicating that HRas lateral segregation on the plasma

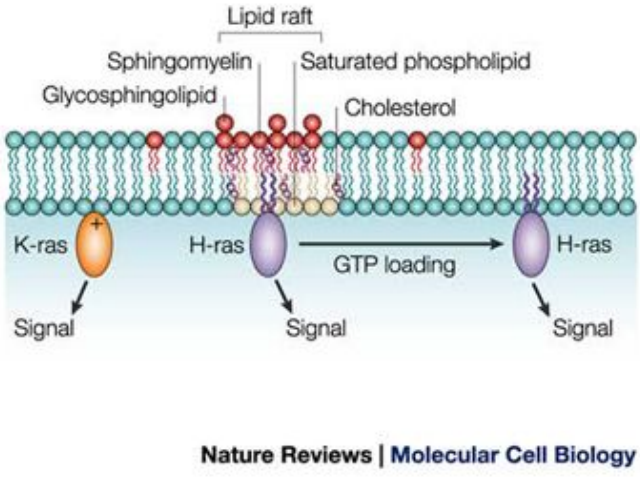

Figure 1.1.4: Ras Compartmentalization. Reprinted from [9]

membrane is dependent on its nucleotide status. In contrast, KRas resides outside of lipid rafts regardless of the bound nucleotide [26]. Further, KRas has been shown to be sensitive to actin [25], and the KRas tail, the membrane targeting motif, encodes lipid selectivity and has high affinity to phosphatidylserine [27, 28]. Phosphatidylserine, an anionic lipid that is relatively abundant on the inner leaflet of the membrane, forms immobile and mobile pools in the membrane [29, 18]. As such, it is hypothesized that KRas segregates to these phosphatidylserine pools on the membrane.

1.2 Ras Dimers and Clusters in Signaling

1.2.1 Protein clusters on the membrane

Clustering of membrane proteins is proving to be a ubiquitous mechanism [30]. A diverse set of membrane bound proteins, from signaling to immune receptors, have been observed to form clusters [30]. GPI-APs are lipid-linked extracellular proteins that are involved in a range of functions including signal transduction, cell adhesion and endocytosis. Chemical crosslinking and fluorescence resonance energy transfer (FRET) revealed that GPI-APs form oligomers of at most four molecules [30]. This was observed for multiple GPI-AP species. Lymphocyte function-associated antigen-1 and CD209, transmembrane proteins involved in the immune system, are also known to form large nanoclusters [30]. In addition, well studied signaling proteins such as the members of the ERBb family are also known to form transient, reversible dimers on the membrane where the dimerization is a necessary step for the activation of the intracellular tyrosine kinase domain [31]. The prevalence of protein clusters across biological functions begs the question of its necessity. Some potential explanations include allosteric regulation of the receptor oligomers or increasing the dwell time of a ligand by providing multiple ligand binding sites in close proximity [30]. It has also been suggested that nanoclusters can filter out noise in signal transduction by digitizing the continuous analog input signals, in terms of ligand binding, and preventing spurious generation of signal [32]. The recent advance of super resolution imaging has allowed for a more in-depth investigation of protein oligomerization as an organizing principle.

1.2.2 Ras dimers and clusters on the membrane

The clustering behavior of Ras was first described by Prior and colleagues in an immuno-EM study where Ras formed clusters of 6-8 Ras molecules [26]. These Ras nanoclusters were further characterized in a follow-up paper [32]. In this study, about 60% of the Ras molecules on the membrane existed as monomers, while the other 40% existed as nanoclusters. Importantly, it was shown that monomeric Ras

did not interact with RAF, concluding that Ras clustering was necessary for signal transduction [32] and that KRas scaffold protein galectin-3 is a necessary component of nanoclusters [33]. Further, the Hancock lab was able to show that H and KRas reside in different membrane compartments [23, 25]. Although showing the necessity of Ras clustering behavior in MAPK signaling was groundbreaking, the immuno-EM was performed with an overexpression of Ras ($\sim$14 fold higher expression than in a normal cell [25, 34]) due to the technical limitation of labeling efficiency of the target protein by antibody-labeled gold.

Nan et al. overcame the labeling limitations of EM by using quantitative PALM, a super resolution microscopy technique [34]. High labeling efficiency was achieved by genetically tagging KRas G12D with PAmCherry1, a photoactivatable red fluorescent protein. The construct was placed under a tetracycline promoter so that the expression of the exogenous fusion protein increased with the addition of doxycycline, a tetracycline analog [34]. This doxycycline-inducible system allowed them to express KRas GTP at physiological levels, and the resulting multimers were quantified through single-molecule counting [34]. At the physiologically relevant Ras densities of 70 Ras molecules/μm^2, dimers were the dominant cluster size and higher order multimers (3 or more Ras molecules in a cluster) were rare, implying that the dimers were the physiologically relevant Ras signaling unit [34]. The functional requirement of Ras dimers was further validated through both chemical cross-linking and Ras dimer interface inhibition [35, 36]. Inouye et al. showed that the dimerization of Ras was essential for activation of Raf [35], while Smith et al. demonstrated the necessity of KRas GTP dimers in signal transduction by preventing Ras dimer formation with a synthetic monobody [36]. Thus, multiple studies have determined that Ras dimers are the minimum necessary unit to signal downstream affectors.

1.3 Different approaches to studying spatial distribution of membrane proteins

Aside from the use of traditional biochemical assays to investigate protein oligomers, such as chemical cross-linking and western blots, several imaging techniques have been used to directly observe and probe membrane proteins.

1.3.1 Electron Microscopy

Electron microscopy (EM) has the highest spatial resolution to observe the membrane structures of a cell [37, 38]. With nanometer resolution, EM can identify various membrane structures including caveolae, clathrin coated vesicles, and actin filaments [38, 37]. In immunogold electron microscopy (immuno-EM), target proteins of interest can be visualized by labeling them with an antibody conjugated to a gold nanoparticle [37, 38]. The Hancock lab successfully applied this technique to directly characterize Ras nanoclusters on the membrane [23, 25]. They successfully mapped the spatial distribution of the Ras isoforms to different membrane compartments. Using two different sized gold nanoparticles, they also mapped the spatial distribution of H and KRas on the membrane [23, 25].

Despite providing the best spatial detail, EM is limited to only fixed cells and suffers from low immuno-gold labeling efficiency. In order to compensate for the low labeling efficiency, Ras proteins were extremely overexpressed using a CMV promoter. Aside from issues arising from protein expression, since EM is incompatible with live cells, this technique is unable to confer any dynamic information.

1.3.2 Fluorescence Microscopy

Fluorescence microscopy (FM) in many ways offers opposite advantages and disadvantages compared to EM. Unlike EM, FM has high labeling efficiency via genetic tags, is compatible with live cell imaging, and is easy to implement multiple colors. However, fluorescent probes used to label target proteins can have significant interfer-

ence on the binding kinetics and the spatial distribution of the protein [39]. Further, the spatial resolution of FM is often significantly worse, at approximately 200 nm depending on the excitation wavelength. The diffraction limit for light microscopy can be described as follows [40]:

$$\text{resolution} = \frac{\lambda}{2\text{NA}}$$

where λ is the excitation wavelength and NA is the numerical aperture. As such, protein clusters cannot be directly observed with conventional FM. For example, excitation wavelength of 550 nm would result in $\sim$ 290 nm resolution with 0.95 NA.

Fluorescence Resonance Energy Transfer (FRET)

FRET is one technique that can measure protein-protein interactions using FM [41]. FRET is a fluorescence imaging technique that relies on the transfer of energy between two fluorophores with overlapping emission and excitation wavelengths. If the two fluorophores are within a few nanometers, the emission from the donor fluorophore excites the acceptor fluorophore and the resulting emission from the acceptor fluorophore can be detected to determine the dimerization of two proteins (Figure 1.3.1).

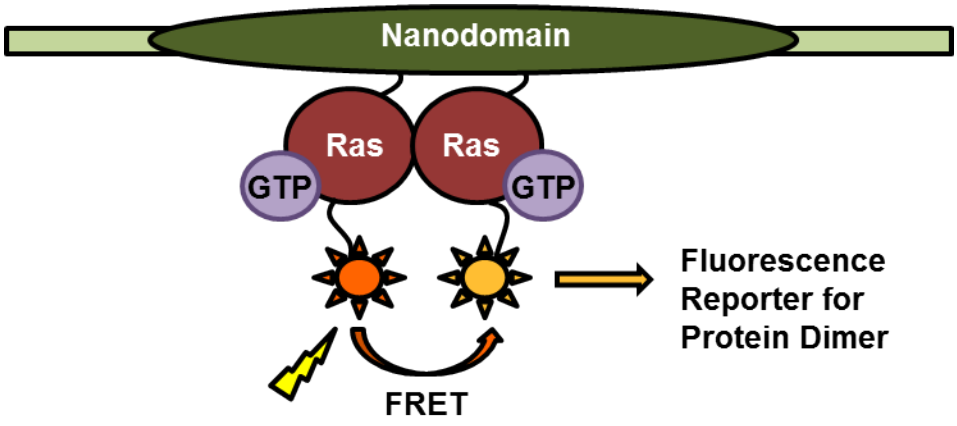

Figure 1.3.1: Detecting Protein-Protein Interactions Using FRET

This highly restricted sensing range, on the order of nanometers, makes this technique an accurate method for detecting protein protein interactions. Further, this approach is live cell compatible, and thus it is able to give dynamic information on the duration and the spatial location in addition to the frequency of cluster formation.

Super-Resolution Microscopy

Super-resolution microscopy (SRM) is a group of light microscopy techniques that can circumvent the diffraction limit of light in conventional FM [40]. In general, there are three different super-resolution methods: single molecule localization microscopy (SMLM) [42, 43], structured illumination microscopy (SIM) [44], and stimulated emission depletion (STED) [45]. The work presented in this thesis only relies on SMLM. Hence only SMLM will be covered.

SMLM consists of photoactivated localization microscopy (PALM) [43], stochastic optical reconstruction microscopy (STORM) [42], and DNA-Point Accumulation for Imaging Nanoscale Topography (PAINT) [46]. As shown in Figure 1.3.2C, in a densely labeled sample, SMLM surpasses the diffraction limit of light by spatially isolating individual fluorophores. If the point spread function (PSF) of an imaging system is known and the individual fluorophores are isolated, then super-resolution can be achieved by fitting the PSF to the diffraction limited spot of the emitter. In SMLM, fluorophores are spatially isolated by random activation of only a subset of fluorphores, such that at any given time only a small number of fluorophores are actively emitting light. In most cases, the random activation enables separation of the emitters greater than the limit of the spatial resolution (i.e. $\sim$250 nm). Thus, the locations of all of the fluorophores are imaged sequentially by acquiring a movie with hundreds to hundreds of thousands of frames.

Subdiffractive localization of individual molecules, on the order of nanometer resolution, is achieved by fitting a two-dimensional Gaussian to each point spread function (PSF) generated from a light diffracted point source (Figure 1.3.2 A). The centroid localization of the fitted 2D Gaussian determines the spatial resolution,

which depends on the number of photons collected [43, 40]:

$$\sigma_{x,y} \approx \frac{s}{\sqrt{N_{sig}}}$$

where $\sigma_{x,y}$ is the localization precision of the estimated particle position, s is the standard deviation of the Gaussian fitted to the PSF, and N_{sig} is the total number of photons. After the sample is imaged, the coordinates are extracted in the post image processing step where this function is fitted to all of the emitters in the movie. The final high resolution image is constructed using the extracted coordinates. Since the localization precision depends on the number of photons collected per emitter, a brighter fluorophore leads to improved spatial resolution.

In PALM, this is achieved by utilizing fluorescent proteins that start in the dark state and require input energy to fluoresce while STORM relies on dyes that stochastically switch between on and off states. In the case of DNA-PAINT, artificial blinking is mimicked by the kinetics of binding between the complementary DNA strands between the target protein and the dye.

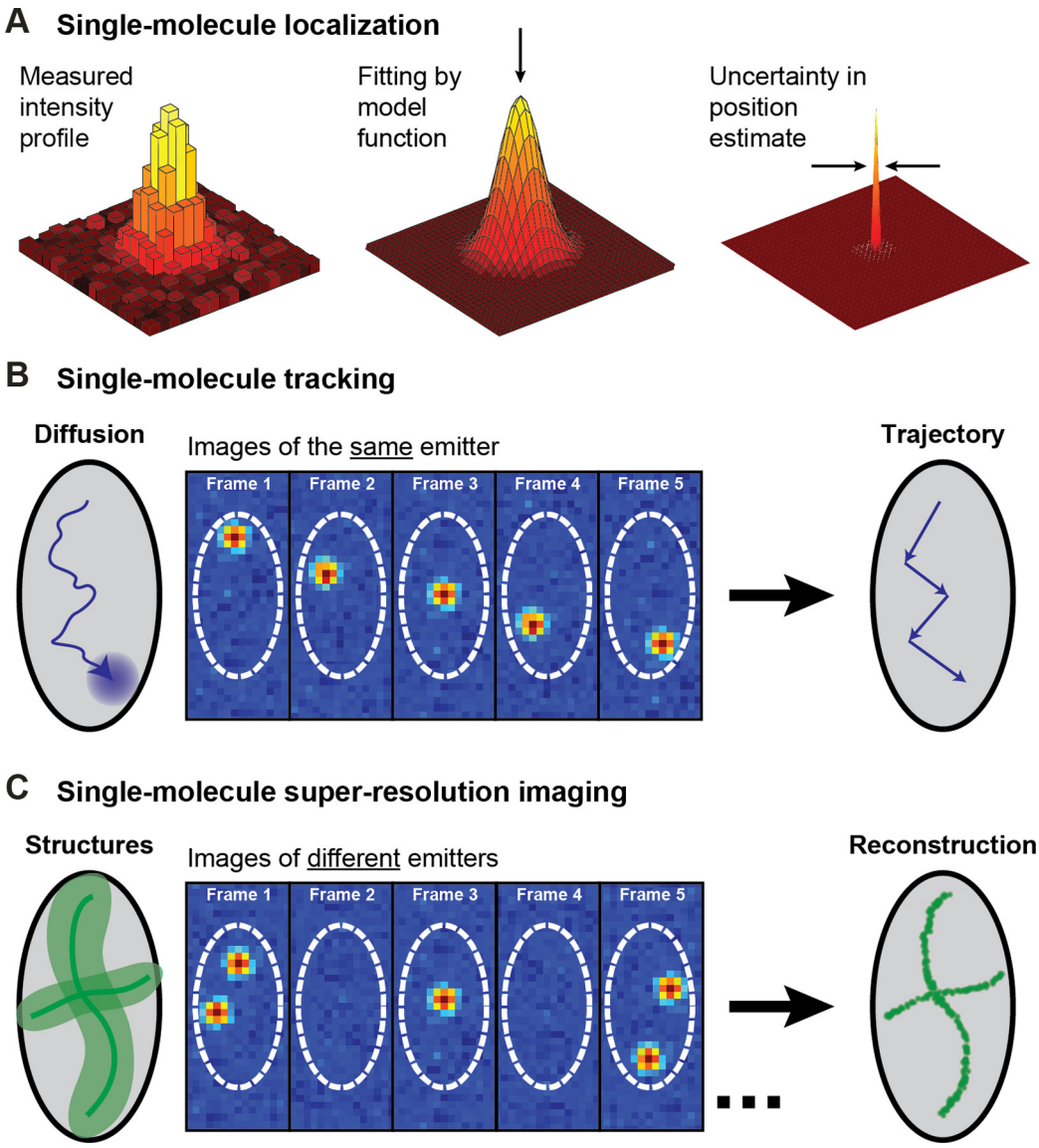

Figure 1.3.2: Single Molecule Localization Microscopy and Single Particle Tracking. Reprinted from [40]

Single Particle Tracking

Single particle tracking (SPT) is a technique that allows the measurement of dynamic information [47, 48, 14, 49, 50, 40]. More importantly, SPT is the only method that allows observation of motions of individual molecules [50, 40]. In an SPT experiment, particle motion in real time is obtained by taking a movie of the diffusing particles labeled with a fluorophore (Figure 1.3.2B). After the movie acquisition, the spatial positions for each particle are extracted and connected over time (discussed in further detail in Chapter 2). Since the coordinates must be extracted for each frame, similar to super resolution, each emitter must be spatially separated beyond the diffraction limit of light.

Traditional SPT techniques only employed a handful of fluorescent probes to prevent aggregation of multiple emitters in the same light diffracted space. This limited the acquisition of single particle trajectories to only a handful of trajectories, which limited the statistical and observational power. This limitation was overcome with sptPALM, where the technique of temporally separating single emitters in PALM was introduced to SPT to allow significantly more trajectories to be collected [51]. Similar to PALM, sptPALM relies on photoactivatable fluorescent proteins that initially start out in the dark state. Only a small number of fluorophores are activated at a time, which allows each particle position to be extracted and connected over adjacent frames. More fluorophores are activated as the current fluorophores become photobleached and the cycle is repeated until the end of the movie or until all of the fluorophores have been activated.

The analysis of the resulting single molecule tracks reflects the underlying diffusion behavior of the molecule for a given spatial location. This indirectly allows us to detect hidden underlying interactions between the tagged molecule and the membrane structure. Because SPT is a collection of individual measurements, rare and transient behavior can be detected. Through SPT the hidden interaction between a given protein and its spatiotemporal interaction with the membrane can be modeled.

1.3.3 Analysis of Single Particle Tracking Data

While there are multiple methods for analyzing single particle tracking data, we will focus on three different methods: calculating the mean square displacement (MSD), fitting a cumulative distribution function (CDF), and applying the variational Bayes single particle tracking (vbSPT) method.

Mean Squared Displacement

The probability density function (PDF) for the one-dimensional position of a particle as a function of time is given by the following [52]:

$$p(x,t) = \frac{1}{\sqrt{4\pi Dt}} \exp\left(-\frac{(x-x_0)^2}{4Dt}\right)$$

where x is the coordinate after time lag t, x_0 is the starting coordinate at time 0 and D is the diffusion coefficient. The variance of the above PDF is the MSD [48, 52, 50]:

$$\text{MSD} = 2nDt$$

where D is the diffusion coefficient, n is the number of dimensions, and t is the time interval. The MSD measures the variation in the position of a particle as a function of the time interval.

Assuming brownian motion, this is a simple method that has been used widely to extract the diffusion coefficient from the single particle trajectories. To plot the MSD, the average displacement is calculated for each time lag.

$$\text{MSD} = \frac{1}{N}\sum_{n=1}^{N}(x_n(t) - x_n(0))^2$$

where N is the number of particles, $x_n(t)$ is the starting position of that particle at time t, and $x_n(0)$ is the initial starting position of particle. To determine the diffusion coefficient of a molecule undergoing random motion, the slope of the plot of MSD over time can be divided by $2n$ (where n is the number of dimensions) [52].

Unfortunately, this approach is limited to simple diffusion where the slope of the MSD curve is linear. Nonlinear curves at short time scales indicate anomalous diffusion [52]. The following MSD functions can be fitted for two-dimensional diffusion:

$$\begin{aligned} \text{MSD} &= 4Dt && \text{normal diffusion} \\ \text{MSD} &= 4Dt^{\alpha} && \text{anomalous diffusion} \end{aligned}$$

where D is the diffusion coefficient, t is the time lag, and $\alpha > 1$ indicates superdiffusion and $\alpha < 1$ indicates subdiffusion. Although straightforward and easy to implement, MSD cannot separate different diffusion modes. For example, if a particle displayed slow and fast diffusion, MSD analysis will aggregate both diffusion modes into a single diffusion coefficient [52].

CDF fitting for a mixture model

One way to infer different number of diffusion states, their corresponding occupancies, and diffusion coefficients is by fitting a mixture model to the data.The PDF for a single diffusion state is known. We can fit the functional form of a mixture of distributions for each diffusion state to the observed step size distribution to obtain the mixture coefficients (occupancies) and the corresponding diffusion coefficients for a given number of diffusion states. For a 2D particle undergoing brownian motion, the probability density function for a given displacement vector is given by the following [53, 54, 48, 55]:

$$P(\vec{r}, t) = \frac{1}{4\pi Dt} \exp\left(\frac{-\vec{r}^{\,2}}{4Dt}\right)$$

The PDF for a given scalar displacement of size, r, can be derived by integrating over all angles.

$$\text{PDF}(r, t) = \int_{\theta=0}^{2\pi} P(\vec{r}, t)\, d\vec{r} = \frac{r}{2Dt} \exp\left(\frac{-r^2}{4Dt}\right)$$

$$\text{CDF}(r, t) = \int_{0}^{r} PDF(r, t)\, dr = 1 - \exp\left(\frac{-r^2}{4Dt}\right)$$

The CDF for more than one diffusion coefficient is given by the following [54, 56]:

$$\text{CDF}(r,t) = 1 - \sum_{i=1}^{n} \alpha_i \exp(\frac{-r^2}{4D_i t})$$

where α is the fraction or occupancy corresponding to each diffusion coefficient.

Although technically the histogram of the step sizes can be fitted to the PDF to determine the corresponding diffusion coefficient, the quality of the histogram depends on the size of the bins [53]. However, the empirical CDF, by definition, does not depend on bins ($F_n = \frac{1}{n}\sum_{i=1}^{n} \mathbb{1}\{X_i \leq x\}$) and it has some nice properties that are guaranteed to converge to the theoretical CDF [57]. Therefore, the empirical CDF was constructed from the step size histogram, and then was fitted to obtain the diffusion coefficients.

Variational Bayes Single Particle Tracking (vbSPT)

The third method discussed here, vbSPT, is more complex than the other methods but provides a rich diffusion model that can identify different diffusion states, the corresponding occupancies, and the transition probabilities [58]. vbSPT models particle diffusion as a hidden Markov model.

One way to model sequential data is using a Markov model, which is a type of probabilistic graphical model [59]. Given some finite number of states, a first order Markov model assumes that the next state only depends on the current state [59]. The transition probability is the probability for the occurrence of a transition from one state to another, conditioned on the previous state ($p(x_n|x_{n-1})$, where n is the number of latent variables) [59]. Therefore, the probability for a sequence of N observations can be described as follows [59]:

$$p(x_1, ..., x_N) = p(x_1) \prod_{n=2}^{N} p(x_n|x_{n-1})$$

where x_i is the observed state at time i. All of the transition probabilities for a given

state i must sum to 1:

$$\sum_{j=1}^{n} p(x_j|x_i) = 1$$

A hidden Markov model (HMM) is a Markov model where the states are discrete and hidden (latent variables z), and the observations come from one of the discrete states [59]. HMM can be thought of as a mixture model with z_n components, the latent variables, that generate some observation x_m [59]. Since observations are drawn from the latent variables, the emission probabilities describe the probability of generating an observation conditioned on one of the latent variables ($p(x_i|z_j)$) [59]. The transition matrix, A, is an n by n (n is the number of latent variables) square matrix that describes the transition probabilities between every pair of states [59]. A vector of initial state distributions π, where $\pi_i = p(z_i)$ determines the initial probability of observing the first state (z_1) [59]. The joint probability of observing a sequence of N observations ($X = \{x_1, x_2, ..., x_n\}$) given N hidden states ($Z = \{z_1, z_2, ..., z_n\}$) can be written as follows, where $\theta = \{\pi, A, \phi\}$ represents the model parameters:

$$p(X|Z, \theta) = p(z_1|\pi) \prod_{n=2}^{N} p(z_n|z_{n-1}, A) \prod_{m=1}^{N} p(x_m|z_m, \phi)$$

which describes the probability of first state based on the initial probability ($p(z_1|\pi)$), $p(z_n|z_{n-1}, A)$ describes the state transitions, and $p(x_m|z_m, \phi)$ describes the probability of the observation based on the hidden variable with ϕ describing the set of parameters governing the emission probability distribution [59]. Since π is a vector of initial state probabilities, its components must sum to 1 [59]:

$$\sum_{i=1}^{n} \pi_i = 1$$

For single particle tracking experiments, particle diffusion can be modeled with HMM as shown in Figure 1.3.3. The distribution and the order of observed step sizes depend on the hidden diffusion state of the particle. In Figure 1.3.3, a particle

with 2 modes of diffusion spends 60% of its time in a slow diffusion state and the other 40% of its time in a fast diffusion state with corresponding diffusion coefficients of 0.1 μm^2 and 1 μm^2, respectively. If the particle is in the slow state, it is much more likely to generate small step sizes (distribution of steps shown in blue) while a particle in the fast state is more likely to generate large step sizes (distribution of steps shown in red). With enough data, i.e. single particle trajectories, the HMM parameters (diffusion coefficient, occupancy, transition probabilities) that most likely generated the sequences of observed step sizes can be inferred. For a given dataset, vbSPT takes single particle trajectories and infers the HMM parameters for the most optimal model size [58].

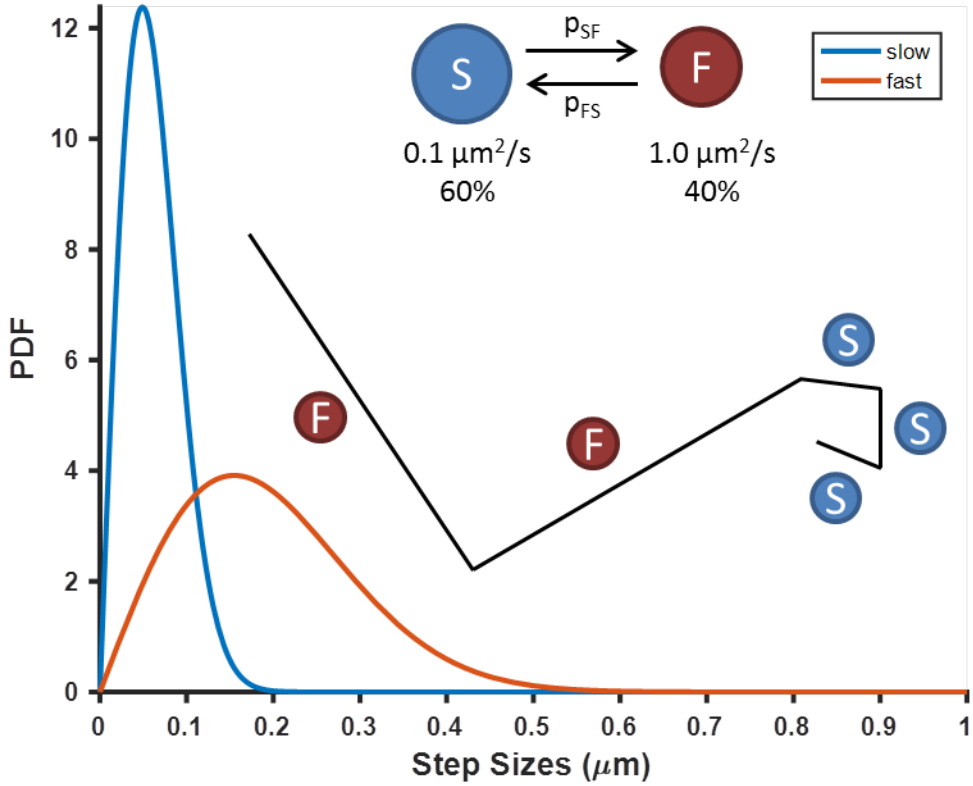

Figure 1.3.3: An Example of Modeling SPT Data with HMM

Among the three different SPT analysis methods discussed above, vbSPT pro-

vides the greatest amount of information [58]. The analysis of MSDs is restricted to the most simple case of a single diffusion state, and CDF fitting is limited to the number of diffusion states (diffusion coefficients and occupancies associated with each diffusion state). Not only does vbSPT estimate the same parameters as CDF fitting, but it also outputs the most probable sequence of hidden states responsible for the observed data [58]. This makes it possible to link diffusion states to spatial and temporal location. Thus, vbSPT allows the detection of dynamic spatiotemporal information.

1.3.4 Application of SPT to studies of protein dynamics on the membrane

Live-cell single-particle tracking (SPT) [47, 48, 14, 49, 40] complements static imaging by providing information about molecular motions, and it has been used to study Ras dynamics on the membrane [60, 61, 62]. The underlying rationale is that interactions of Ras with different membrane domains and signaling partners would manifest as varying diffusion behavior. Indeed, using SPT, Murakoshi et al. observed transient events of Ras immobilization on the membrane, which became more frequent upon epidermal growth factor stimulation, potentially reflecting the formation of signaling complexes or interactions with raft domains [61]. Lommerse and colleagues also used SPT to probe Ras diffusion and similarly observed transient and context-dependent confinement of Ras in membrane regions not more than 200 nm in diameter [62].

1.4 Remaining questions and major directions

1.4.1 Ras clustering at the membrane

Although we have determined the functional necessity of Ras dimers and clusters at the membrane, the mechanisms through which they form, and the role of the biological membrane in signaling activity and specificity of Ras are still poorly

understood. Recent studies suggest that Ras multimer formation, signaling, and membrane partition is dependent on membrane nanodomains. However, due to the static nature and lack of throughput of the high resolution imaging techniques used previously to probe membrane Ras, there is little known about the transient and spatiotemporal dynamics of Ras interaction with the membrane. Thus, this thesis attempts to address some of these remaining questions using live cell sptPALM to detect Ras membrane interactions in real time.

1.4.2 Outline of the Thesis

The following chapters are organized as stated. Chapter 2 describes experimental and analysis pipeline for live cell SPT that will be used for the rest of this thesis. Chapter 3 utilizes the techniques described in Chapter 2 to discover the nested membrane nanodomain organization with respect to Ras. Chapter 4 characterizes the Ras nanodomains found in the previous chapter and explores the differences in Ras isoform interaction with the nanodomains. Chapter 5 explores potential roles for Ras nanodomain in Ras multimer formation and considers the overall impact of the membrane organization in membrane-bound signaling proteins.

Chapter 2

Optimizing data acquisition and analysis for high-throughput SPT

2.1 Introduction

This chapter addresses how single particle tracking movies are processed into single particle trajectories, which is the basis for all of the data analysis, and the pitfalls associated with the data acquisition pipeline. One of the major challenges that we addressed was the impact of the single particle trajectory construction on the diffusion model. All single particle tracking analysis methods that we examined assume that the trajectories are accurate without any false connections between two different particles [61, 48]. Even a relatively small number of misconnections can result in inaccurate diffusion parameters, such as the appearance of additional artificial diffusion states. The problem of trajectory construction has no ground truth; if there are multiple particles within close distance, it is not possible to know the exact assignment between the particles in the previous and current frames. Unfortunately, no simple and straight forward method existed to connect trajectories in high particle density conditions that prevented misconnections. This was not an issue with traditional SPT where a fewer number of fluorophores were imaged with longer trajectories but became a problem for high-throughput SPT where a large number

of particles are collected with short trajectories.

Our investigation into this issue was first prompted by the observation that when using vbSPT to infer the diffusion model based on the experimental sptPALM data [51], the model outputs varied in terms of both the model size (i.e., number of diffusive states, Figure 2.1.1) as well as the model parameters (e.g. diffusion coefficients), even for data acquired from different cells under the same conditions [58]. Moreover, vbSPT also yielded different models depending on the threshold of the search distance used for connecting the particle coordinates in adjacent frames into trajectories [58, 63].

2.2 Experimental set up

2.2.1 Microscope

A custom single color imaging system was constructed using Nikon Eclipse Ti-U inverted microscope with 60x APO TIRF oil objective (NA=1.49). Four lasers emitting at 647 nm, 561 nm, 488 nm, and 405 nm sharing the same light path were directed through a beam expander (50:150 mm) and reflected into the back of the microscope with a multi-edge dichroic mirror (405/488/561/635 nm). The fluorescence signal from the sample was collected through the same objective and passes through a 405/488/561/635 nm quad-edge laser dichroic beamsplitter from Semrock and reflected to the side port by a mirror. Illumination with the 561 nm and 405 nm laser was cleaned up by passing the sample signal through a band pass filter and two notch filters (405 and 561/647) placed before the detector. Fluorescence signal was acquired using an electron multiplied charge-coupled device (Andor iXon Ultra 897). TIRF illumination of the sample was achieved by shifting the incident laser horizontally on the back focal plane of the objective before it entered the microscope. Stage top incubator from Tokai Hit (INUG2F-SSI-W and UNIV2-CSG), connected to a CO2 line, was placed on top of the microscope stage and enabled live cell single particle tracking by controlling the humidity, temperature (37C), and CO2 (5%).

A

Model Size	Count of Movies with Model Size
4	3
5	3
6	8
8	1

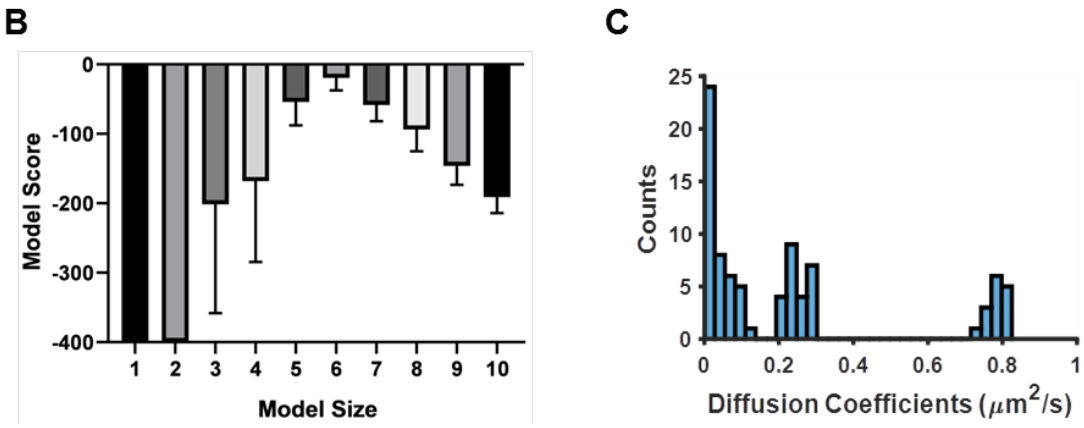

Figure 2.1.1: vbSPT Model Output on Experimental spt-PALM Datasets Acquired at High Particle Densities. When spt-PALM datasets of PAmCherry1-KRas G12D in U2OS cells were acquired at particle densities higher than 0.03 per μm^2 per frame (typically around 0.05 – 0.1 per μm^2 per frame), vbSPT outputs diffusion models of varying sizes, many reaching 6 or more states (A, B). However, a histogram of the diffusion coefficients of all detected states shows 3 clusters, indicating that a three-state model is still likely the best to recapitulate KRas diffusion (C). Note that the three clusters are centered at diffusion coefficient values similar to those obtained with vbSPT or CDF analysis of spt-PALM datasets acquired at low particle densities (<0.03 particles per μm^2 per frame) as in Figure 1F. All data were taken at a frame rate of 35 ms/frame.

2.2.2 Cell line

KRas G12D was genetically fused to PAmCherry1, a red fluorescent protein, to ensure high labeling specificity and efficiency. The PAmCherry1-KRas G12D coding sequence is placed under a CMV promoter regulated by the TetOn operon. The construct was transduced via lentivirus into an isogenic U2OS-tetR cell line that constitutively expresses tetR. Single cell clones were subsequently isolated and

screened to yield isogenic cell lines that express the PAmCherry1-KRas G12D fusion protein under doxycycline (Dox) regulation.

2.2.3 Cell treatment for single particle tracking

Cells were grown in fluorobrite DMEM (Thermo Fisher Scientific A1896701) with 10% FBS in eight well Lab-Tek chambers (155409; Thermo Fisher Scientific) and Dox induced 1.5 days before imaging. The chamber slides were treated with 1M NaOH for 3-5 hours at room temperature and rinsed 5 times with PBS+ and incubated in fluorobrite DMEM prior to being plated by cells. Cells were serum starved for at least 12 hours prior to the movie acquisition and did not exceed 24 hours of serum starvation. Live cell single particle tracking experiments were performed at 37C temperature and 5% CO2 using a stage top incubator (see microscope set up). 561 nm (400 W/cm2) and 405 nm lasers (at extremely low power) were used to excite PAmCherry1 molecules at 12 ms and 35 ms frame intervals.

2.3 Optimizing data analysis for high-throughput SPT

2.3.1 Coordinate Extraction

Similar to PALM, coordinates are extracted from raw images by fitting a two-dimensional Gaussian to each particle, hence sptPALM [40, 50]. The threshold for goodness of fit (RMS) depends on multiple factors, such as the signal to noise ratio [61, 48]. Thus, RMS value was set based on visual inspection of the quality of the particles for each movie. The end product is a list of coordinates and frames for each particle in the movie.

2.4 Two-Dimensional Markov Simulation

As mentioned previously, the identities of individual particles from experimental movies are unlabeled, and hence there is no way to test if the resulting single particle trajectories are correctly constructed. Instead, simulations were used to generate single particle tracking data, with known diffusion parameters, which was then used to test the accuracy of our trajectory connection pipeline. The inputs to the simulations were experimentally derived diffusion parameters: number of trajectories, diffusion coefficients, occupancies, transition matrix, frame rate, and the trajectory density. The trajectory density and the number of trajectories are used to determine the width of the simulation space. At the start of the simulation, every particle is randomly assigned a coordinate and a state based on the occupancies. Once a state is assigned, particles are assigned new coordinates by drawing displacements for each dimension from the corresponding $X \sim N(0, 2Dt)$, where each state has a different diffusion coefficient, D, and t is the time interval. At the next time step, a new state is randomly assigned to every particle based on its current state and the transition probability matrix. This process is repeated for the total simulation time.

2.4.1 Trajectory Connection

Once the coordinates from the experimental movie are collected, single particle trajectories are constructed by connecting the coordinates from the same particle in successive frames. Coordinates in adjacent frames are assumed to be from the same particle if the distance between the coordinates is less than the connection distance threshold. The connection distance threshold specifies the search radius around each particle in the current frame for its possible locations in the next frame. This is a critical parameter for linking particle coordinates into trajectories but is initially unknown. This is addressed in Figure 2.4.1. Trajectories were terminated when no particles or multiple particles were found within the threshold distance in the next frame. Therefore, determining the optimal threshold is vital to preventing false connections between two unrelated particles and also to prevent truncating the left side of the step size histogram generated by real particle movement.

In general, the likelihood of connecting two unrelated particles is the greatest when the maximum step size (frame to frame displacement) for a given particle is large. The maximum step size is a function of the fastest moving particle and the frame rate. The connection distance threshold reflects our belief in the maximum step size a particle could take given a single frame interval. In order to determine the correct connection distance threshold, we ran simulations and compared the step size histogram between the simulated particles and the experimental data.

We ran two-dimensional markov simulations (described in Two-Dimensional Markov Simulation) of diffusing particles with 2 diffusion states (0.1 and 1 μm^2/s, referred to as the 'slow' and the 'fast' states, respectively) at 12 ms frame acquisition time (the fastest frame rate for the camera used with a sufficiently large field of view to fit couple of cells) and particle density at 0.03 particles/μm^2 per frame. Here, the fast diffusion coefficient at 1 μm^2/s was used empirically based on previous reports as well as model outputs from existing datasets [51, 58, 63]. Particle coordinates generated in the simulations were connected in the same way as the experimental datasets to intentionally introduce errors in trajectory connection.

To define the threshold distance, we first constructed the trajectories using an arbitrarily large distance significantly greater than the expected maximum step size ($\sim$2,000 nm), from which a step size histogram could be constructed (Figure 2.4.1 A). The step size histogram broadly consists of two components; signal and noise. Signal represents the shorter step sizes generated by real particle movement, while noise is due to the misconnections between two different random particles. As Figure 2.4.1 A shows, the step size histogram clearly shows the approximate boundary between signal and noise, where the majority of the molecules moved 500 nm or less in 12 ms. Therefore, we reconstructed the single particle trajectories at 400, 500, and 600 nm connection distance thresholds and compared the diffusion model as well as the step size histogram for each condition. We discovered that the exact connection distance threshold was not critical to the diffusion model inference (Figures 2.4.1 B&C). The correct 2 state model was still returned even at 400 nm cut off, even though that threshold clearly truncated the tail of the distribution. However, the tail truncation did result in a slower diffusion coefficient being returned for the fast state. The

occupancy was similar for all three connection distance threshold values.

We applied the same method to determine the connection distance threshold for the experimental data. The step size histogram from PAmCherry1-KRas G12D showed the same pattern as the simulation. The first segment comprised the signal with the first peak around 70 nm and extending to 500 nm, and all step sizes beyond 500 nm was attributed to noise originating from misconnected trajectories generated by the unrealistically large threshold distance. Based on this histogram, we reconstructed the diffusion trajectories using 500 nm as the threshold distance for 12 ms frame acquisition, and 800 nm for 35 ms frame rate movies (using the same method). A new step size histogram was then obtained, which was essentially identical to the first segment of the original step size histogram, confirming that the new threshold distance eliminated most of the misconnected trajectories (similar to Figure 2.4.1 A inset and main panel). The step size histograms of trajectories obtained under the same conditions were also highly consistent, allowing us to set the same threshold value for each condition.

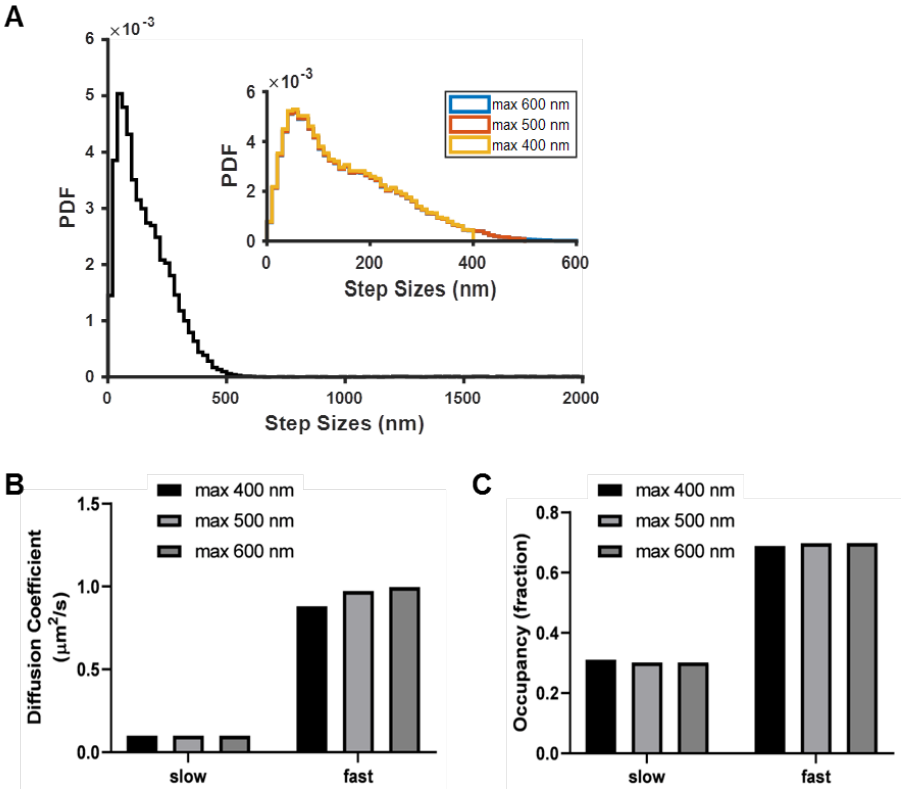

Figure 2.4.1: Impact of the Connection Distance Threshold on vbSPT Model Output. Using simulated trajectories at 0.03 particles/μm^2 per frame, which comprises a two-state system with diffusion coefficients at 0.1 and 1 μm^2/s. We first synthesized trajectories using an unrealistically large connection distance threshold of 2000 nm, and examined the step size distribution of the resulting trajectories (A, main panel), where it became clear that the vast majority of the molecules moved less than 500 nm between frames. Based on this, we chose 400 nm, 500 nm, and 600 nm as the connection distance thresholds and resynthesized the trajectories (A, inset); the histograms essentially overlap except at the large step sizes (blue: 600 nm threshold; red: 500 nm threshold; and yellow: 400 nm threshold). B-C) Comparison of the vbSPT model outputs on trajectories synthesized using the three connection distance threshold values shows that vbSPT was able to pick the correct model size (of 2) at all three settings. However, setting the threshold value at 400 or even 500 nm caused a noticeable truncation in the step size histogram (as shown in A) and resulted in lower diffusion coefficients for the fast state while the 600 nm threshold returned the correct diffusion coefficient; the slow state was not affected. Interestingly, the threshold setting had minimal impact on the resulting outputs for state occupancies (C). These settings were used to guide the trajectory synthesis based on the experimental spt-PALM data.

2.5 Optimizing experimental conditions for high-throughput SPT

2.5.1 Impact of particle density on diffusion model construction

Using the simulated trajectories, we found that the number of particles per raw image frame has a big impact on the diffusion model outputs from vbSPT and CDF. At high particle densities, two different particles from successive frames may be connected leading to some misconnected trajectories and a significant increase of nonexistent, fast-moving particles, which vbSPT would assign to artificial states. As demonstrated in Figure 2.5.1, misconnection occurs only in a tiny fraction of the trajectories (corresponding to the positive end of the step size histogram) and predominantly skews the fast diffusive states of the model where most ambiguities in trajectory connection arise. This manifest as altered diffusion parameters of the fast states or appearance of non-existent 'fast' states with suspiciously low occupancies.

The severity of trajectory misconnection depends on how fast the particles diffuse, how sparse the particles are in each frame, and how quickly the image acquisition takes place. For a given frame rate, the fastest diffusion coefficient dictates the maximum travel distance of a particle, which in turn affects the step size and the particle search distance for trajectory connection threshold. A large search distance threshold results in an increased likelihood of connecting two unrelated particles, especially when the particle density is high. Hence, for accurate model reconstruction, it is better to use a high frame rate with a small number of particles per frame. This effectively eliminates misconnected trajectories and still yields a sufficient number of diffusion trajectories to accurately determine the model.

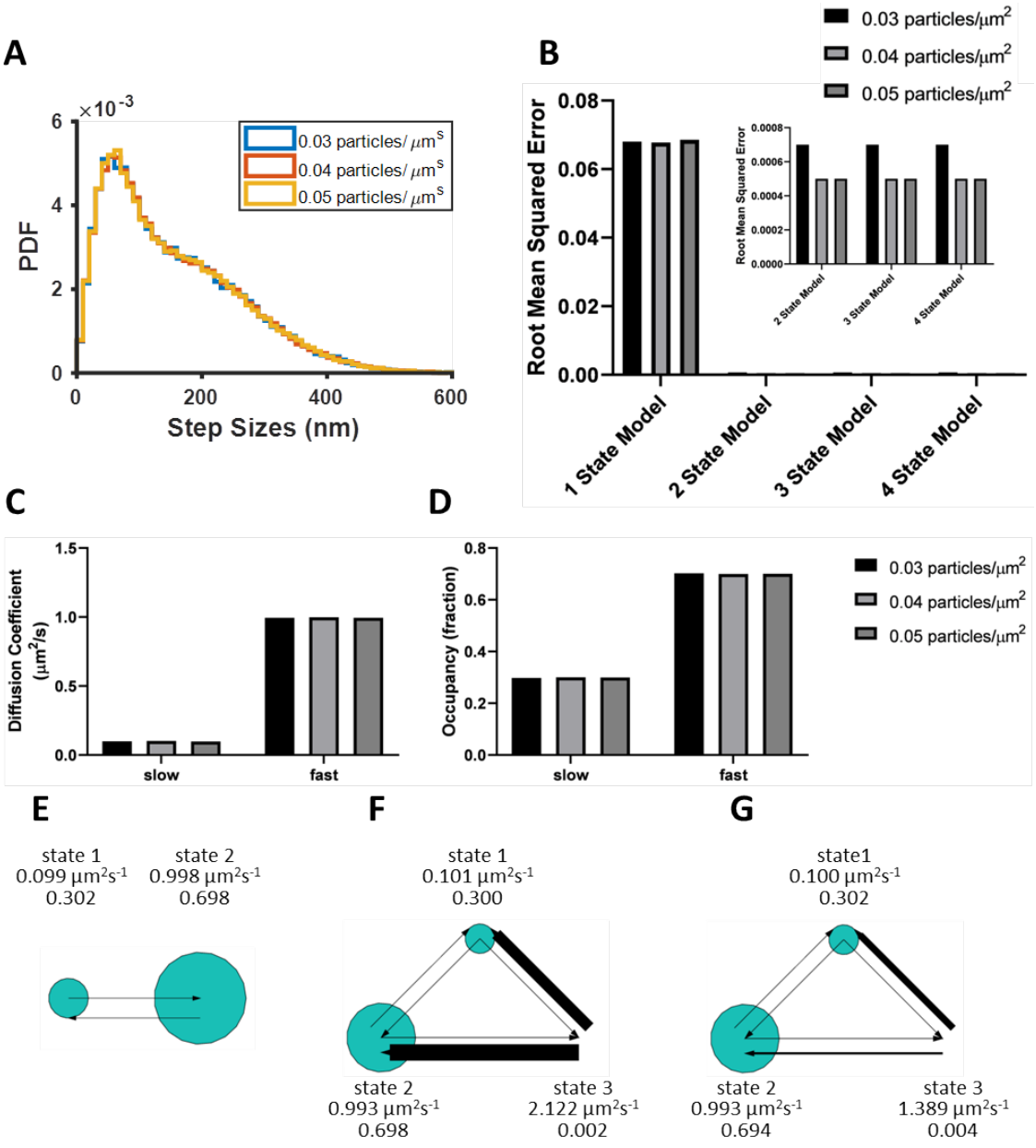
A
×10-3
PDF
Step Sizes (nm)
0.03 particles/ μms
0.04 particles/ μms
0.05 particles/ μms
B
0.03 particles/μm2
0.04 particles/μm2
0.05 particles/μm2
Root Mean Squared Error
1 State Model
2 State Model
3 State Model
4 State Model
C
Diffusion Coefficient (μm2/s)
slow
fast
D
Occupancy (fraction)
E
state 1
0.099 μm2s-1
0.302
state 2
0.998 μm2s-1
0.698
F
state 1
0.101 μm2s-1
0.300
state 2
0.993 μm2s-1
0.698
state 3
2.122 μm2s-1
0.002
G
state1
0.100 μm2s-1
0.302
state 2
0.993 μm2s-1
0.694
state 3
1.389 μm2s-1
0.004

Figure 2.5.1: Impact of Particle Density on Diffusion Model Reconstruction. Test data were generated by simulating diffusion trajectories of two separate populations of particles with no transitions exhibiting diffusion coefficients of 0.1 and 1 μm^2/s, and occupancies of 0.3 and 0.7, respectively (see Methods). About 6-10k trajectories were synthesized (depending on the particle density) with connection distance threshold of 600 nm and analyzed using vbSPT (B-D) or CDF (E-G). A) Histograms of step sizes at 0.03, 0.04, and 0.05 particles/μm^2 per frame; B-D) show the vbSPT outputs on simulated trajectories at 0.03, 0.04, and 0. 05 particles/μm^2, returning 2, 3, and 3 state models respectively, with the model parameters displayed next to each state; E) Goodness of CDF fitting at different model sizes, as well as the diffusion coefficients (F) and state occupancies (G) obtained from fitting to a 2-state model.

2.5.2 Strategies for controlling particle density in high-throughput SPT

We determined the optimal particle density per frame for tracking KRas G12D by testing the performance of our analysis workflow with simulated trajectories at varying particle densities. We used the same simulation described in section 2.2 Trajectory Connection to generate simulated trajectories for particle densities at 0.03, 0.04, and 0.05 per μm^2 per frame. As shown in Figure 2.5.1, while the step size histograms at the three different particle densities seemed virtually identical (Figure 2.5.1 A), vbSPT reported different models for each condition (Figures 2.5.1 B-D), with only the model output at 0.03 per μm^2 per frame being accurate because it correctly predicts a 2-state model. This suggests that the fraction of misconnected trajectories at the higher particle densities could be too small to be detected by visual inspection but it does lead to incorrect model reconstruction. Starting at 0.04 particles per μm^2 per frame, vbSPT detected a third state with a diffusion coefficient greater than 1 μm^2/s but with virtually null occupancies (Figures 2.5.1 C&D). Thus, we set the maximum particle density threshold for all of our movies to be 0.03 particles/μm^2. Interestingly, CDF fitting correctly returned a 2 state model for all the particle densities tested (Figures 2.5.1 E-G), making CDF fitting a useful parallel approach to confirming the model output of vbSPT.

2.6 Discussions/Conclusions

Through a combination of experimental and analysis optimizations, we determined both the experimental conditions and also a post acquisition data analysis pipeline that allowed us to obtain accurate single particle trajectories resulting in a stable diffusion model. Since the biological behavior of the protein of interest should be independent of imaging conditions, we reasoned that the diffusion model should also be independent of image acquisition speed and the particle density in each frame as long as the biological conditions remain the same. Thus, once the diffusion model is acquired under ideal conditions to maximize correct trajectory connections (high frame rate and low particle density per frame), we acquired data obtained in non-ideal conditions (lower frame rate and high particle density per frame) and analyzed the non-ideal dataset with the number of states found in the ideal dataset. This allowed us to acquire significantly higher number of trajectories for each movie which increased the statistical power for the analysis.

A fundamental albeit implicit result from the present study is the importance of experimental parameters in accurately determining the diffusion model, a critical step for in-depth analysis of protein dynamics on the membrane. While there are many different software packages for analyzing spt-PALM trajectories, the importance of controlling the particle density during image acquisition has not previously been recognized to our knowledge. Imaging at a per frame particle density of 0.05-0.1 per μm^2, which is typical for single-molecule localization microscopy, yielded varying estimated model parameters in our early attempts to track KRas with spt-PALM (Figures 2.1.1 & 2.5.1). Using simulations, we found the source of variability to be a small fraction of misconnected trajectories mostly caused by fast moving molecules. In order to minimize the misconnected segments, we kept the density of activated PAmCherry1 in each frame to below 0.03 per μm^2 at an acquisition rate of 12 ms/frame (Figures 2.5.1). With this precaution, we were able to yield a highly consistent diffusion model from trajectories acquired in different cells and under different conditions. This was critical to defining a previously unresolved state with intermediate mobility (D 0.3 μm^2/s) and to all subsequent analyses. We recom-

mend the same precautions to be taken for studies of other membrane molecules.

Chapter 3

High-throughput single-particle tracking reveals nested membrane nanodomains that dictate Ras diffusion and trafficking

This chapter is taken from a published paper [64]. I was responsible for the live cell single particle tracking experiments, post image acquisition processing, and the analysis, including the simulations.

3.1 Introduction

The plasma membrane has a complex and dynamic landscape that helps shape how diverse membrane-localized signaling molecules behave [30, 65, 66, 67, 68, 69]. Among others, the Ras small GTPases are prototypical examples of signaling molecules whose biological activities are directly regulated by the membrane [70, 71]. While biochemical aspects of how Ras interacts with downstream effectors such as Raf have been well studied [72, 73], the mechanisms through which the biological membrane defines the signaling activity and specificity of Ras are still poorly understood.

Recent studies by us and others suggest that Ras signaling may involve the formation of multimers (dimers and/or clusters) in a membrane-dependent manner [74, 34, 36, 75, 23, 35, 25], and that partitioning of Ras into nanoscopic membrane domains and interactions with scaffold proteins or structures likely constitute critical steps to Ras multimer formation and signaling [27, 76, 77, 33]. While previous high-resolution imaging experiments using immuno-EM [23, 25] or quantitative superresolution microscopy [34] were instrumental to revealing the existence of Ras multimers, the resulting images were mostly static and provided limited information about the spatiotemporal dynamics of Ras – membrane domain interactions.

Live-cell single-particle tracking (SPT) [47, 14, 48] complements static imaging by providing information about molecular motions, and it has been used to study Ras dynamics on the membrane [60, 61, 62]. The underlying rationale is that interactions of Ras with different membrane domains and signaling partners would manifest as varying diffusion behavior. Indeed, using SPT, Murakoshi et al. observed transient events of Ras immobilization on the membrane, which became more frequent upon epidermal growth factor stimulation, potentially reflecting the formation of signaling complexes or interactions with raft domains [61]. Lommerse and colleagues also used SPT to probe Ras diffusion and similarly observed transient and context-dependent confinement of Ras in membrane regions not more than 200 nm in diameter [60].

These prior studies offered important initial insight into the potential connections between Ras diffusion, function, and membrane organization, but the technical constraints of traditional SPT limited the throughput and depth of analysis in these studies. Typically, only a few tens of trajectories could be obtained from each experiment, which precluded detailed and quantitative characterization of the heterogeneous and stochastic nature of molecular diffusion. In consequence, while the studies consistently reported two diffusion states – a 'free' diffusion state and another 'immobile' state, it remains to be seen whether a two-state model accurately recapitulates Ras membrane dynamics [60, 61, 62]. Thus, the nature of the membrane domains occupied by each of these states and how Ras molecules transition between the states in connection with multimer formation and signaling remain unclear.

Recent years have seen significant advances in both experimental [51, 78, 79, 80,

81, 82] and data analytic strategies [58, 83, 63, 84, 85, 86, 87, 88, 89] of SPT, some of which have dramatically improved the information throughput. Among others, spt-PALM combines SPT with photoactivated localization microscopy (PALM) to enable single molecule tracking under dense labeling conditions through stochastic photoswitching30. With spt-PALM, it is routine to acquire thousands of diffusion trajectories from a single cell. A growing list of software tools has also been developed to facilitate spt-PALM data analysis [58, 63, 84, 88, 90]. In particular, the variational Bayes SPT (vbSPT) package allows construction of a detailed diffusion model from spt-PALM data with parameters such as the number of states, the diffusion coefficient and the occupancy of each state, as well as the state transition rates even when the individual trajectories are short [58]. Additionally, a wide range of analytical methods has been introduced to gain further insight into the states and the state transitions from SPT trajectories [85, 88, 50]. These advances help overcome the limitations of conventional SPT and make it possible to analyze Ras membrane dynamics in much greater depth.

Here, we report our efforts on combining spt-PALM with detailed trajectory analysis to reveal previously unknown aspects of Ras diffusion on the cell membrane. With carefully controlled expression levels and photoactivation rate, spt-PALM trajectories of PAmCherry1-tagged KRas G12D consistently reported three diffusion states, including a fast diffusion state, an immobile state, and a previously unidentified diffusion state with intermediate mobility. Leveraging the large number of trajectories, we were able to spatially map the diffusion states to distinctive membrane domains, estimate the size and life time of each domain, and define the spatial relationship between the domains. Moreover, in analyzing how KRas transitions from one diffusion state to another, we discovered that KRas diffusion follows a non-equilibrium steady state (NESS) model with net mass flow from the fast state to the immobile state, likely coupled to the endocytic trafficking and membrane recycling of KRas. Based on these results, we propose a new model to describe the membrane dynamics of KRas, where nested membrane nanodomains dictate the diffusion, trafficking, and potentially multimer formation and signaling.

3.2 Experimental and data analysis methods

Cell line and treatment for single particle tracking. Same cell line and live cell image acquisition conditions described in Chapter 2 were used for the data gathered in this chapter.

Imaging optimization. Based on the results of Chapter 2, we chose to use a high frame rate (12 ms/frame) and a low particle density ($< 0.03\ \mu m^{-2}$) to eliminate misconnected trajectory segments while maintaining a sufficient number of trajectories. However, it is beneficial to obtain more trajectories to accurately infer the model parameters with vbSPT, especially for the transition probabilities [58]. As demonstrated in Figure 3.3.11, the diffusion coefficients and the occupancies typically converged with only a few thousand trajectories, but the transition probabilities required significantly more trajectories to converge. Thus, we usually acquired spt-PALM data at higher particle densities once the model size has been defined; for these datasets, we could safely enforce a three-state model during vbSPT data analysis, since the diffusion model should not depend on the rates of frame acquisition rate and photoactivation. This strategy allowed more flexibility in spt-PALM data acquisition and robustness in the subsequent analyses.

Trajectory connection for single particle tracking. As discussed in Chapter 2, we used 500 nm connection distance threshold for the 12 ms dataset and 800 nm connection distance threshold for the 35 ms dataset.

Two-dimensional Markov simulation. We relied on two-dimensional simulations that mimic experimental observations as controls for some of the analysis. The same simulations utilized in Chapter 2 (Two-Dimensional Markov Simulation) were used as a negative control to test the null hypothesis for spatial clustering (Figures 3.3.3, 3.3.4, 3.3.6, 4.3.3, 4.3.8) and equilibrium state analysis (Figures 3.3.7, 3.3.8). When the simulation was used as the negative control (Figures 3.3.3, 3.3.4, 3.3.6, 4.3.3, 4.3.8, 3.3.7), the simulation was run for every single movie acquired and the

results were compared to the experiment.

State assignment and averaging. States for each trajectory segment were assigned using vbSPT (contained in field est2.sMaxP, refer to the vbSPT manual). The state assignment is based on trajectory displacements, not the coordinates (e.g. if a trajectory has 3 coordinates, then 2 states are returned for the 2 steps). In order to prevent over counting for the pair correlation analysis (Figures 3.3.3, 3.3.4, 3.3.6, 4.3.3, 4.3.8), in the case of a single molecule staying in the same domain for multiple frames, we averaged all of the coordinates (including both ends) that were assigned the same state for consecutive time points in a single trajectory.

Pair correlation function. Pair correlation function, or $g(r)$, in general, measures the deviation of the particle density from the expected value from a reference particle as a function of distance. More specifically, $g(r)$ was calculated for each particle by counting the number of other particles within a circular shell at distance of r and $r + 10$ nm and dividing by the expected number of particles assuming uniform distribution. Therefore, when the observed number of particles for a given distance is equal to the expected number of particles given complete spatial randomness, $g(r) = 1$ and signifies random distribution of particles. Accordingly, $g(r) > 1$ indicates clustering behavior since there are more observed particles around each particle than expected, and $g(r) < 1$ represents cases where there are fewer particles than expected. Every movie was sliced into non-overlapping time segments (1, 5, 10, 20 min) and the average position for each state segment was extracted (as described in State Classification and Averaging) such that every coordinate represented a continuous track for an individual particle in a domain. Therefore, the coordinates used to calculate the pair correlation function represented either different particles that visited the same domain or the same particle that left the domain and returned at a later time. The resulting coordinates were separated into each of the three states, and the $g(r)$ was calculated for the coordinates of a given state within the given time slice. In cross pair correlation function analysis, $g(r)$ was calculated for a given pair of different states.

Statistical analysis. Sample size is shown for each figure in the figure captions as n and was not predetermined. All results on model parameters and subsequent quantifications such as mass-flow rates are shown as arithmetic mean ± 95% confidence interval. Spt-PALM datasets with insufficient number of trajectories to fully fit up to a 10-state model (e.g. Figure 3.3.1 E) using vbSPT were discarded. The full raw dataset, including an outlier with abnormally long average trajectory length and all the discarded datasets are presented in Figure 3.3.11.

3.3 Results

3.3.1 Establishing a three-state model of KRas diffusion on the membrane

To investigate the lateral diffusion properties of KRas under controlled expression levels, we established isogenic U2OS cells stably expressing PAmCherry1-KRas G12D under doxycycline (Dox) regulation [34]. The expression level of PAmCherry1-KRas G12D was comparable to that of the endogenous KRas at 2 ng/mL Dox as judged by western blotting, with higher expression levels achieved at 5 - 10 ng/mL Dox (Figure 3.3.1 A). Hence, initially data were collected from cells induced at 2 ng/mL Dox. The photoactivatable fluorescent protein PAmCherry1 has been widely used for quantitative PALM and spt-PALM [91]. Owing to the good single-molecule brightness of activated PAmCherry1, we were able to track individual PAmCherry1-KRas G12D molecules at frame rates up to ∼83 Hz (i.e., ∼12 ms/frame) with a low excitation dose (∼400 W/cm^2 at 561 nm). The low spontaneous photoactivation rate of PAmCherry1 also permits clean single-molecule imaging even at high expression levels, yielding as many as hundreds of thousands of trajectories per cell via spt-PALM (Figure 3.3.1 B).

A close inspection of the individual trajectories clearly shows larger diffusive steps intermittent with moments of transient entrapment, indicating the presence of multiple diffusion states and frequent state transitions (Figure 3.3.1 C and inset). Similar observations were reported for both HRas and KRas in previous low throughput SPT

experiments, where two diffusion states – a 'fast' state and an 'immobile' diffusion state – were detected [60, 61].

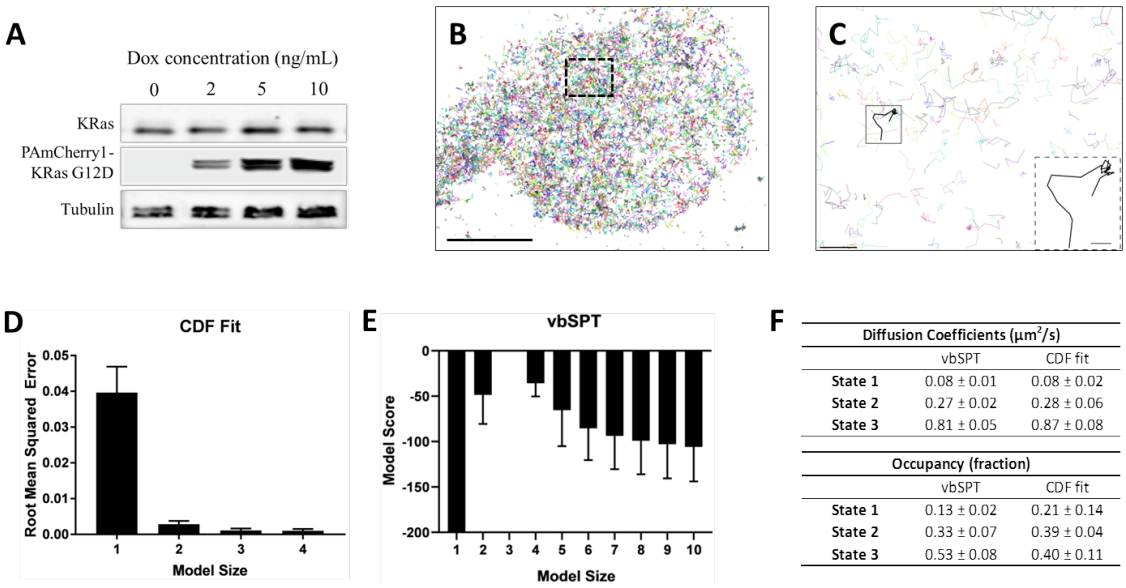

F

Diffusion Coefficients (μm²/s)		
	vbSPT	CDF fit
State 1	0.08 ± 0.01	0.08 ± 0.02
State 2	0.27 ± 0.02	0.28 ± 0.06
State 3	0.81 ± 0.05	0.87 ± 0.08

Occupancy (fraction)		
	vbSPT	CDF fit
State 1	0.13 ± 0.02	0.21 ± 0.14
State 2	0.33 ± 0.07	0.39 ± 0.04
State 3	0.53 ± 0.08	0.40 ± 0.11

Figure 3.3.1: Defining the membrane diffusion model of KRas using spt-PALM and vbSPT. A) Western blot showing the increasing expression level of PAmCherry1-KRas G12D with increasing doxycycline (Dox) concentration; B) Example trajectory map of membrane KRas acquired at 12 ms frame rate using TIRF illumination. Each line represents an individual Ras molecule coordinate over time acquired for the duration of the movie (20 minutes). Only a subset of all trajectories is plotted. Scale bar: 10 μm; C) Expanded view of the boxed region in B). Only a subset of all of the trajectories in the boxed region is shown to allow unhindered view of individual Ras trajectories. Inset shows a KRas trajectory displaying multiple diffusion states. Scale bars: main figure: 1 μm; inset: 200 nm; D) Determining the optimal model size for KRas membrane diffusion using CDF fitting, with smaller root mean squared error indicating a better model (n=8); E) Determining the optimal model size for KRas membrane diffusion using vbSPT, with smaller absolute model score (i.e., score of zero being the best global model) indicating a better model (n=5); F) Comparing the model parameters obtained from CDF fit and vbSPT, both using a three-state model for KRas membrane diffusion. State transition probabilities were not inferred from CDF fit and therefore not included in the comparison. Error bars are 95% confidence intervals (CIs).

Since spt-PALM offers a much larger number of trajectories, we first asked whether KRas diffusion on the cell membrane could indeed be described by a simple two-state model. To this end, we used two methods to analyze the Ras diffusion trajectories. The first approach fits cumulative distribution function (CDF) for Brownian motion to the squared displacements of Ras trajectories to extract diffusion coefficients and the respective occupancies of the diffusion states [54]. The second method, vbSPT, treats particle diffusion and the associated state transitions with a Hidden Markov Model and performs model selection through variational inference [58].

Using trajectories acquired and analyzed with the optimizations from Chapter 2, both CDF fitting and vbSPT yielded similar three-state models for KRas G12D diffusion on the membrane of live U2OS cells. Specifically, CDF fitting to a three-state model had significantly lower residual error compared to a single- or a two-state model and further increasing the model size did not decrease the error (Figure 3.3.1 D), indicating that a three-state model is sufficient to describe the data. For vbSPT, a score equal to zero indicates the best model, a condition that was met with a three-state model but not with larger or smaller size models (Figure 3.3.1 E). The diffusion coefficient and the occupancy for each of the diffusion states were in good agreement between the two analysis methods and within each method when applied to different cells under the same conditions, as evidenced by the small errors (Figure 3.3.1 F). As discussed in the previous chapter, datasets with high particle densities can return models with variable sizes, sometimes also with aberrant model parameters; even so, the histogram of all vbSPT-derived diffusion coefficients still showed three distinct clusters (Figure 2.1.1 C) corresponding to the three states listed in Figure 3.3.1 F. Thus, we concluded that the membrane diffusion of KRas G12D under our experimental conditions is best described by a three-state model, demonstrating the existence of an intermediate state not detected in previous studies. Between the two methods, vbSPT was used for most subsequent analyses in the remainder of this work because it supplies the transition probabilities and state identities for every time step whereas CDF does not.

The diffusion coefficient of the slowest state in Figure 3.3.1 F is comparable to that expected from single-molecule localization error (30 nm, Figure 3.3.2), which

implied that the actual diffusion of KRas in this state may be even slower than it appeared.To test this hypothesis, we acquired spt-PALM data at a slower frame rate (35 ms/frame) to improve the localization accuracy of slowly moving molecules since more photons could now be collected for each PAmCherry1 molecule in a single frame (Figure 3.3.2). Indeed, these datasets reported a significantly smaller diffusion coefficient (0.02 μm^2/s) for the slowest state than that obtained earlier (0.08 μm^2/s) using data taken at 12 ms/frame. This result suggests that the slowest diffusion state of KRas is essentially an immobile state, consistent with previous reports [60, 61].

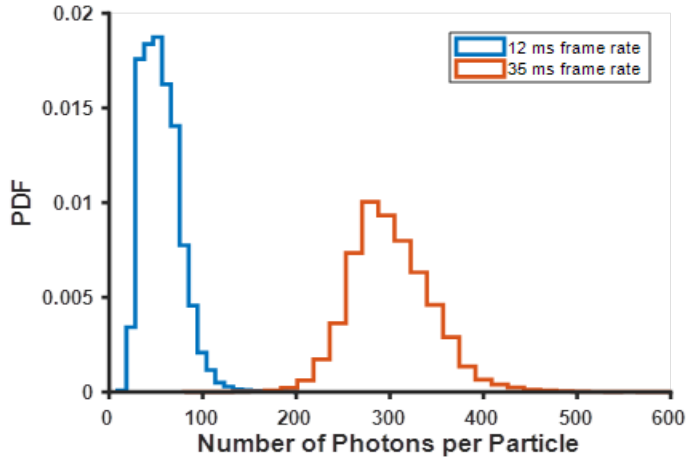

Figure 3.3.2: Photon yield and localization accuracy at the different frame rates used in this work. Photon yields were calculated based on the integrated intensity above background across a 9×9 pixel area for each single-molecule image; the pixel intensity units were converted to the number of photons using hardware specific gain conversion factors. On average, the photon yield for single PAmCherry1 molecules at 12 ms and 35 ms frame acquisition time was 56 photons and 301 photons, corresponding to 26 nm and 10 nm localization precisions, respectively.

3.3.2 KRas diffusion states are associated with distinct membrane domains

The diffusion model presented in Figure 3.3.3 A summarizes the results from the spt-PALM trajectory analyses using vbSPT. Each circle represents one of the

diffusion states with arrows indicating the transition probabilities between pairs of states. A notable feature of this model is that there appears to be a defined state transition path: KRas molecules always transition between the fast (F) and the immobile (I) states by going through the intermediate (N) state, and direct transitions between the fast and the immobile states almost never occur. In order to confirm this transition path, we compared the distribution of step sizes relative to the immobile state steps, since different step sizes would reflect different diffusion coefficients. In support of this hypothesis, the histogram of step sizes immediately adjacent to the immobile steps corresponded to the intermediate diffusion state (Figure 3.3.3 B, blue) while the distribution of the remaining steps had a broader peak implying a mixture of both fast and intermediate diffusion steps (Figure 3.3.3 B, where the black color indicates a mixture of states). As expected, the step sizes assigned to the immobile states (Figure 3.3.3 B, red) are even smaller compared to that of the other two states. The clear separation of these three step size distributions confirms the above-mentioned transition path through the intermediate state. The distinctions in step sizes among the three states were even more obvious on data taken at 35 ms/frame, which had better single-molecule localization precision (Figure 3.3.4). Thus, the intermediate state is not merely a state with intermediate mobility but effectively an obligatory link between the immobile and the fast states of KRas.

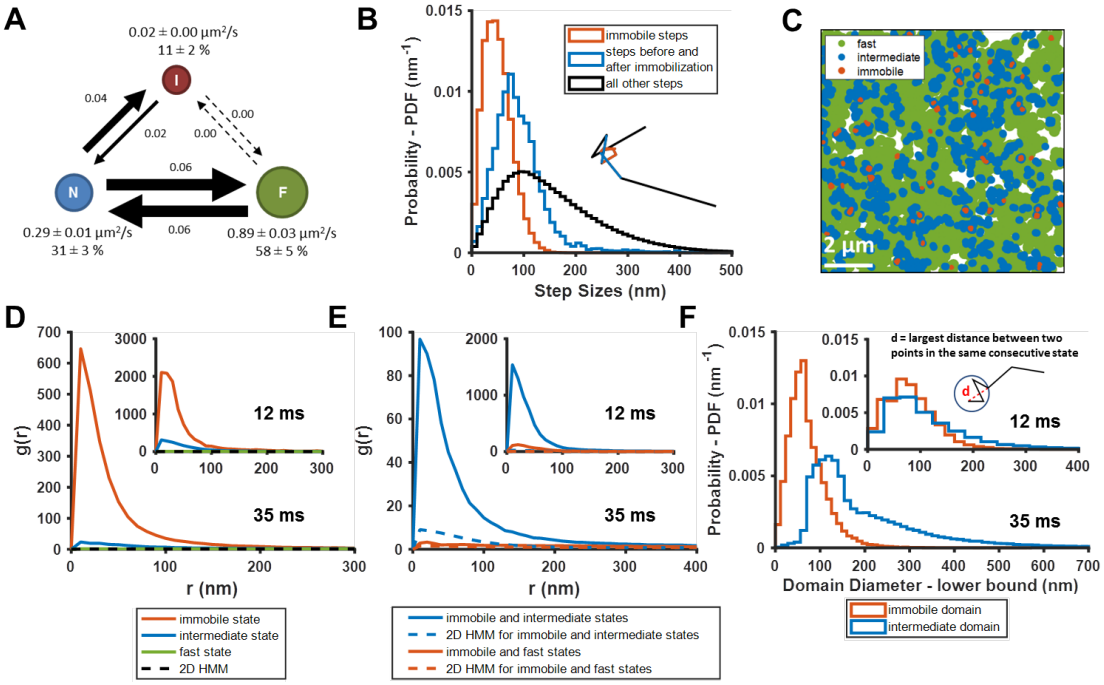
A
0.02 ± 0.00 μm²/s
11 ± 2 %
I
0.04
0.02
0.00
0.00
0.06
N
F
0.06
0.29 ± 0.01 μm²/s
31 ± 3 %
0.89 ± 0.03 μm²/s
58 ± 5 %
B
Probability - PDF (nm⁻¹)
immobile steps
steps before and after immobilization
all other steps
Step Sizes (nm)
C
fast
intermediate
immobile
2 μm
D
g(r)
12 ms
35 ms
r (nm)
immobile state
intermediate state
fast state
2D HMM
E
g(r)
12 ms
35 ms
r (nm)
immobile and intermediate states
2D HMM for immobile and intermediate states
immobile and fast states
2D HMM for immobile and fast states
F
Probability - PDF (nm⁻¹)
d = largest distance between two points in the same consecutive state
d
12 ms
35 ms
Domain Diameter - lower bound (nm)
immobile domain
intermediate domain

Figure 3.3.3: KRas diffusion states are associated with distinct membrane domains. A) The three-state model for KRas diffusion with F, N, and I, representing the fast, the intermediate, and the immobile states, respectively. Model parameters were inferred using vbSPT on spt-PALM datasets with at least 30,000 trajectories obtained on cells induced with 2 ng/mL Dox. The arrows indicate state transitions (i.e. the probability of switching to a different state in the next frame) and the area of the circle and the thickness of the arrows are both roughly scaled to reflect their relative values. All parameters were derived from data acquired at 12 ms frame interval except for the diffusion coefficient of the immobile state, which was inferred from data taken at 35 ms frame interval. Error bars are 95% CIs (n=8); B) Step size histograms for immobilization events (red), one step before or after the immobilization event (blue), and all other steps (black). A diffusion step was part of an immobilization event if immobile state was assigned to that trajectory segment by vbSPT (n=14, see Methods); C) Map of the membrane locations where KRas molecules exhibit specific diffusion states (referred to as state coordinates) within a one-minute duration (taken from a spt-PALM dataset of 20 min total duration). Red, blue, and green dots represent locations of the immobile, the intermediate, and the fast states, respectively, with each rendered circles scaled proportionally to the mean diffusion coefficient for the state; D) Pair correlation analysis on the averaged state coordinates across multiple, one-minute segments of longer spt-PALM datasets. The same color coding as in B) was used to distinguish the three states. For this analysis, molecules in the same diffusion state in successive frames only contributed a single, averaged state coordinate. The average state coordinates of all molecules captured within a one-minute segment were used for correlation analysis, and the results from multiple one-minute segments were averaged to yield the plot. The negative control was generated through a 2D Markovian simulation, and the resulting trajectories were analyzed the same as the experiment (see Methods); E) Cross correlation analysis between pairs of diffusion states. The state coordinates were processed the same way as in D) prior to the correlation analysis, except that the correlation was performed between two different diffusion states. The negative control was generated through a 2D Markovian simulation, and the resulting trajectories were analyzed the same as the experiment (see Methods); F) Estimating the lower bound size for the immobile and the intermediate domains. The estimation was based on the maximum distance traveled by the molecule while in the same diffusion state. *D-F) The main panel shows results inferred from data taken at 35 ms frame intervals for improved localization precision. The inset shows the data taken at 12 ms/frame (n=14 for 12 ms and n=7 for 35 ms datasets).

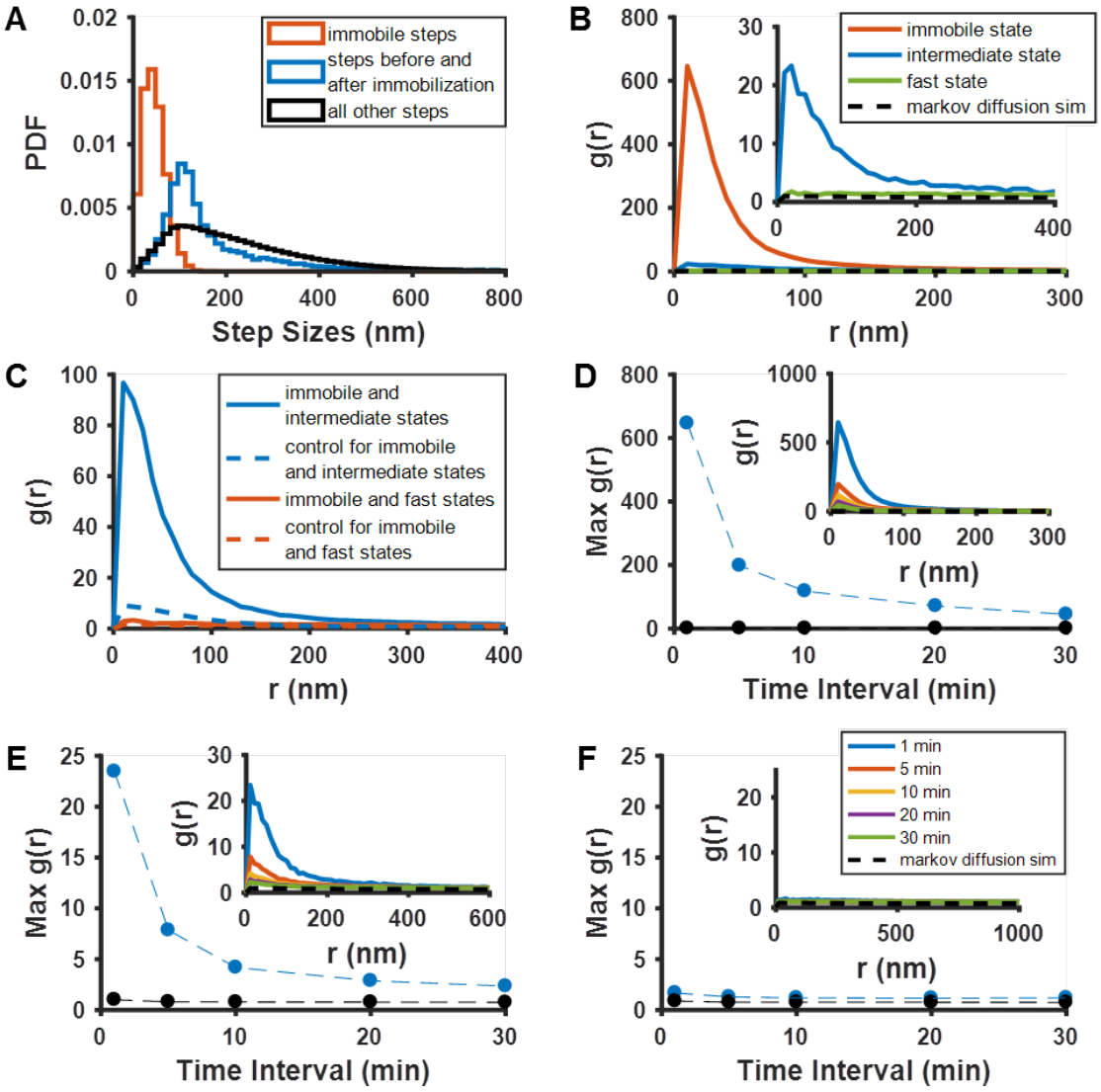
A
PDF
Step Sizes (nm)
immobile steps
steps before and after immobilization
all other steps
B
g(r)
r (nm)
immobile state
intermediate state
fast state
markov diffusion sim
C
g(r)
r (nm)
immobile and intermediate states
control for immobile and intermediate states
immobile and fast states
control for immobile and fast states
D
Max g(r)
Time Interval (min)
g(r)
r (nm)
E
Max g(r)
Time Interval (min)
g(r)
r (nm)
F
Max g(r)
Time Interval (min)
g(r)
r (nm)
1 min
5 min
10 min
20 min
30 min
markov diffusion sim

Figure 3.3.4: Spatial analysis of KRas membrane domain properties using data acquired at 35 ms per frame. As spt-PALM data acquired at 35 ms/frame showed better single-molecule localization accuracy than those at 12 ms/frame, we aimed to perform similar analysis of the domain properties to that shown in Figures 3.3.3 & 3.3.6 using data taken at 35 ms/frame (n=7). A) Step size histograms for the immobilization events (red), the steps directly before and after the immobilization events (blue), and all other steps (black); B) Pair correlation analysis on the averaged positions of the three states for one-minute temporal slices of the raw spt-PALM image stack (see Methods), shows the same trend as observed with data taken at 12 ms/frame acquisition rate. Note the somewhat reduced spatial correlation for the intermediate domain (state) compared with that obtained with data taken at 12 ms/frame (Figure 3.3.3 D); C) Cross-correlation analysis between the three membrane domains, performed on the same one-minute slices of the raw spt-PALM image stack; D-F) Peak amplitudes of autocorrelation $g(r)$ at different time intervals. The steadily decreasing $g(r)$ with increasing time intervals indicates the life times of the immobile and the intermediate domains to be on the order of minutes.

The observed state transition path may arise from at least two potential scenarios. In the first scenario, fast diffusing KRas may transition into the intermediate then the immobile state through spontaneous conformational changes unrelated to slow or static membrane structures. Alternatively, the immobile states could be caused by KRas transiently binding to structures (termed 'immobilization sites or domains') residing in specialized membrane regions that confer intermediate mobility to KRas (termed 'intermediate domains'). Consequently, these intermediate domains would act as transition zones between membrane regions where KRas exhibits fast diffusion and the sites of KRas immobilization, yielding the observed state transition path. In either case, the intermediate and the immobile states of KRas would be temporally and spatially correlated. It is only in the latter case, however, that we would observe multiple visits to the same intermediate or immobilization domains by different KRas molecules, provided that both domains have life times longer than our temporal resolution. Of note, the second scenario may encompass the first, as KRas targeting to the intermediate or immobile domain may take a different conformation than those molecules still in the fast state.

To distinguish between the two scenarios, we performed auto- and cross-correlation analysis on the locations of KRas exhibiting a certain diffusion state (referred to hereafter as state coordinates). We first visually examined the spatial distributions of the states by slicing each raw image stacks into one-minute time segments and plotting the state coordinates on the same map, with each color representing one of the states (Figure 3.3.3 C, Figure 3.3.5). Each diffusion trajectory typically contributes only a few points to the plots as limited by its short duration, and the points from multiple trajectories accumulate over time (up to 1 min in this case) to 'paint' a map of the membrane regions associated with each of the diffusion states. As shown in Figure 3.3.3 C, the intermediate states and the immobile states not only co-clustered, but also each appeared to self-cluster. Specifically, regions corresponding to the intermediate states (blue) often connect to give rise to nanoscopic domains a few hundred nm in size and the vast majority of the immobilization sites (red) are surrounded by the intermediate domains. By contrast, regions corresponding to the fast state occupy the majority of the membrane area. While both the intermediate and the immobile domains appeared to be dynamic, a time-lapse domain map showed that at least some of these domains could last a few minutes (addressed in Figure 3.3.6). Thus, spatial mapping of the KRas state coordinates provided visual evidence for the physical presence of nested, nanoscopic domains conferring the distinct KRas diffusion states.

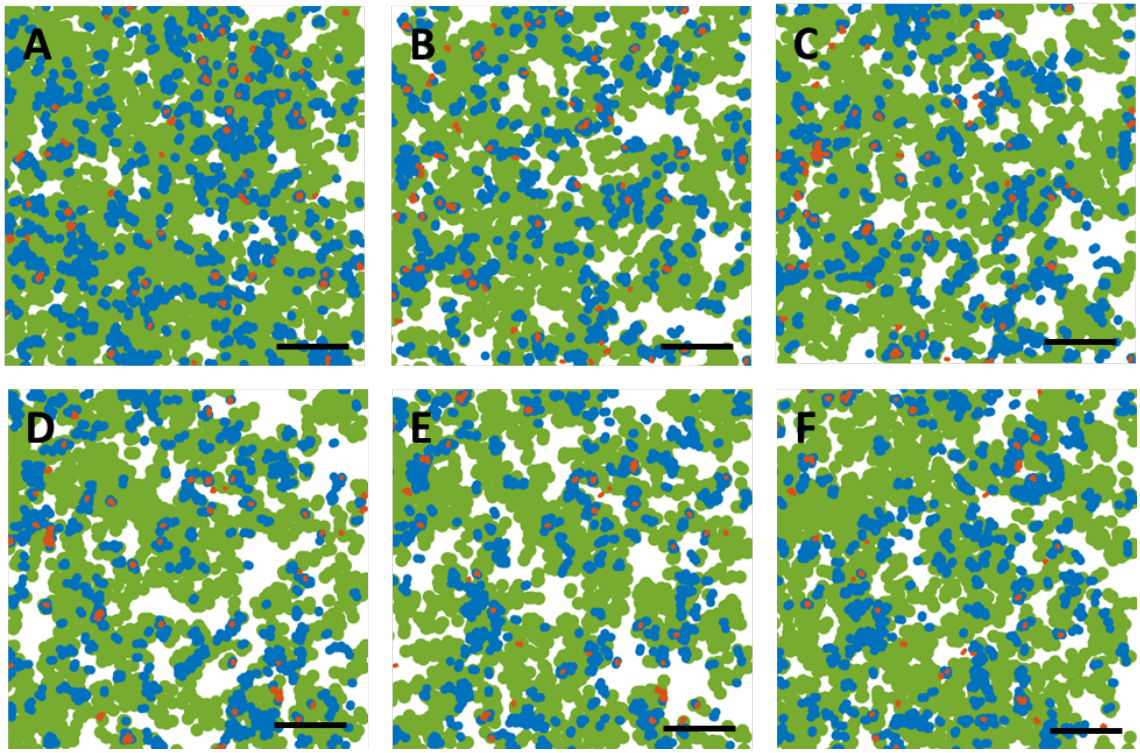

Figure 3.3.5: Temporal evolution of the membrane domains associated with each KRas diffusive state. The three membrane domains associated with the immobile, intermediate, and fast states of KRas are labeled with red, blue, and green, respectively. The domain maps were generated using the same approach as described for Figure 3.3.3 C (12 ms frame interval), with each panel representing the domain map within a 1 min duration with 0.5 min overlap. Thus, A-C represent total of 3.5 min time period. Of note, the maps were generated without position averaging, and therefore each trajectory contributes 2 or more points (including the beginning and the end) in the corresponding plot. Scale bars, 2 μm.

We next used pair correlation function (g(r)) to quantitate the spatial relationship between the KRas states (Figures 3.3.3 D-E). The function $g(r)$ measures the ratio of the number of particles located a distance (r) from a given particle to that expected from a complete spatial randomness (see Methods). Here, the $g(r)$ $g(r)$ could be calculated for particles in the same diffusion state (auto-correlation) or between two different diffusion states (cross-correlation); in either case, amplitudes of $g(r)$ significantly greater than that expected for a random distribution indicate spatial clustering. When multiple KRas molecules visit the same domain, each at a different time point but exhibiting the same diffusive state, $g(r)$ would detect spatial auto-correlation for the given state. To avoid false clustering due to the same molecule staying in the same state across multiple frames, we used the averaged state coordinate for each continuous trajectory segment that stayed in the same state for more than two consecutive time points (see Methods). Results from both datasets taken at 35 ms/frame (main panels) and those at 12 ms/frame (inset) are shown for comparison (Figures 3.3.3 D-E).

Consistent with the visual observation earlier (Figure 3.3.3 C), coordinates of the immobile and the intermediate states each showed significant clustering in the $g(r)$ plots averaged across each 1-minute raw image stacks, whereas $g(r)$ of the fast state was barely above random across the full range of r analyzed (Figure 3.3.3 D). All $g(r)$ negative controls were generated with a 2D Markovian simulation of diffusing particles with no associated domains (see Methods), and the simulated trajectories were processed through the same analysis pipeline as the experimental data. As expected, the averaged state coordinates of the simulated negative control had values close to one and showed no peak in the $g(r)$ plots. Furthermore, $g(r)$ based on spatial cross-correlation analysis clearly indicated co-clustering between the immobile and the intermediate state positions but not with the fast diffusion state (Figure 3.3.3 E).

We also estimated the lower-bound size of the domains associated with the immobile and the intermediate states of KRas by calculating the maximum distance a particle traveled while in a domain (i.e., longest distance between two points within consecutive steps taken while in the same state). Shown in the main panel Fig-

ure 3.3.3 F are the histograms of the estimated domain sizes determined from data taken at 35 ms/frame, based on which we determined that the mean diameters of the intermediate and the immobile membrane domains were at least 200 nm and 70 nm, respectively. This is consistent with the notion that most immobile domains are likely surrounded by intermediate domains. The distinction between the two domains became much significant with data taken at 12 ms/frame, which we attributed to the low localization precision of single PAmCherry1 molecules at this fast frame rate. The distribution of the minimum intermediate domain size appeared to have at least two peaks at 120 nm and 230 nm, implying that there may potentially be multiple types of intermediate domains (Figure 3.3.3 F).

3.3.3 Transient, nanoscopic domains mediate the intermediate and the immobile states of KRas

To understand the temporal behavior of the immobile and the intermediate domains, we extended $g(r)$ calculations as in Figure 3.3.3 from one minute to longer time intervals. The rationale was that, as the time interval for calculating $g(r)$ increases beyond the life time of a domain, the chance of observing KRas molecules visiting the same domain (i.e., exhibiting the same diffusion state in close proximity) should decrease, resulting in lower $g(r)$. Indeed, as shown in Figure 3.3.6 A-C, for dataset acquired at 12 ms frame interval, the peak amplitudes of $g(r)$ for both the immobile (Figure 3.3.6 A) and the intermediate (Figiure 3.3.6 B) states decreased significantly after 5 min with further decay at increasing time intervals, indicative of finite life times for both nanodomains, likely on the order of minutes on average (see also Figure 3.3.4 for results with data taken at 35 ms/frame). For the limited temporal resolution of this analysis, we likely only detected relatively stable domains with life times longer than 1 min, and the presence of more transient intermediate or immobile domains should not be ruled out.

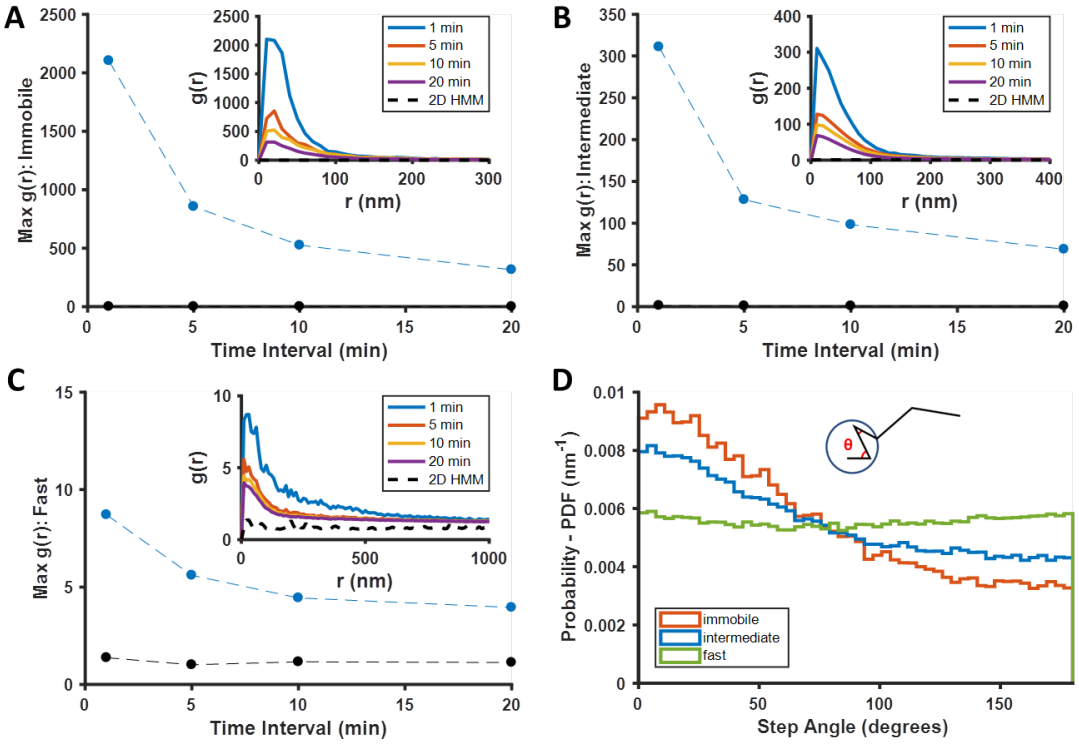

Figure 3.3.6: Temporal properties of the KRas-associated immobile and intermediate domains. A-C) Pair correlation analysis of the state coordinates at different time intervals (1, 5, 10, and 20 min). The amplitude (maximal $g(r)$ value) of the pair correlation function at each time interval was plotted in the main panel with the raw pair correlation plots shown in the inset. A-C show pair correlation functions of averaged coordinates for the immobile, the intermediate, and the fast states, respectively (see Methods). The negative control in each case was generated through a 2D Markovian simulation, and the resulting trajectories were analyzed the same as the experiment (see Methods); D) Deflection angle analysis on KRas diffusion trajectories separated by diffusion states (red: immobile; blue: intermediate; green: fast). The deflection angle was calculated as the angle between two successive segments of the trajectory while the molecule was in the same diffusion state. *Results shown for data acquired at 12 ms/frame (n=14).

To gain insight into how KRas interacts with the different membrane domains, we also analyzed the frame-to-frame deflection angle for KRas molecules within each domain. The deflection angle measures the relationship between the current and the preceding step: a complete random walk would yield a flat distribution of deflection angles, whereas a preference for acute angles indicates more 'returning' steps. As shown in Figure 3.3.4 D, KRas molecules trapped in either the immobile or the intermediate domains (the red and the blue lines) were more likely to exhibit acute deflection angles, potentially due to backward movements at the domain boundaries. In comparison, KRas molecules in the fast state exhibit (Figure 3.3.4 D, the green line) equal probabilities of moving in all directions, consistent with Brownian motion.

3.3.4 Mass flow between the KRas diffusion states

The small variance in the estimated model parameters from data taken on different cells, be it from the same or different samples (Figure 3.3.3 A), led us to hypothesize that KRas membrane diffusion is in a steady state. To verify this, we divided each spt-PALM dataset with a minimum of 40,000 trajectories into four quarters (each with 10,000 trajectories and typically 5 min long) and computed the diffusion model for each quarter using vbSPT. As Figure 3.3.7 A shows, the model parameters for all four quarters were essentially identical, which is the case for all qualifying datasets, confirming that KRas diffusion is indeed in a steady state, at least in U2OS cells and at the investigated time scales (up to 20 minutes).

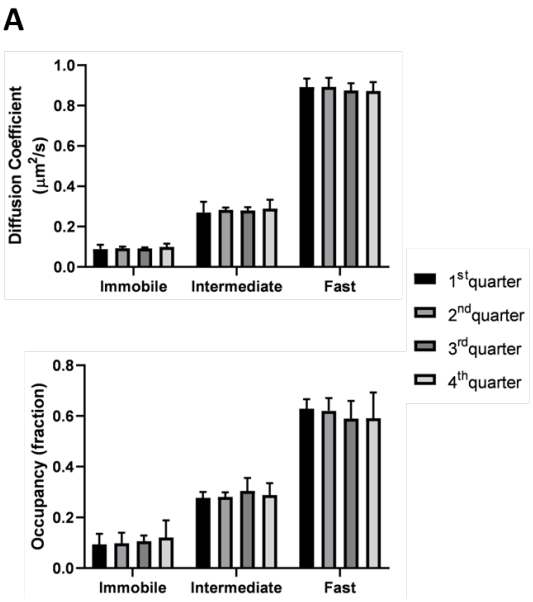

	Immobile	Intermediate	Fast
Calculated Equilibrium Occupancy	0.53 ± 0.09	0.24 ± 0.04	0.23 ± 0.07
Simulated Equilibrium Occupancy	0.50 ± 0.09	0.24 ± 0.04	0.25 ± 0.07
Observed Steady State Occupancy	0.11 ± 0.02	0.31 ± 0.03	0.58 ± 0.05

Figure 3.3.7: KRas diffusion on the cell membrane is in a non-equilibrium steady state. A) Time invariance of the KRas diffusion model. A single ∼20 min spt-PALM dataset was segmented into four quarters with each quarter containing ∼10,000 trajectories (in ∼5 mins), each analyzed separately using vbSPT to obtain the model parameters such as the diffusion coefficients (upper panel) and the state occupancies (lower panel). Results from multiple spt-PALM datasets were grouped and plotted (n=4); B) Temporal evolution of the KRas diffusion model in simulated runs. The system was setup according to the experimental model parameters (number of states, state occupancies, diffusion coefficients, and state transition rates) as shown in Figure 3.3.3 A. The system was then allowed to evolve based on the input, with the new state occupancies recorded every time step (12 ms) and plotted (see Methods). Similar to Figure 2A, only movies with minimum of 30,000 trajectories were simulated (n=8); C) Table summarizing the calculated, simulated, and experimentally observed occupancies for each of the states. *All error represents 95% CIs.

In contradiction to KRas diffusion being in a steady state, we found that the diffusion model as presented in Figure 3.3.3 A cannot self-sustain. When using experimentally derived model parameters to simulate how the three-state system evolves over time (see Methods), we observed that the system quickly deviated from its initial configuration and instead stabilized at an entirely different set of state occupancies (Figure 3.3.7 B). In the new, 'equilibrated' system configuration, KRas spends as much as 50% of its time in the immobile state, significantly more than the observed steady state occupancy of 11%. The fast state is the opposite; the population residing in this state is significantly reduced from 58% to 25%. By contrast, the intermediate state changes only slightly (31% vs 24% for the experimental and the theoretical observations, respectively). We confirmed that the simulated equilibrium probabilities were consistent with the principle of detailed balance49 (Figure 3.3.7 C); we also verified that the experimentally determined state occupancies in Figure 3.3.3 A were not an artifact of vbSPT, since vbSPT correctly retrieved the steady state model parameters when applied to simulated trajectories from steady state models with varying input parameters (Figure 3.3.8). Therefore, we concluded that the model in Figure 3.3.3 A represents a non-equilibrium steady state (NESS).

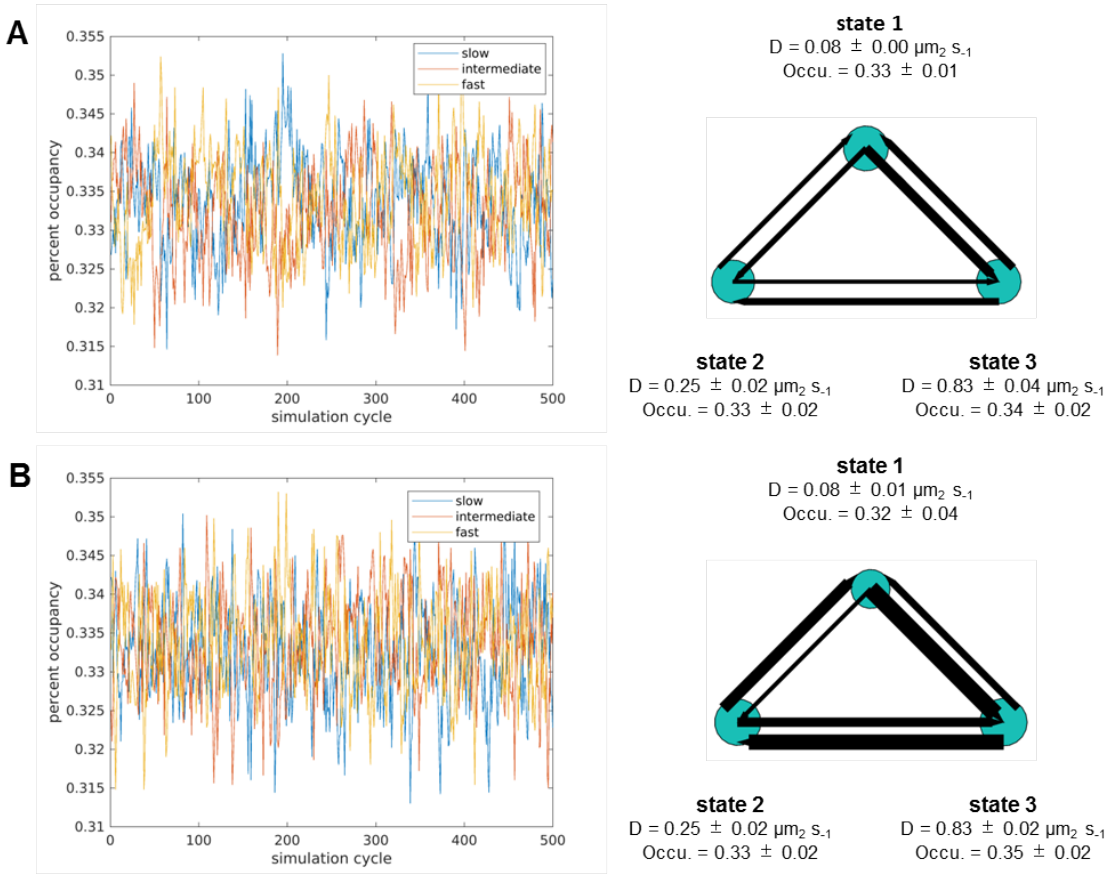

Figure 3.3.8: Validating vbSPT output accuracy on simulated trajectories using different model parameter inputs. We simulated steady state systems using three states, with diffusion coefficients of 0.08, 0.26, 0.84 μm^2/s and the same occupancy for each state (0.33). The state transition probabilities used for (A) were $p_i i = 0.8$ and $p_i j = 0.1$, which give rise to equal mass flow between each pairs of states; those used for (B) were $p_1 2 = p_2 3 = p_3 1 = 0.1$ (counter-clockwise) and $p_1 3 = p_3 2 = p_2 1 = 0.8$ (clockwise). Each simulation generated 5,000 trajectories, which were then analyzed using vbSPT; each model was simulated 5 times, and the exemplary models with averaged model parameters are shown on the right. The resulting diffusion parameter outputs confirm that vbSPT was able to accurately determine parameters for both balanced (A, right) and non-balanced (B, right) state transitions. Error bars show 95% confidence interval.

To further characterize the NESS, we calculated the mass flow for each of the three KRas diffusion states as the change in state occupancy per time interval. A positive net flow rate or a ratio of in- vs outflux greater than one indicates an accumulation of mass for the state, while a negative flow rate or a ratio of flux less than one indicates the opposite. As shown in Figures 3.3.9 A & B, within the NESS there is a net influx of KRas molecules into the immobile state and a net outflux of molecules out of the fast state, whereas the in- and outfluxes for the intermediate state are comparable. We also calculated the mass flow for each of the three arms in the diffusion model in Figure 3.3.3 A – in the clockwise direction, it would be the flow from the fast state to the intermediate state (F to N), intermediate to immobile (N to I), and immobile to fast (I to F). The results of this calculation are shown in Figure 3.3.9 C, where a positive value in the y axis (net mass flow between a pair of states) indicates mass flow in the designated direction, and a negative value indicates flow in the opposite direction. Consistent with results in Figures 3.3.9 A & B, the dominant net mass flow through the NESS is unidirectional – from the fast state to the intermediate to the immobile state (Figure 3.3.9 C) – with minimal 'leakage' from the fast to the immobile state.

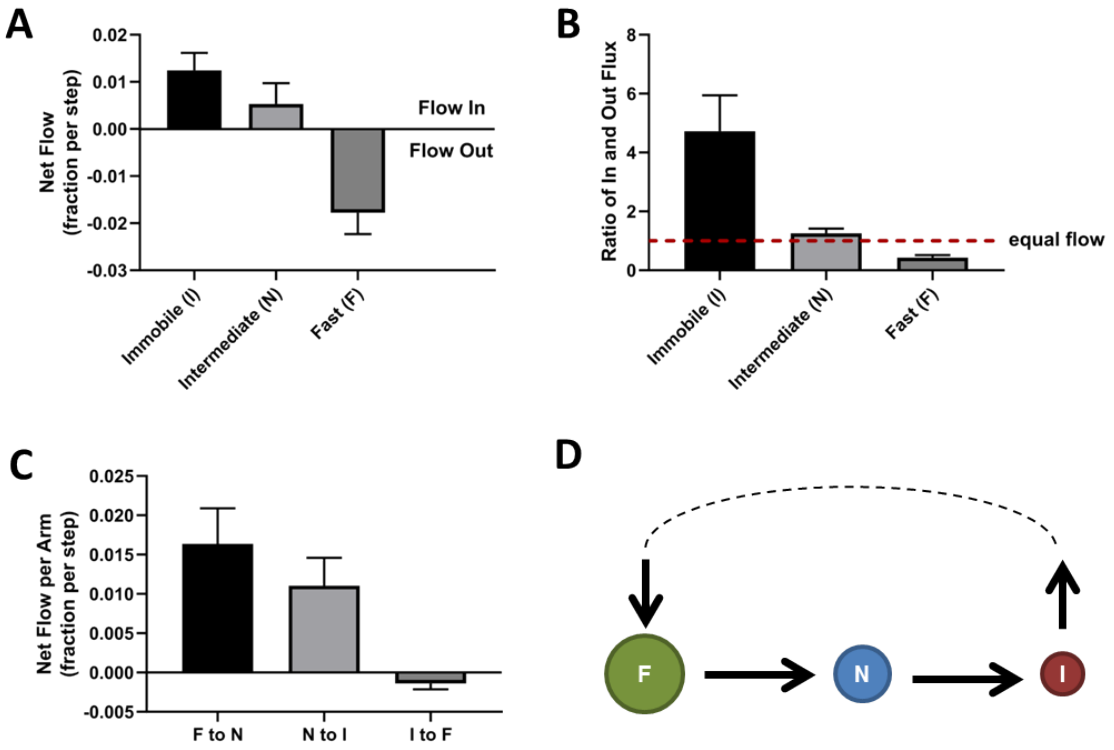

Figure 3.3.9: Directional mass flow between KRas diffusion states. A) Net mass flow per state, defined as the difference between the influx (positive) and the outflux (negative) for each state and expressed as the fraction (of total KRas population) entering (positive, flow in) or leaving (flow out, negative) the state per time interval; B) Ratio of in- and outflux for each state. A ratio of one (dashed line) represents equal in- and outflux for the state, greater than one represents more influx than outflux, and less than one represents net outflux of mass from the state; C) Net mass flow per arm (pair of states) in the KRas diffusion model (Figure 2A). F to N and N to I are not significantly different. The states were ordered in a clock-wise direction, and the net mass flow in the direction was calculated as the difference between forward and backward mass flows, with a positive value indicating net flow in the indicated direction and a negative value the opposite direction; D) Model for KRas trafficking between the diffusion states and between the membrane system and the environment (cytosol). Arrows indicate the directional mass flow, and the dashed line represents unknown mechanisms connecting the fast and the immobile states. *All error bars are 95% CIs (n=22).

These results are consistent with the simulated relaxation to equilibrium shown in Figure 3.3.7 B, where the immobile and the fast diffusion states changed occupancies the most. For the KRas NESS system to be sustained over time as we observed experimentally, KRas would need to be replenished into the fast diffusion state and removed from the immobile state. Indeed, KRas has previously been shown to undergo a constant exchange between the plasma membrane and the cytosol, and internalized KRas is collected at recycling endosomes and transported back to the plasma membrane [92, 93]. Our analyses suggest that the loss of KRas from the membrane would primarily be through the immobile state, and the replenishment through the fast state. At present, it is unclear whether the intermediate state has no exchange with the cytosol or has active exchange with equal gain and loss. Accordingly, the membrane trafficking of KRas should follow the model presented in Figure 3.3.9 D, where the arrows indicate the net mass flow between the connected states as well as between the states (F or I) and the environment (cytosol).

3.3.5 KRas diffusion and trafficking are invariant with expression level

Next, we sought to investigate whether experimental conditions such as expression level would alter the diffusion properties of KRas. An important observation on Ras nanocluster (multimer) formation is that the fraction of clustered molecules remains constant over a broad range of expression levels [25]. This unusual property has led to two hypothetical mechanisms of membrane nanocluster formation: one based on protein self-nucleation [25] and another involving actomyosin activity [94]. These active mechanisms are in contrast to passive localization of Ras to existing membrane nanodomains via diffusion, which is thought to result in concentration-dependent multimer formation. To date, it remains controversial as to which mechanism dictates Ras multimer formation. If Ras multimer formation was linked to localization to membrane nanodomains – which in the case of KRas would be the intermediate and/or the immobilization domains – then the observed fraction(s) of KRas in either or both the intermediate and the immobile states should also be independent of

expression level, as for the fraction of Ras molecules in multimers (clusters).

To address this hypothesis, we induced PAmCherry1-KRas G12D at a range of expression levels using different Dox concentrations (Figure 3.3.1 A). Similar to our previous report [34], the expression level of PAmCherry1-KRas G12D responded well to varying Dox concentrations in the isogenic cells used in this study, with the protein expression at 0 ng/mL being extremely low (only due to occasional leakage in tetR suppression) and that at 10 ng/mL about 5-10 fold higher than endogenous KRas. When measured in terms of protein density at the membrane, the endogenous level of KRas (matched by PAmCherry1-KRas G12D at $\sim$2 ng/mL Dox) in U2OS cells is $\sim$60 molecules per μm^2, and the tuning range corresponds to $<$10 molecules per μm^2 at 0 ng/mL Dox to $>$300 molecules per μm^2 at 10 ng/mL Dox, or equivalently $\sim$1/6 to $\sim$5 times of the endogenous levels of KRas [34].

By comparing estimated model parameters using spt-PALM data of PAmCherry1-KRas G12D at different Dox concentrations, we found that KRas diffusion properties remained essentially the same across the range of expression levels investigated (Figures 3.3.10 A-B and Figure 3.3.11). This model invariance is reflected across all conditions: not only was a three-state model optimal for describing the diffusion of KRas as judged with vbSPT (not shown) and with CDF (Figue 3.3.12), but the diffusion coefficients of each state, the state occupancies, as well as the transition probabilities between each pair of states, are indistinguishable within the error bars.

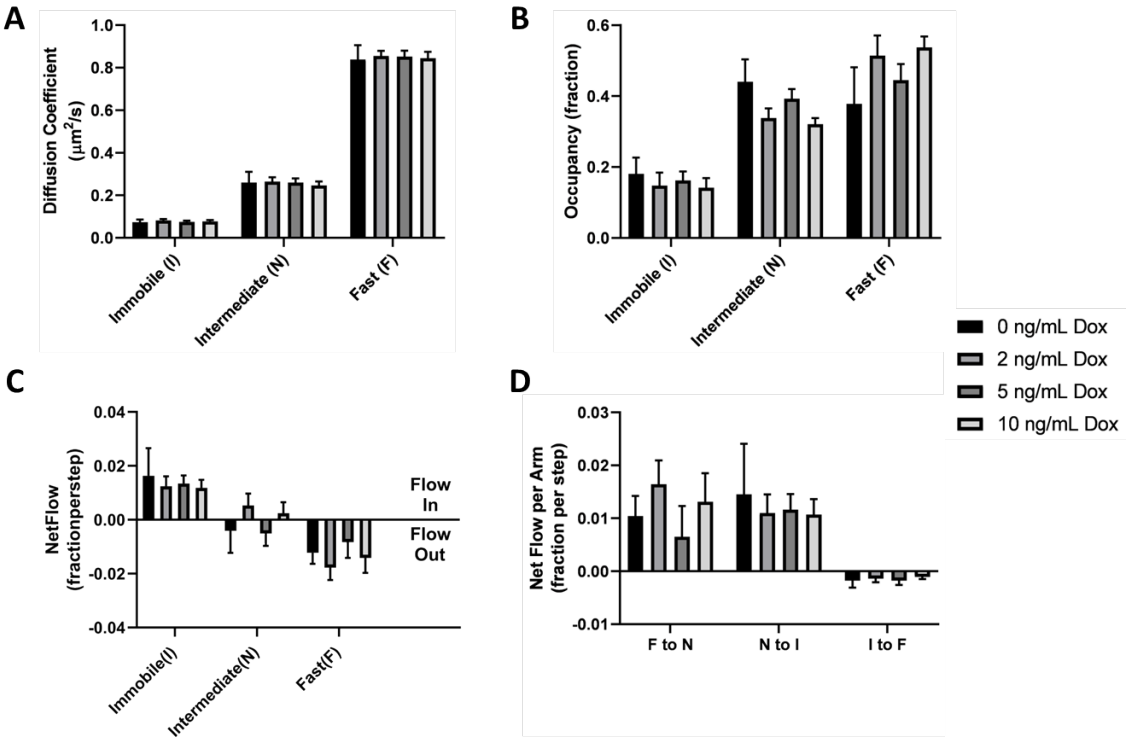

Figure 3.3.10: KRas diffusion properties remain constant over a broad range of expression levels. Spt-PALM trajectories of KRas were acquired at 12 ms/frame after inducing the cells at 0, 2, 5, and 10 ng/mL Dox for 36-48 hours, and the diffusion models were inferred as described previously using vbSPT. All aspects of the diffusion model discussed earlier, including diffusion coefficients (A), state occupancies (B), net mass flow per state (C), and net mass flow per arm (pair of states, D) at the different Dox concentrations were analyzed and compared. Error bars represent 95% CIs (n=12 for 0 ng/mL Dox, n=22 for 2 ng/mL Dox, n=30 for 5 ng/mL Dox, and n=18 for 10 ng/mL Dox).

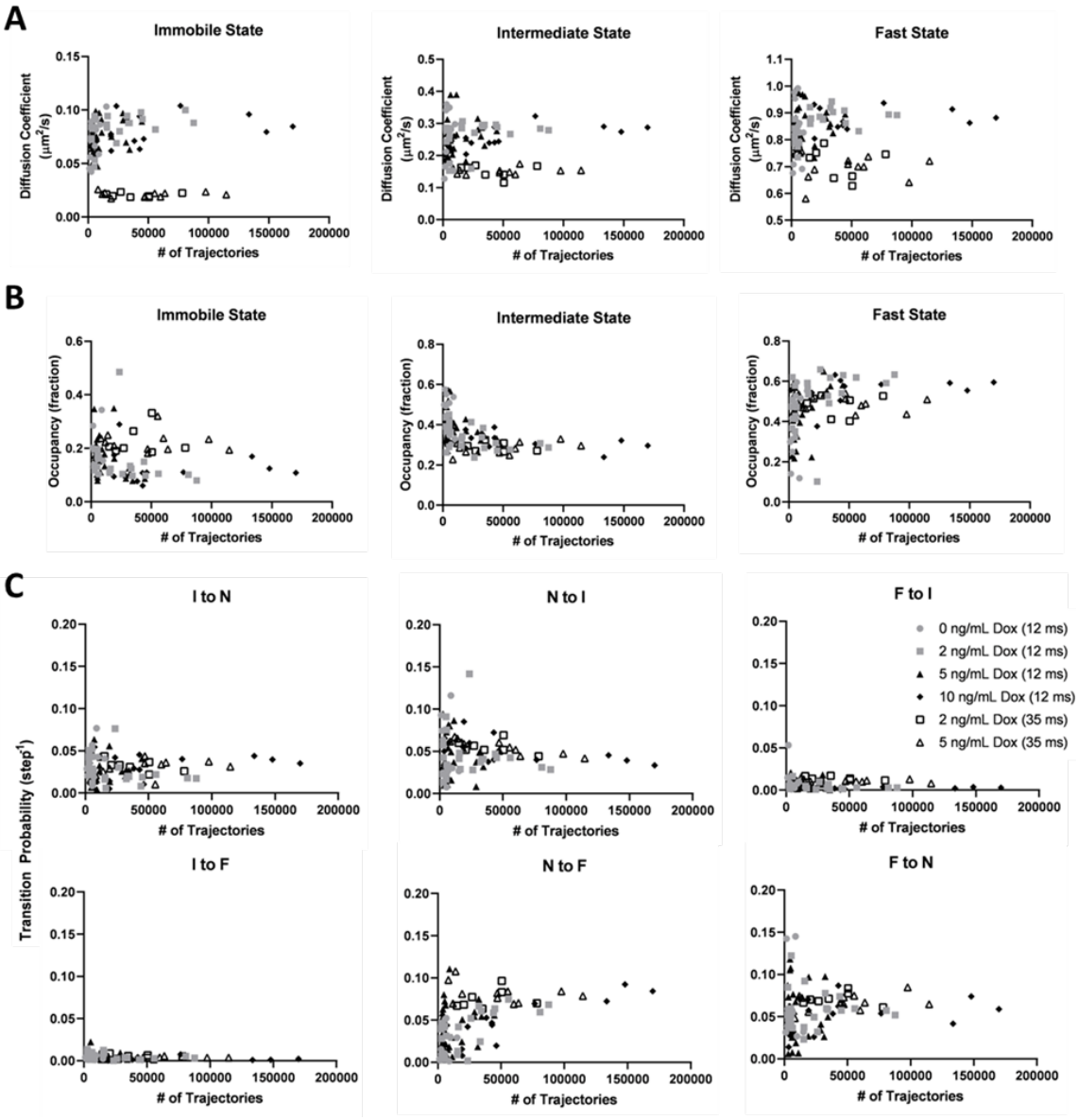
A
Immobile State
Intermediate State
Fast State
Diffusion Coefficient (μm²/s)
# of Trajectories
B
Immobile State
Intermediate State
Fast State
Occupancy (fraction)
# of Trajectories
C
I to N
N to I
F to I
I to F
N to F
F to N
Transition Probability (step⁻¹)
# of Trajectories
0 ng/mL Dox (12 ms)
2 ng/mL Dox (12 ms)
5 ng/mL Dox (12 ms)
10 ng/mL Dox (12 ms)
2 ng/mL Dox (35 ms)
5 ng/mL Dox (35 ms)

Figure 3.3.11: vbSPT model outputs from KRas diffusion trajectories acquired at different conditions (frame rate, total number of trajectories, and Dox concentration). All experimental spt-PALM data on PAmCherry1-KRas (in U2OS cells) acquired with 12 or 35 ms frame acquisition times and under 0, 2, 5, or 10 ng/mL Dox concentrations were pooled (symbols as indicated), and vbSPT outputs of the diffusion coefficients (A), state occupancies (B), and state transition probabilities (C) were plotted against the total number of trajectories. As shown in (A) and (B), the diffusion coefficients and the occupancies typically converge relatively quickly at a few thousand trajectories. Additionally, the diffusion coefficients derived from datasets obtained at 35 ms/frame are consistently lower than those obtained with 12 ms/frame datasets, a result of both localization precision (particularly for the immobile state) and trajectory smearing (predominantly for the faster diffusive states). Transition probabilities (C) required more trajectories to converge. However, all model parameters converged at similar values regardless of Dox concentration (i.e., KRas expression level). There are a total of 82 data points for the 12 ms dataset (n=12 for 0 ng/mL Dox, n=22 for 2 ng/mL Dox, n=30 for 5 ng/mL Dox, and n=18 for 10 ng/mL Dox), and 18 data points for the 35 ms frame rate (n=7 for 2 ng/mL Dox and n=11 for 5 ng/mL Dox).

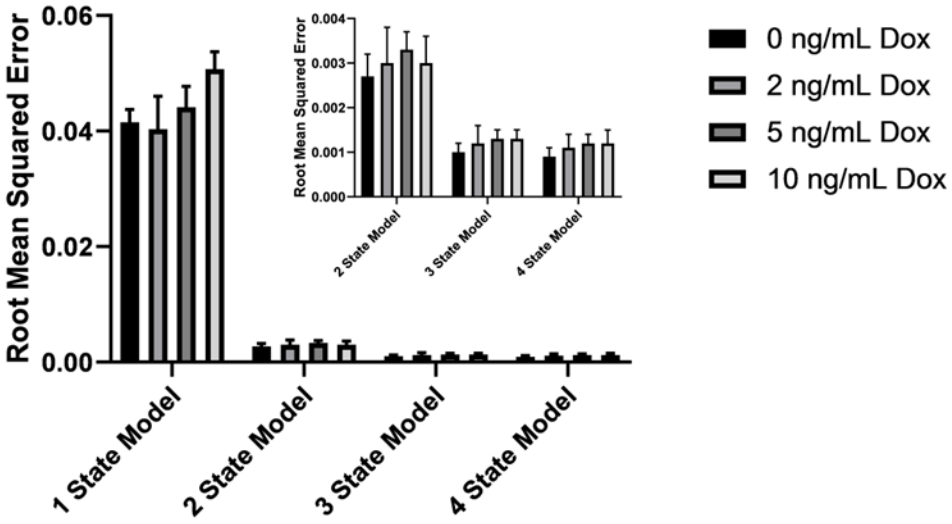

Figure 3.3.12: A three-state model remains optimal for describing KRas diffusion over a broad range of expression levels. The root mean squared error shown here is for CDF fitting of spt-PALM trajectories obtained at 0-10 ng/mL Dox (n=12 for 0 ng/mL Dox, n=22 for 2 ng/mL Dox, n=30 for 5 ng/mL Dox, and n=18 for 10 ng/mL Dox), with all trajectories acquired at optimal conditions (<0.03 particles/μm^2 per frame and frame acquisition time 12 ms/frame). CDF fitting was used to fit data to one, two, three, and four state models, and the residual errors were calculated (as in Fig. 1D).

As expected, the net mass flow rates (expressed as the change in state occupancy per time interval) of KRas within the system also remained the same across all the Dox concentrations (Figures 3.3.10 C&D). A similar observation was made when we acquired the trajectories at 35 ms/frame (Figure 3.3.13). Thus, we concluded that KRas diffusion and trafficking on the membrane remains constant over the range of tested KRas expression levels. Equivalently, the partitioning of KRas in each of the three diffusive states – and the corresponding membrane domains – is stable and independent of KRas protein density on the membrane. This result is consistent with the prior observation that the fraction of Ras in multimers remains constant at widely varying membrane densities [25].

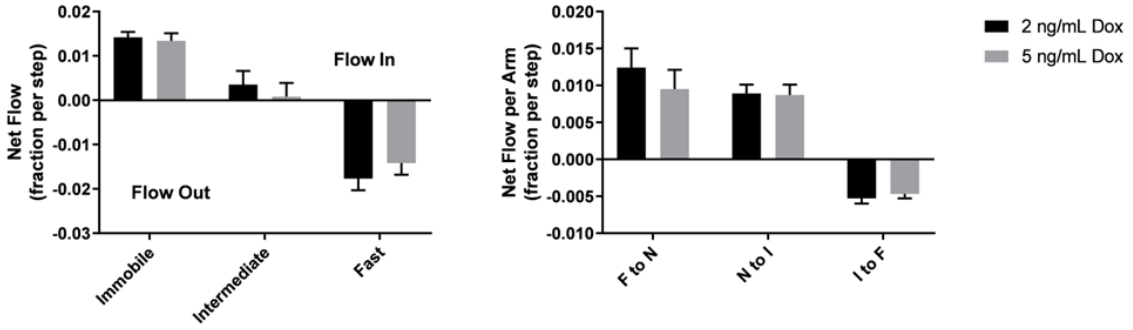

Figure 3.3.13: Net mass flow between KRas diffusion states is independent of expression level. Net flow analysis on datasets acquired at 35 ms/frame from cells induced to express PAmCherry1-KRas G12D at 2 or 5 ng/mL Dox.

3.4 Discussions/Conclusions

Membrane nanodomains have been implicated in the regulation of many membrane-resident cellular processes such as Ras signaling [65, 66, 67, 69, 68, 30], but studying the complex and heterogeneous membrane compartments in a living cell has remained a challenge. Using high-throughput SPT and detailed trajectory analysis, we were able to uncover rich details of how KRas localizes and interacts with the membrane. Our results suggest that KRas diffusion on the membrane is best reca-

pitulated with a model that comprises three states – a fast state, an immobile state, and a previously unknown intermediate state. Leveraging the large number of diffusion trajectories, we were able to map the locations where KRas exhibits specific diffusion states. These maps revealed membrane nanodomains corresponding to the intermediate and the immobile states of KRas. The intermediate nanodomains encompass the immobilization sites in a nested configuration, such that KRas almost always transitions between the fast and the immobile states through the intermediate state. We also found that KRas membrane diffusion is in a non-equilibrium steady state, with KRas constitutively removed from the membrane through the immobile sites and replenished as fast diffusing molecules, potentially coupled to KRas trafficking via endocytosis and recycling. Importantly, partitioning of KRas into the three states remains invariant over a wide range of KRas expression levels, demonstrating that KRas diffusion and trafficking through the three mobility states and associated nanodomains is in a maintained, homeostatic condition. Together, these data start to paint a clear picture of the spatiotemporal dynamics of KRas on the membrane, providing the basis for understanding the mechanisms of Ras multimer formation and signaling.

Based on these findings, we propose a new model for Ras membrane diffusion and trafficking as shown in Figure 3.4.1. In this model, Ras experiences at least three types of membrane environments: a 'regular' membrane region in which Ras freely diffuses with large step sizes, a 'transition zone' or intermediate domain with increased viscous drag and reduced step size, and within the latter an 'immobilization' site where Ras interacts with relatively static structures (such as endocytic vesicles). Both the transition zones and the immobilization sites have finite life times, some up to minutes, during which freely diffusing KRas molecules could enter the transition zone, slow down, then either return to the fast state or become trapped in the immobilization sites. During entrapment, a fraction of the trapped KRas molecules leaves the plasma membrane to enter a constitutive cycle of KRas trafficking. This is in agreement with the current understanding that the rate of KRas removal from the membrane through endocytosis is a concentration dependent process, and the localization of KRas at the plasma membrane is an energy driven, PDEδ and Arl2

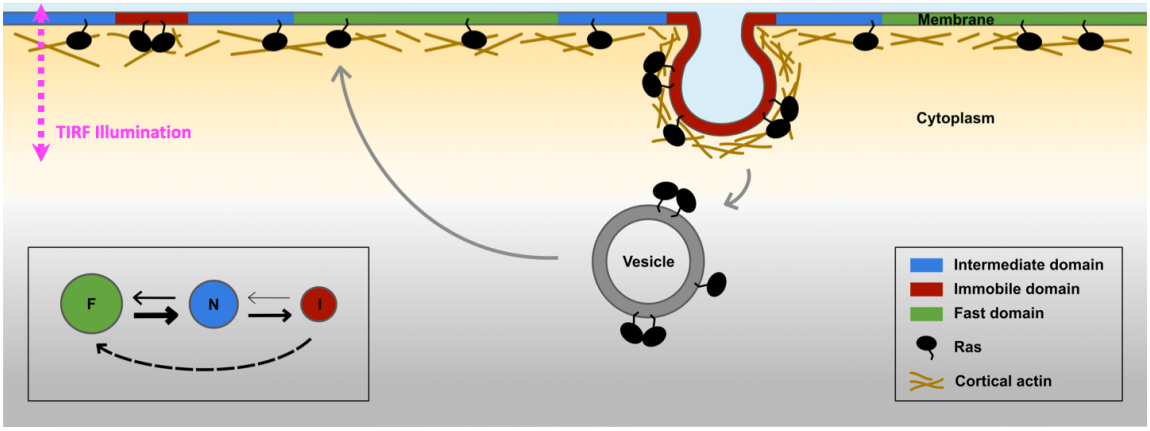

Figure 3.4.1: Proposed model for membrane nanodomains regulating KRas mobility and trafficking. For KRas, the cell membrane comprises of at least three different compartments conferring each of the three diffusion states of KRas, namely the fast (and free), the intermediate, and the immobile diffusion states, depicted as green, blue, and red regions, respectively. The membrane compartments associated with the immobile and the intermediate states of KRas are nanoscopic membrane structures, and at least a subset of the KRas immobilization structures are attributed to endocytic vesicles. KRas is continuously removed from the immobile state, possibly through endocytosis, and the internalized KRas molecules are subsequently transported back to the membrane as fast diffusing species through recycling. KRas immobilization domains such as endocytic vesicles could locally enrich KRas molecules to facilitate KRas multimer formation and potentially signaling. The arrows in the legend reflect net flow between each state.

mediated enrichment of KRas in recycling endosomes which collect and transport KRas back to the plasma membrane [92, 93]. Our work adds important details to this trafficking model in that the removal of KRas from the plasma membrane likely occurs during the entrapment phase and its recycling primarily takes place in membrane regions conferring fast mobility. Additionally, the transient entrapment of KRas could also provide an effective mechanism to locally concentrate Ras molecules to facilitate multimer formation, which arguably is a critical step for signaling [32, 95]. Thus, the various membrane nanodomains directly influence the mobility, trafficking, and potentially multimer formation and signaling of KRas.

The three-state diffusion model proposed in this study refines existing models of KRas membrane diffusion by introducing a previously unresolved intermediate state, and capturing the role of membrane nanodomains in KRas diffusion. While heterogeneous diffusion properties of KRas and other Ras isoforms have been reported, the prior studies lacked the throughput or spatiotemporal resolutions to determine whether two states, namely a fast diffusion state and an immobile state, are adequate to recapitulate KRas diffusion on the membrane. With the diffusion model defined, we were able to subsequently demonstrate that the intermediate and immobile states of KRas are each associated with a distinct membrane domain. The average sizes of the immobile and the intermediate domains of KRas were found to be 70 nm and 200 nm, respectively, consistent with previous notion that nanoscopic membrane domains regulate Ras organization on the membrane. We note that, although a three-state model best fits our data, the model could still be an over-simplification. Among other possibilities, both endocytic and non-endocytic mechanisms may contribute to the immobilization of Ras but cannot be distinguished based on diffusion properties since Ras is immobile in both cases. In fact, there are also indications of more than one type of intermediate domains judging from the estimated domain size (Figure 3.3.3 F).

A unique feature of the model in Figure 3.4.1 is that the membrane nanodomains associated with the immobile state of KRas are surrounded by those associated with the intermediate state, creating a nested configuration between the two nanodomains. A plausible scenario is that the structures that trap KRas preferentially form in the membrane regions enriched in certain proteins or lipids and/or more densely packed. In this scenario, KRas would be forced to travel through the intermediate zone to access the immobilization structures, explaining the state transition pathway in Figure 3.3.3 A. This scenario is also consistent with the observation that the intermediate domains are on average much larger in size than the immobile domains, and that the two nanodomains have similar life times (to the extent of our temporal resolution). In support of this hypothetic scenario, a growing body of literature demonstrates the importance of phosphatidylserine in KRas clustering and activation [27, 96, 28, 24]. In addition to the KRas tail encoding for phosphatidylserine specificity, a significant

fraction of phosphatidylserine display slow motion on the membrane as well [28, 18].

Aside from the steady state partitioning of KRas in the different membrane domains, our data also offered important insight into the membrane dynamics of KRas. We measured a constant flow of KRas from the fast state to the immobile state. Without exchanging KRas with the cytosol, this directional flow would have caused net loss of KRas from the fast state and accumulation in the immobile state as described in Figure 3.3.7 B-C, yet the experimentally observed state configuration (Figure 3.3.3 A) remained stable over time (Figure 3.3.7 A). We therefore reasoned that KRas needs to be constantly removed from the immobile state ('sink') and replenished via the fast state ('source'), potentially coupled to membrane trafficking such as endocytosis and recycling [92, 93, 97, 98, 99]. Previous studies have shown that endocytosis is a primary mechanism for KRas removal from the plasma membrane [92]. Thus, our data indicate that at least a subset of the immobile domains could coincide with endocytic vesicles. In support of this, the life time of the immobilization domains was estimated to be on the order of 2-5 minutes on average (Figure 3.3.6 A-B), which is typical of many endocytic systems [100, 101]. The exact mechanism of KRas internalization, however, remains incompletely understood at present.

It is noteworthy that the spatial partitioning of KRas and more generally the diffusion model were invariant over a broad range of KRas expression levels, which coincides with previous observations where the clustered fraction of KRas or HRas was independent of the protein expression level [25, 32]. This corroborates the idea that membrane partitioning of Ras and perhaps many other membrane resident molecules are in an actively maintained, homeostatic condition. This intriguing property of certain membrane proteins [25, 102] has drawn much attention and led to at least two mechanistic models of multimer formation, one based on self-nucleation [25] and the other driven by actomyosin [94]. Both mechanisms assumed the different states of the protein on the plasma membrane to be in equilibrium. Our results argue that the mass exchange between the plasma membrane and the cytosol breaks the equilibrium and has to be taken into account in order to accurately model the partitioning behavior of membrane proteins. It is possible that the model presented

in Figure 3.4.1 in combination with either self-nucleation or actomyosin activity could provide a better description of the observed model invariance of KRas and potentially other membrane proteins. A clear, mechanistic understanding of this property is important to understand how Ras functions on the membrane, since the Ras multimers have been strongly implicated in signaling. Further experimental and computational work along this line is currently underway.

In summary, our work sheds new light on how complex nanodomains organize on the membrane to dictate Ras diffusion and trafficking. The insights gained from this study offer useful guidance to future experiments that aim at determining the molecular and structural identities of the Ras-associated membrane nanodomains and defining the mechanisms of Ras multimer formation and signaling. The results demonstrate the utility of high-throughput SPT and trajectory analysis in uncovering rich details of the spatiotemporal dynamics of Ras on the membrane, which should be readily applicable to studies of other membrane molecules or processes in cellular compartments.

Chapter 4

Isoform dependent Ras interaction with different membrane structures for multimer formation and signaling

This chapter is currently a manuscript in preparation with myself and Dr. Ying Zhang as co-first authors. Dr. Ying Zhang is responsible for developing the CLEM protocol, CLEM image acquisition and registration, while I am responsible for acquiring the live cell single particle tracking and the analysis, clustering algorithm to define domains, and generating the random molecule fraction and identifying Ras clusters in CLEM data.

4.1 Introduction

In the last chapter, we discovered that the membrane can be broadly categorized into three different regions that can be identified by their effects on Ras diffusion as Ras travels through these domains. Further, we discovered that the membrane is organized in a hierarchical fashion where immobile domains are nested within inter-

mediate domains which reside in fast regions (default membrane). In this chapter, we attempt to identify and characterize the immobile and intermediate domains for K and HRas. The CLEM results shown here in this chapter was acquired by Dr. Ying Zhang [103].

4.2 Data analysis methods

4.2.1 Algorithm to define domains

Since the Ras-associated membrane domains are defined by the diffusion state of the Ras molecule, immobile and intermediate domains were identified based on the x, y coordinates from Ras trajectories associated with either immobile or intermediate diffusion states using vbSPT for the state labeling [58]. Assuming a nested domain structure identified in the previous chapter, immobile and intermediate domains were identified by merging trajectories overlapping in space and clustered in time for either immobile or intermediate state coordinates.

The main core of the clustering algorithm is as described below (Figure 4.2.1), with user inputs for the diffusion state to be clustered (either immobile or intermediate), localization error, minimum number of consecutive terminating and growing points (n), and the maximum number of frames:

1. shorten the movie to the maximum number of frames by discarding frames beyond the maximum

2. a trajectory is identified as domain trajectory if it has a minimum of 3 points for the state being clustered

3. for each trajectory with at least 3 points in a given state determine its convex hull:

3a. expand the convex hull by localization error (current value: 20 nm)

3b. if there is a minimum of n consecutive terminating points inside of the convex hull, assume that the domain has been terminated (terminating event), and bound the time window for adding other trajectories to this domain

3c. if there is a minimum of n consecutive points of the same state (growing points) in the time between terminating events, assume that the domain was present during those times and add those trajectories to the domain

4. define domains based on the domain trajectories

The state that is being clustered will determine the points used to grow and terminate clusters. For immobile domains, coordinates associated with the immobile state were used to add trajectories to domains (growing points) while intermediate and fast state coordinates will restrict the time period used to search for other immobile points within the domain boundary (terminating points). Intermediate domains will be terminated by fast state and grown by intermediate state coordinates.

Since state labels are given for displacements between two time points, both ends of the line were included when assigning states to trajectory coordinates. As such, points of transition were duplicated and categorized under both states. For example, if a trajectory transitioned from immobile to intermediate state, the point that is shared by both immobile and intermediate segments is labeled as both immobile and intermediate. However, terminating points that transitioned from a growing point was not used to terminate domains since these terminating points could have been misclassified or mislocalized as being inside of the domain.

Three different minimum growing and terminating parameters were tested (2, 3, 4). The minimum threshold reflect our belief in whether a series of consecutive points for a given state was due to a real physical structure or an artifact of mislabeling or mislocalization. Therefore, the growing and terminating thresholds were both set to the same value. There was no significant difference for the immobile domain identification between the three thresholds (Figure 4.2.2).

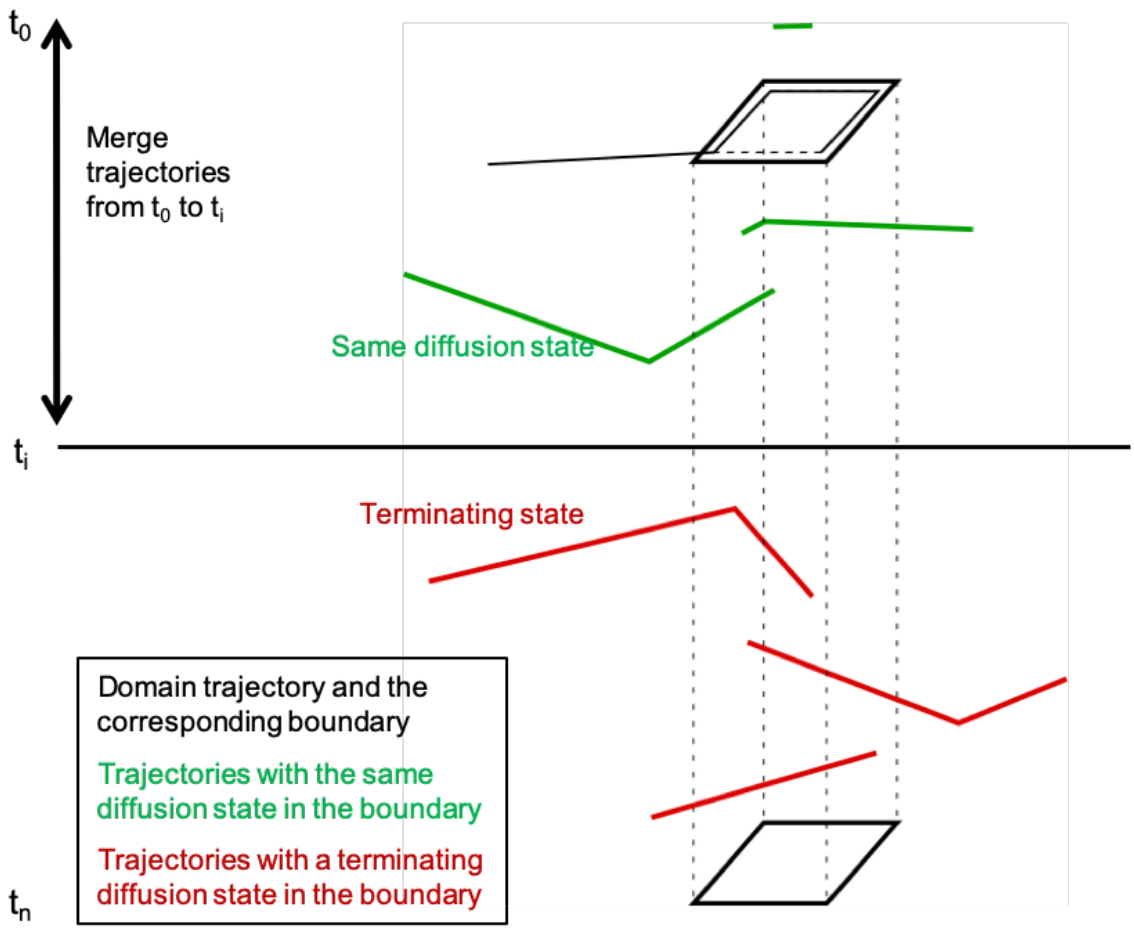

Figure 4.2.1: An example of the domain clustering algorithm. The y-axis indicates time, where t_0 is the start and t_n is the end of the movie. The black line is a trajectory with a minimum of 3 points that is currently being clustered (step 2). The green lines indicate other trajectories with the same diffusion state that are being used to grow the domain (step 3c) while the red circles indicate trajectories with diffusion states that terminate the domain and prevent it from growing past t_i (step 3b).

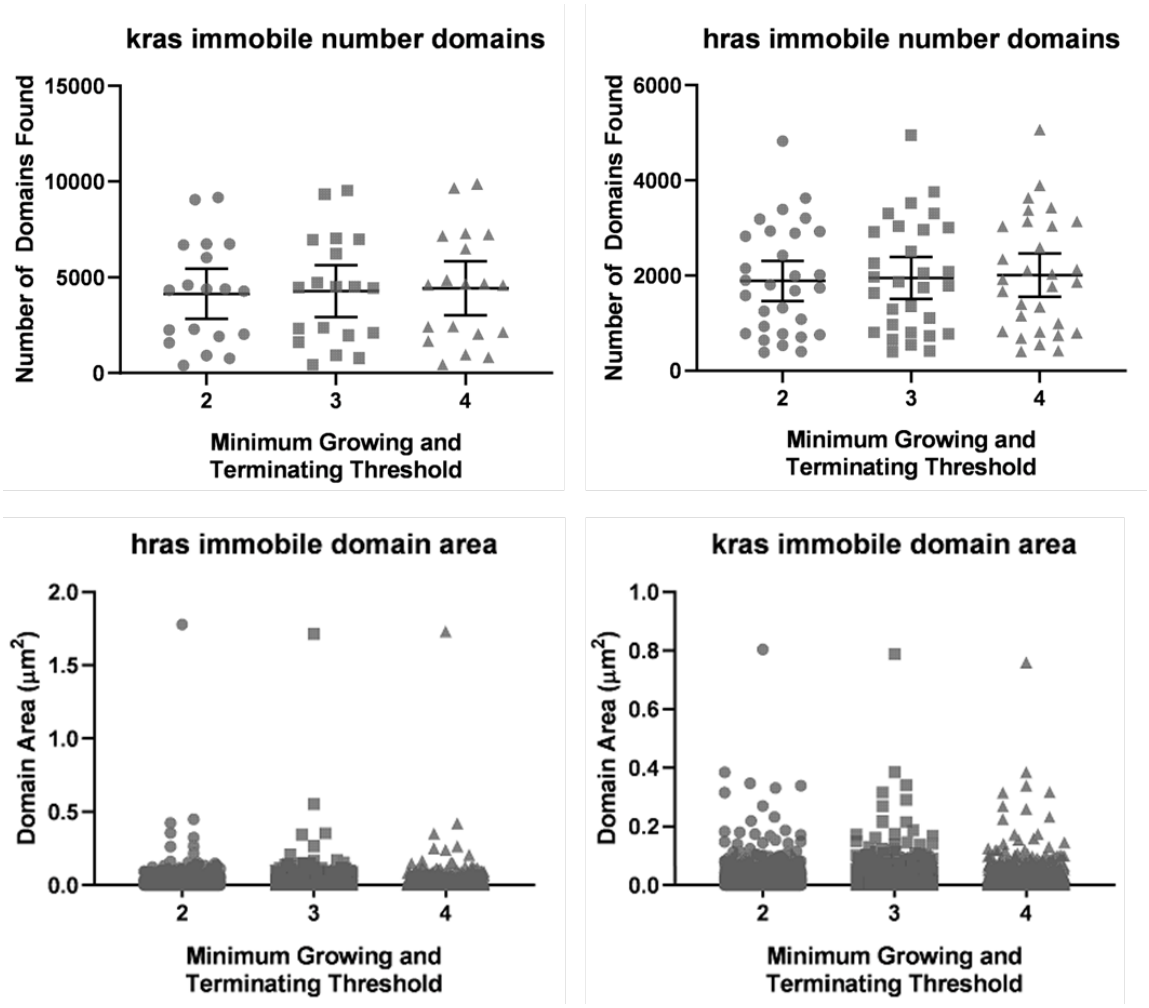

Figure 4.2.2: The effect of minimum clustering parameters on immobile domain construction.

This is most likely due to the fact that immobile domains are small and tightly clustered. Although, intermediate domains were more affected by the choice of terminating and growing parameter, the domain area did not change significantly (Figure 4.2.3). As the threshold was increased, the number of domains identified increased due the fracturing of domains, while the outliers for the domain area decreased. For the rest of the analysis, a minimum of 3 points was used to grow and terminate domains.

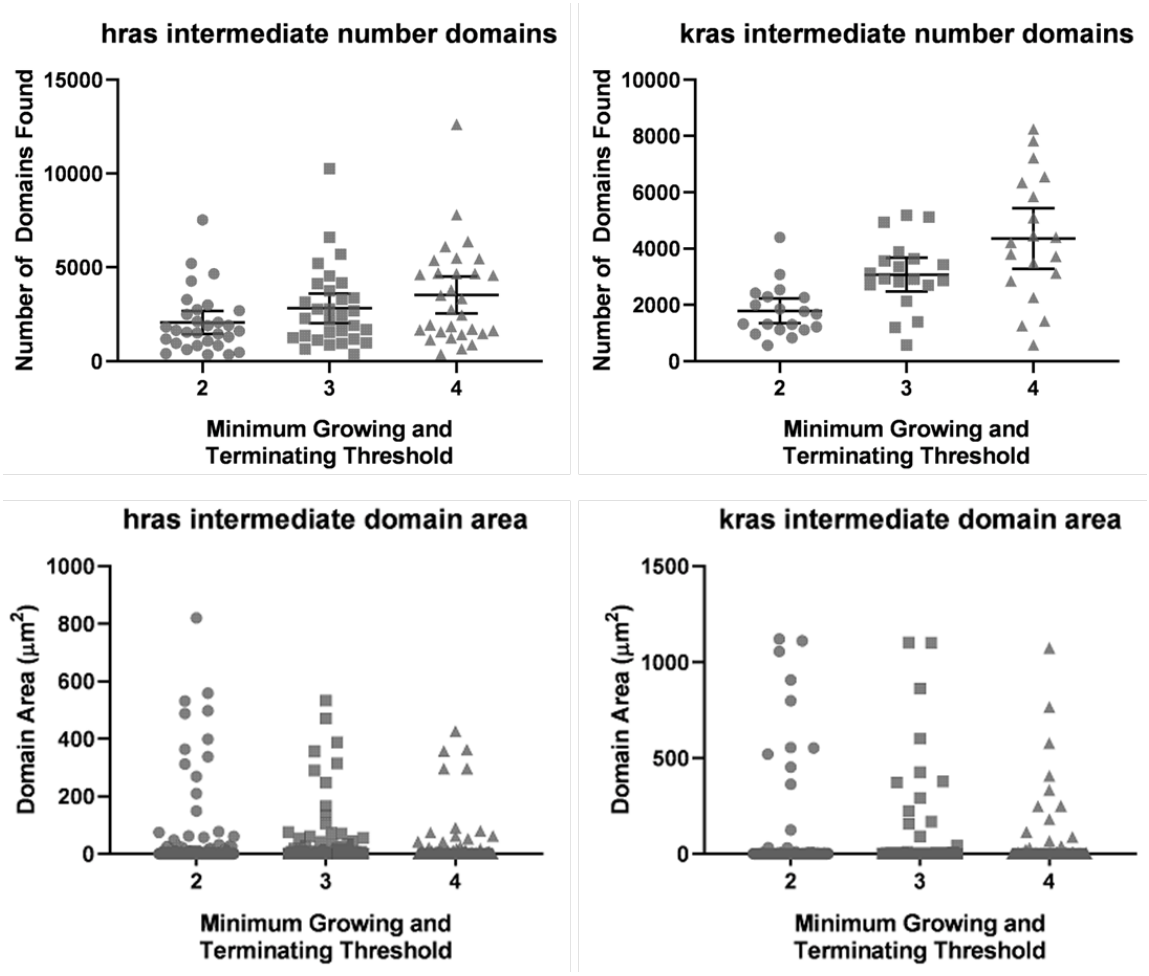

Figure 4.2.3: The effect of minimum clustering parameters on intermediate domain construction.

4.3 Results

4.3.1 KRas WT and G12D mutant have similar diffusion and trafficking properties

To determine whether this was nucleotide specific membrane behavior, we characterized the lateral diffusion properties of membrane bound KRas WT. Similar to KRas G12D, KRas WT tagged with PAmCherry1 was placed under doxycycline regulation. KRas WT single particle trajectories were collected following the same procedure as KRas G12D. As Figure 4.3.1 shows, using the same method as KRas G12D, the optimal model for KRas WT was also a 3 state model. Further, KRas WT had similar diffusion properties as KRas G12D. The diffusion coefficients, which define each of the 3 diffusion states are the same as the diffusion states that define the 3 KRas G12D diffusion states (Figure 4.3.2). KRas WT diffusion parameters (diffusion coefficients, occupancies and the transition probabilities) track very closely to KRas G12D (Figure 4.3.2). Although there is not enough data to conclusively establish a difference between the KRas-GTP and KRas-GDP diffusion models, KRas WT seems to have higher fraction of immobile and lower fraction of fast state populations compared to KRas G12D.

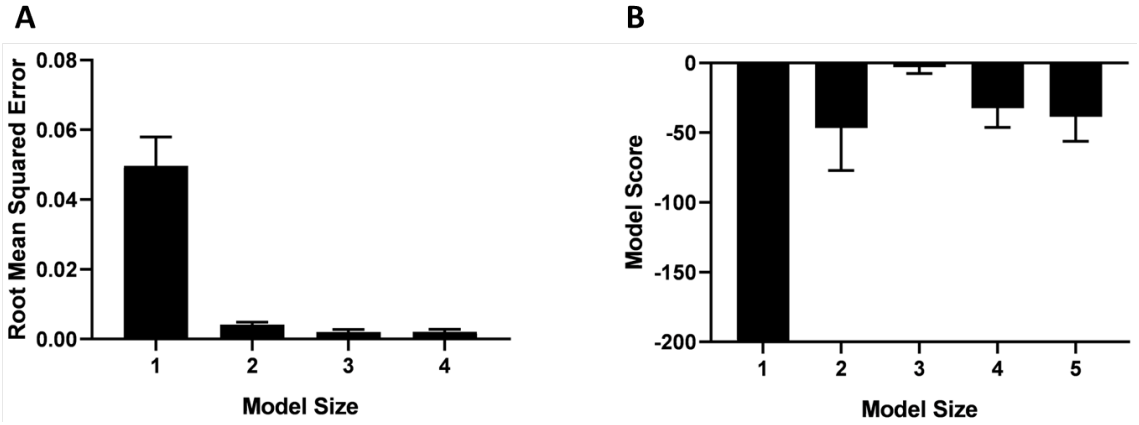

Figure 4.3.1: Defining the membrane diffusion model size for KRas WT using CDF fit (A) and vbSPT (B). Both CDF fit and vbSPT agree that the optimal model size for KRas WT is a three-state model.

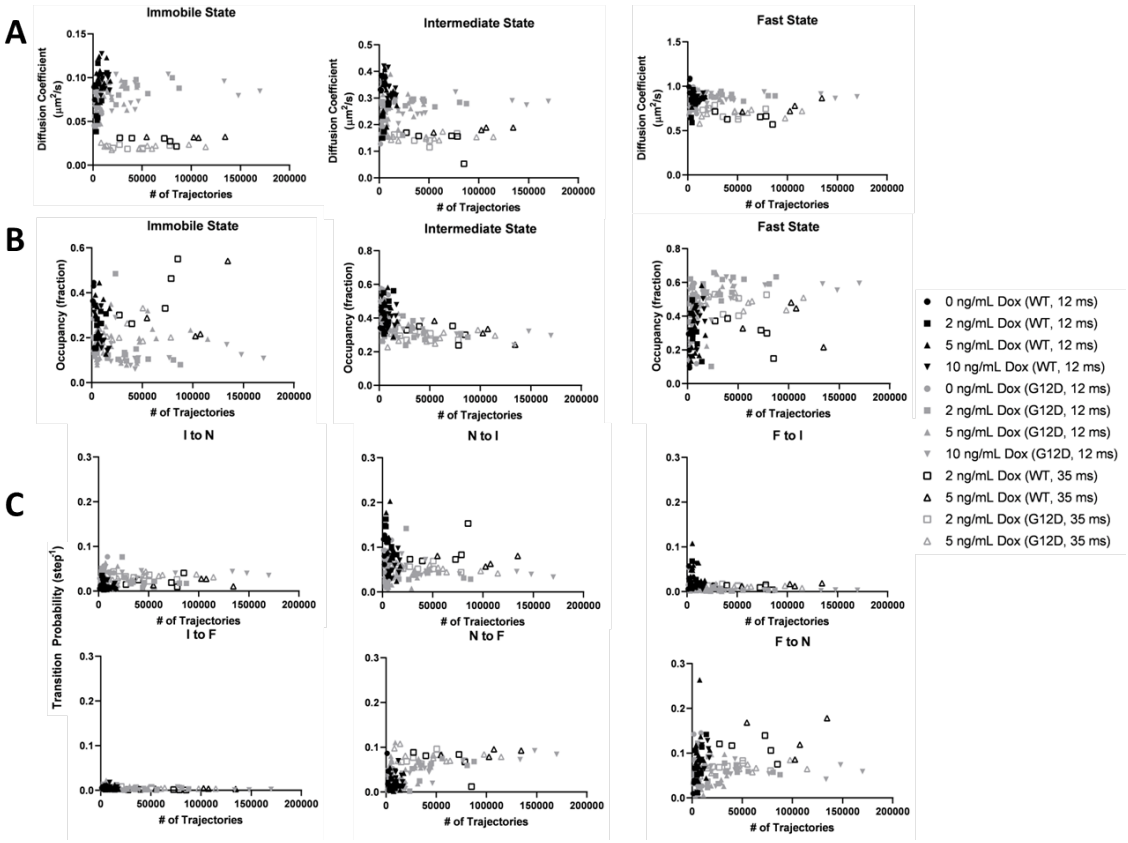

Figure 4.3.2: vbSPT model outputs for KRas WT single particle tracking data with the same conditions as KRas G12D shown in Figure 3.3.11 (frame rate, total number of trajectories, and Dox concentration). The state diffusion coefficients (A), occupancies (B), and transition probabilities (C) are plotted against the total number of trajectories. Majority of data points track very closely with KRas G12D, except for the immobile and the fast state occupancies (B).

Further, KRas WT appears to have the same nested domain structure as KRas G12D. As Figure 4.3.3 shows, immobile and intermediate KRas WT domains are tightly clustered indicating a physical location that slows down the diffusion of KRas WT molecules as they travel through that region. Although the data set is somewhat incomplete, the pair correlation function for KRas WT seems similar to KRas G12D. Further, the net mass flow for each state and between each states are the same as GTP bound KRas. The net flow analysis shows that KRas WT flows from the fast state, through the intermediate state, and accumulates in the immobile state. Hence, Figure 4.3.4 shows net loss of KRas from the fast state and net mass gain in the immobile state. Further, net mass flow between states show that the fraction of KRas WT molecules that flow from the fast to intermediate is not significantly different from the flow from the intermediate to immobile states. In order to get accurate results, only data sets with a minimum of 10,000 trajectories were used for the flow analysis. Transition probabilities, in particular, require significantly more data to infer. As such, only 35 ms data is shown because there was not enough of the 12 ms data set with a minimum of 10,000 trajectories. This also indicates that KRas is deposited on the membrane in the fast membrane region while being removed from the membrane from the immobile domains. Thus, our findings here show that GDP bound KRas follows a similar membrane organization as GTP bound KRas.

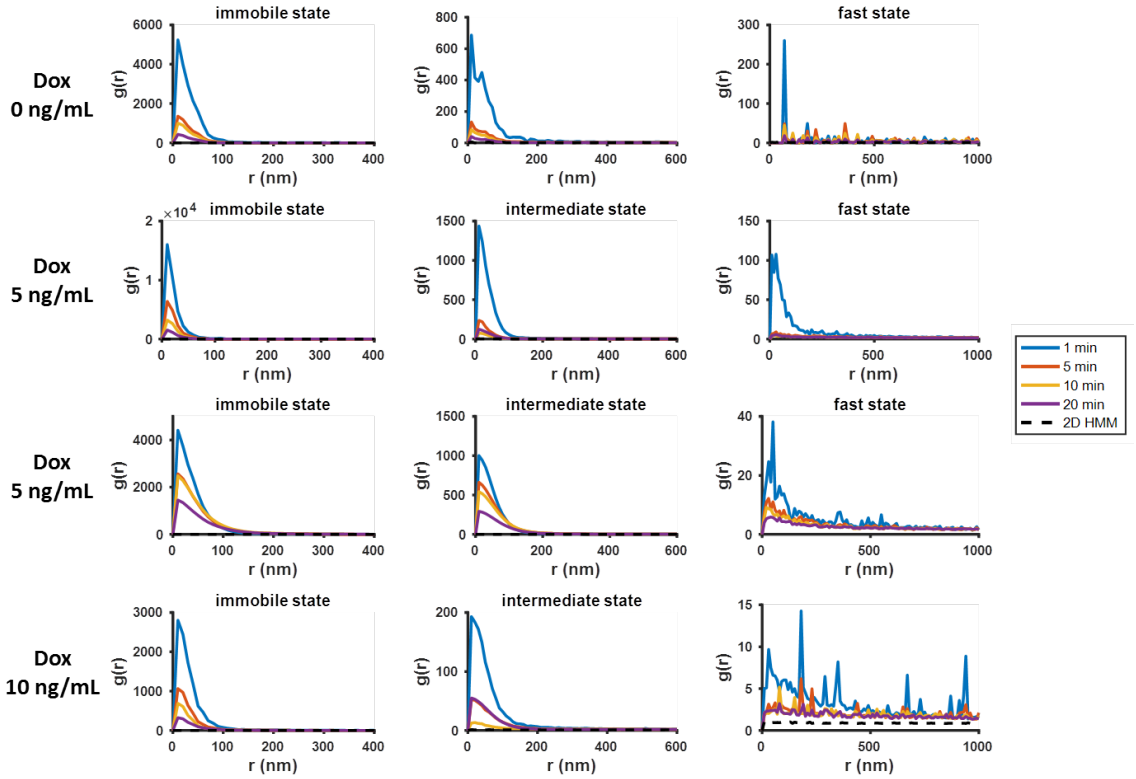

Figure 4.3.3: Spatiotemporal analysis of the KRas WT diffusion states. Pair correlation analysis was performed for KRas WT state coordinates at different time intervals (1, 5, 19, and 20 min) for each Dox condition (see Figures 3.3.3 & 3.3.6). Similar to KRas G12D, the spatial locations for the immobile and the intermediate diffusion states are clustered, implying that these are caused by underlying membrane domains, and the peak amplitude show that clustering peaks at 1-5 minutes. The negative control for each condition was generated using the 2D markovian simulation mentioned previously. The spikes in the $g(r)$ for the 0 ng/mL Dox fast state condition are due to the lack of trajectories in the 0 ng/mL Dox condition. When no Dox is added, minimal Ras is expressed from the leaky promotor. If there are only a few points, then random clustering can produce significant signals.

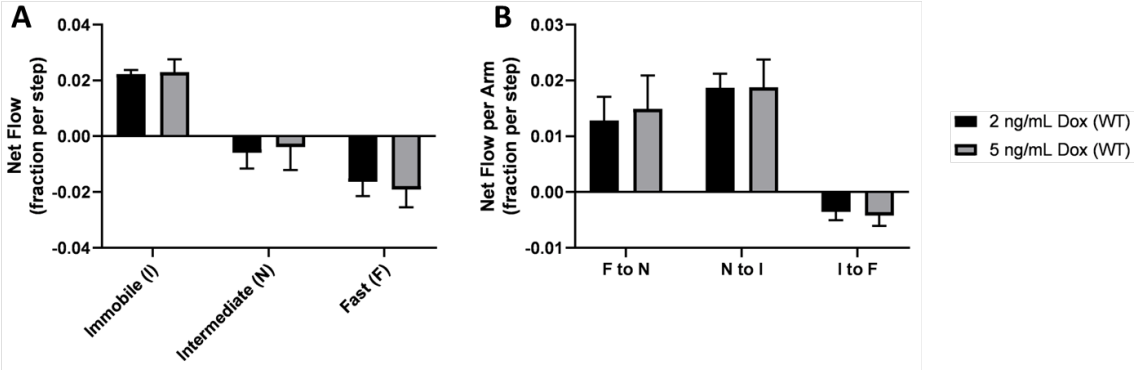

Figure 4.3.4: KRas WT net flow. Net mass flow for KRas WT remains unchanged for low (2 ng/mL Dox) and high (5 ng/mL Dox) expression levels. Using the same method as KRas G12D, the net flows for each state (A) and between each states (B) were calculated. Error bars represent % CIs. Due to lack of 12 ms data with minimum of 10,000 trajectories, the net flow analysis was restricted to the 35 ms dataset.

4.3.2 KRas G12D and HRas G12V show significant differences in the membrane diffusion model

Given that HRas has the most different tail from KRas, next we investigated the difference in lateral diffusion between KRas and HRas. In order to be have a fair comparison, we generated the HRas cell line using the same parental cell line and the same construct. The PAmCherry1-HRas G12V fusion protein was placed under a CMV promoter regulated by the Tet operon and transduced via lentivirus into a U2OS-tetR cell line with constitutive tetR expression. The HRas diffusion model was constructed using the same experimental and analysis set up as described for KRas. Contrary to our expectations, HRas membrane diffusion had many similarities to KRas diffusion. Similar to KRas, the optimal model size for HRas comprised of 3 diffusion states (Figure 4.3.5). More specifically, HRas also did not have any direct transitions between the fast and the immobile states, and the direction of net mass flow for each of the three states were similar between the two isoforms as well (Figures 4.3.6 & 4.3.9). The intermediate state for both isoforms had roughly equal flow into

and out of the state while the immobile and the fast states for both H and KRas showed faster flow into and out of those two states, respectively. Hence, analogous to the KRas membrane organization and trafficking, pair correlation analysis and net flow analysis (figures 4.3.8 & 4.3.9) suggested that HRas diffusion states are also caused by nested membrane domains that modulate HRas diffusion with HRas being replenished in the fast membrane region and endocytosis in the immobile domains (to be discussed in more depth in Chapter 4). However, there are significant differences between the KRas G12D and HRas G12V membrane diffusion behavior. For instance, the fast state is significantly faster for HRas than KRas ($\sim 1.1\ \mu m^2$/s vs $\sim 0.9\ \mu m^2$/s), and HRas had significantly more molecules in the fast state and less in the intermediate state (Figures 4.3.6 & 4.3.7). These differences suggest that the Ras tail plays an important role in Ras-membrane interactions.

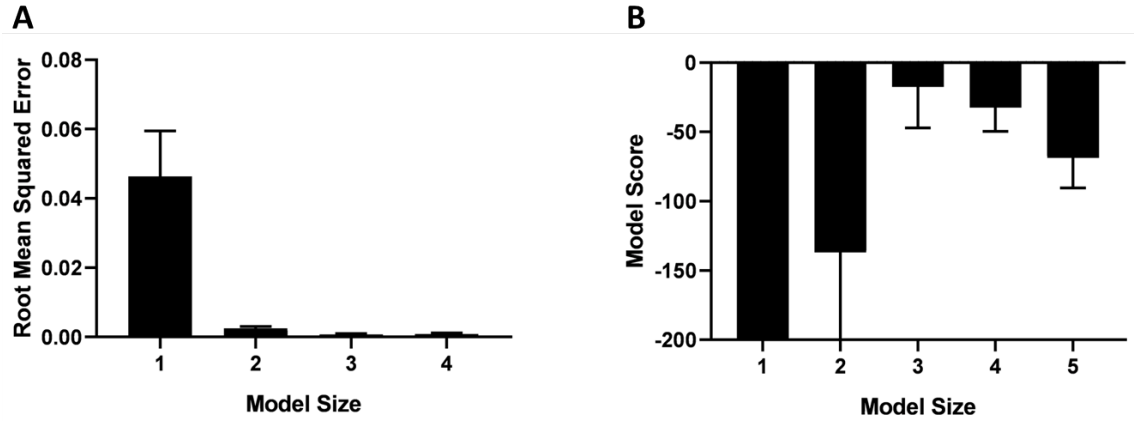

Figure 4.3.5: HRas is also a three-state model. Using the same method as described previously for KRas G12D and WT, the optimal membrane diffusion model size was calculated for HRas G12V using CDF fit (A) and vbSPT (B). Similar to KRas, HRas also displays three diffusion states on the membrane.

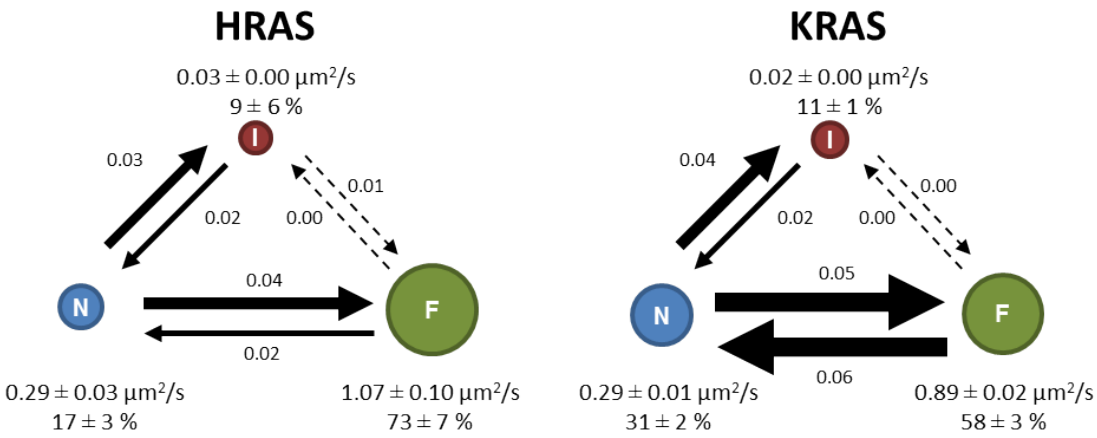

Figure 4.3.6: A comparison between HRas G12V and KRas G12D three state diffusion model parameters. The diffusion parameters from vbSPT using trajectories acquired at 2 ng/mL Dox with minimum of 10,000 trajectories are summarized here. Although they both display a three-state model, there are significant difference between H and KRas (intermediate and fast state occupancies, and the transition probabilities between the two states).

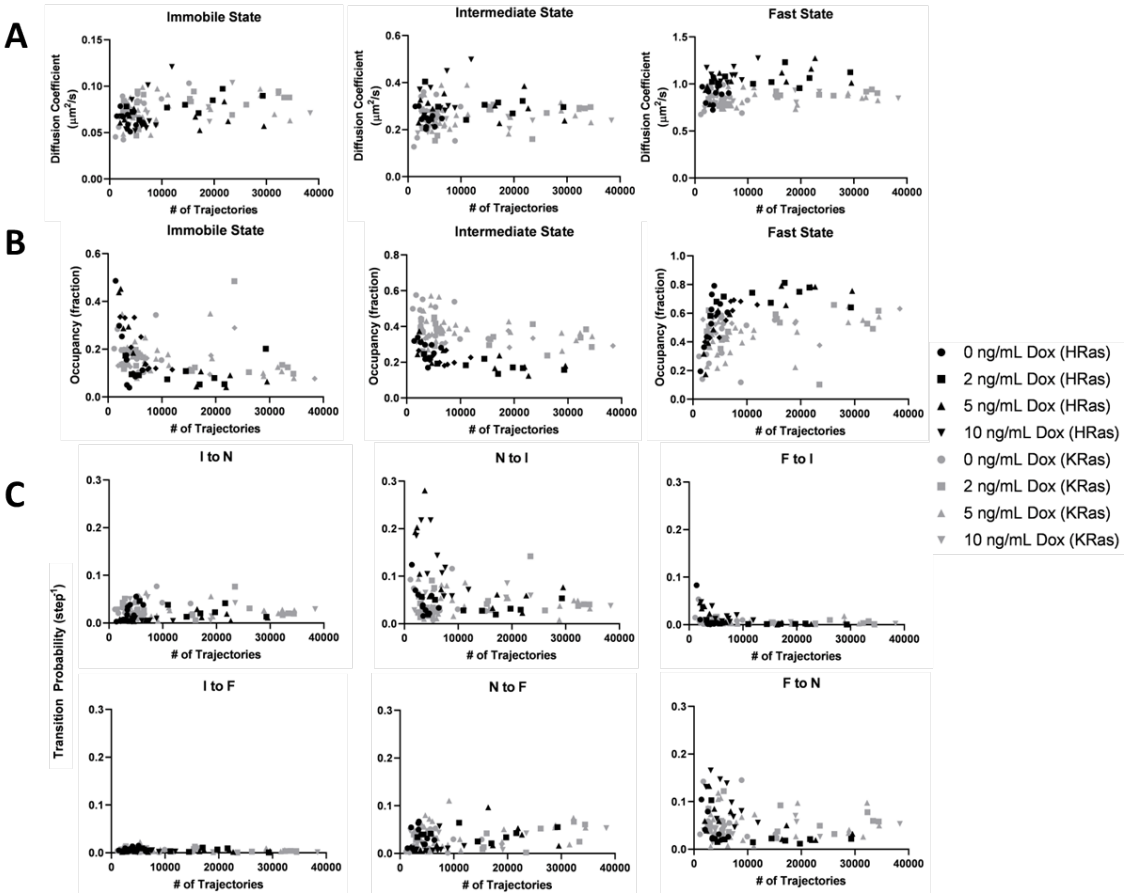

Figure 4.3.7: A full comparison between H and KRas diffusion parameters generated by vbSPT. The following diffusion model parameters are compared: (A) diffusion coefficients, (B) state occupancies, and (C) transition probabilities. The diffusion coefficients (A) show that HRas fast state is significantly faster than KRas, and the occupancies (B) show that HRas has a increased fast state and decreased intermediate fraction compared to KRas.

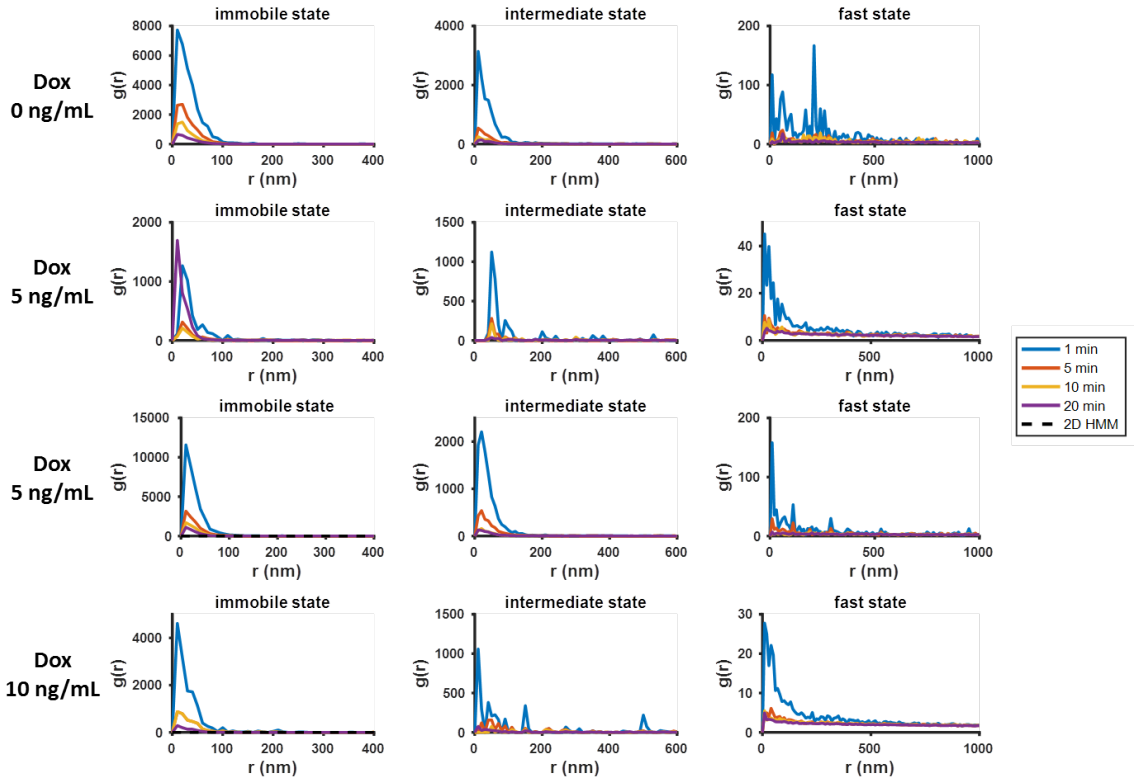

Figure 4.3.8: HRas immobile and intermediates are also correlated with membrane nanodomains. Pair correlation was calculated for HRas single particle tracking data similar to KRas. The results clearly show that the locations of the immobile and the intermediate states are clustered, indicating an underlying membrane region that is correlated to immobile and intermediate diffusion.

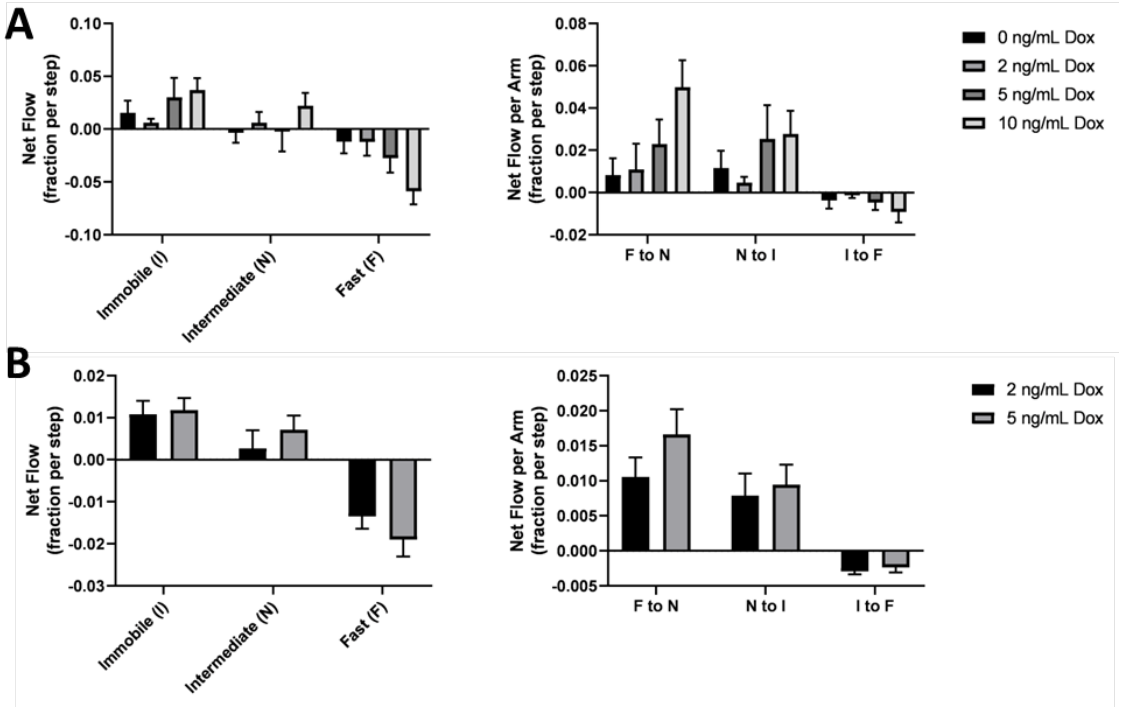

Figure 4.3.9: HRas also flows from the fast to the immobile state via the intermediate state. Similar to KRas results, HRas also is deposited on the membrane as the fast state and is removed from the membrane through the immobile state. Intermediate state has no net mass gain or loss. The 12 ms data is shown in (A) while 35 ms data is shown in (B).

4.3.3 Identification of Ras associated nanodomains (RANDs)

Using the algorithm described in the data analysis methods section, we identified membrane domains associated with the immobile and the intermediate Ras diffusion states. As figure 4.3.1 shows, the domain density increases with trajectory density for all cases, which is expected since domains can only be identified when Ras molecules are observed within them. Most notably, KRas has a significantly higher number of immobile domains than HRas while the density of intermediate domains is similar between the two isoforms (Figure 4.3.10).

Comparing the density of immobile and intermediate domains for each isoform, KRas on average has slightly higher number of immobile to intermediate domains, resulting in greater 1 ratio of immobile to intermediate domains, while HRas has on average fewer immobile domains than intermediate, resulting in less than 1 ratio (Figure 4.3.11). Figure 4.3.12 shows that the sizes of immobile and intermediate domains for both H and KRas are comparable.

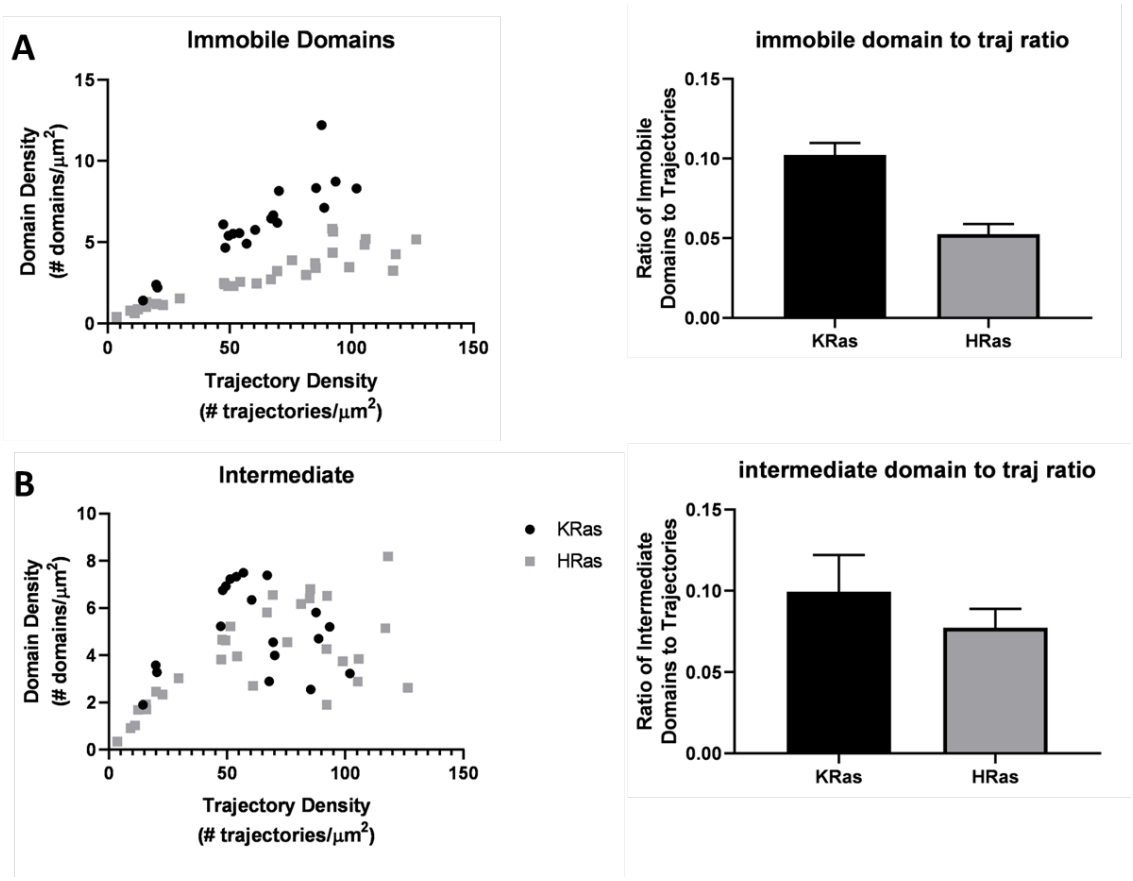

Figure 4.3.10: KRas has more immobile domains than HRas. A comparison between the isoforms for the immobile and intermediate domains is shown by plotting the domain density against the trajectory density (A) and the ratio of the domain density to trajectory density from (A) in (B).

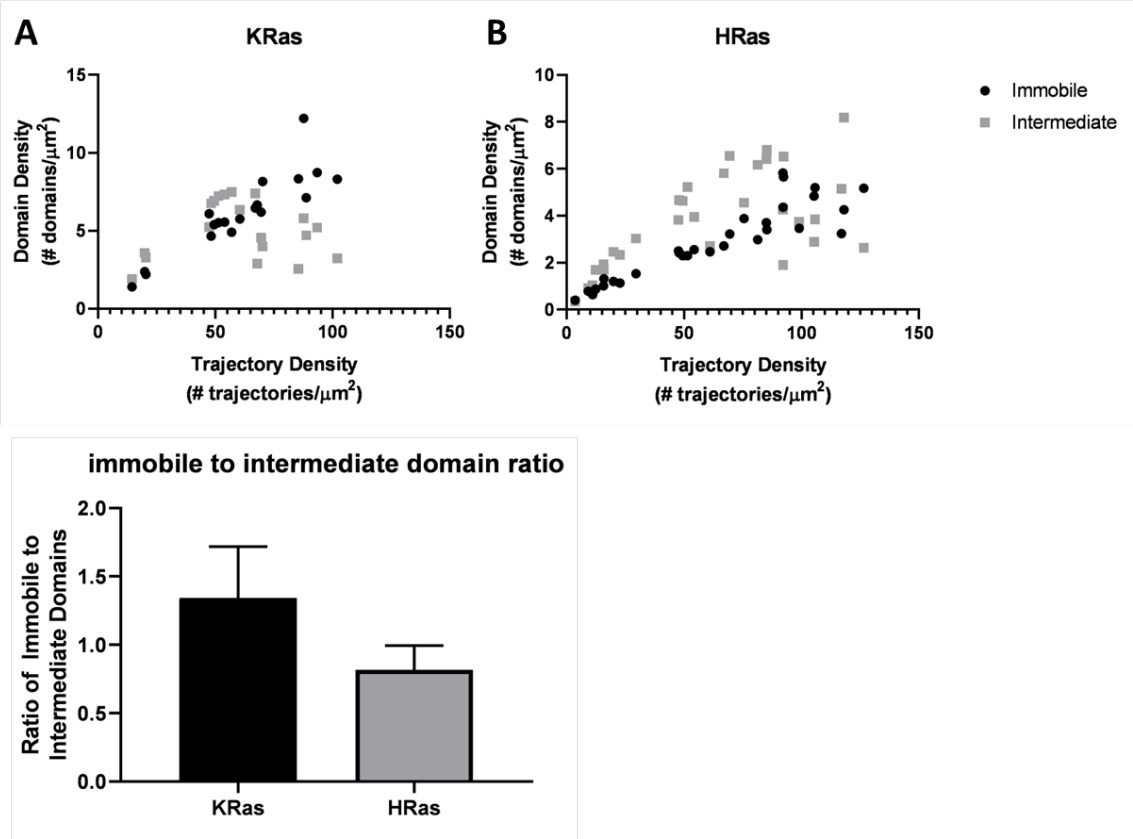

Figure 4.3.11: HRas has a lower ratio of immobile to intermediate domains than KRas. The same data from 4.3.10 is grouped for each isoform. This figure clearly shows that there are different trends for immobile vs intermediate domain densities for K (A) and HRas (B).

4.3.4 Life time analysis reveals multiple types of RANDs

Next we analyzed the life times for both immobile and intermediate domains. Life time was calculated by measuring the interval between the first and the last trajectory in that domain. Therefore, life time calculation and, by extension, the assessment of transient and stable domains are restricted to domains with a minimum of two or more trajectories.

Further investigation of the life times for immobile and intermediate domains

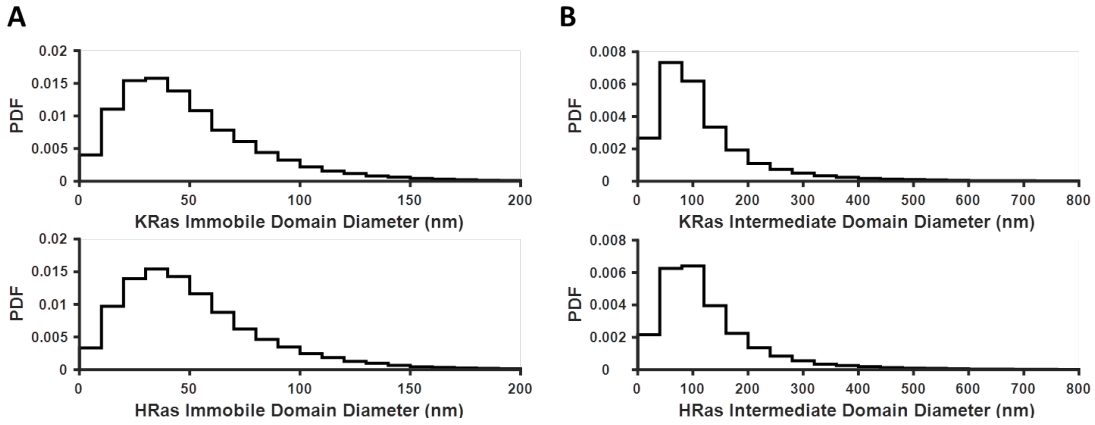

Figure 4.3.12: Histogram of H and KRas domain diameters. The distribution of immobile (A) and intermediate (B) domain diameters show that both isoforms interact with similar sized domains.

revealed that there are at least two different subtypes based on their duration: transient domains with life times on the order of seconds and stable domains that are still present even after minutes (Figure 4.3.13). Transient and stable domains were identified by fitting a two-component Gaussian mixture model to the distribution of the log transformed immobile domain life time (Figure 4.3.13), where the transient domains are the domains with the life time in the first peak. Given the absence of any transient intermediate population, the two component gaussian mixture model generated from the log transformed immobile life time histogram was used to determine whether an intermediate domain belonged to the transient or the stable population based on its log transformed life time.

Domain life times are the lower bound estimates since domains can only be identified when fluorescing Ras molecules travel into these regions. Therefore, the exact true life time is unknown. Further, due to the nature of the experiment and image processing, a single trajectory can be disconnected into two or more segments. Some of the factors that contribute to this challenge include blinking of PAmCherry1 or the failure to identify and fit a 2D gaussian to a particle due to a decrease in PAmCherry1 intensity or motion blur. Therefore, in the extreme case, it is possible that the transient domains are stable domains with a single trajectory that was artificially

misidentified as two separate events. In order to verify that the immobile transient domains were not artifacts of undersampled stable domains with a single trajectory broken into two, we ran simulations using the empirical distribution of the domain life time and the trajectory interval (Figure 4.3.14).

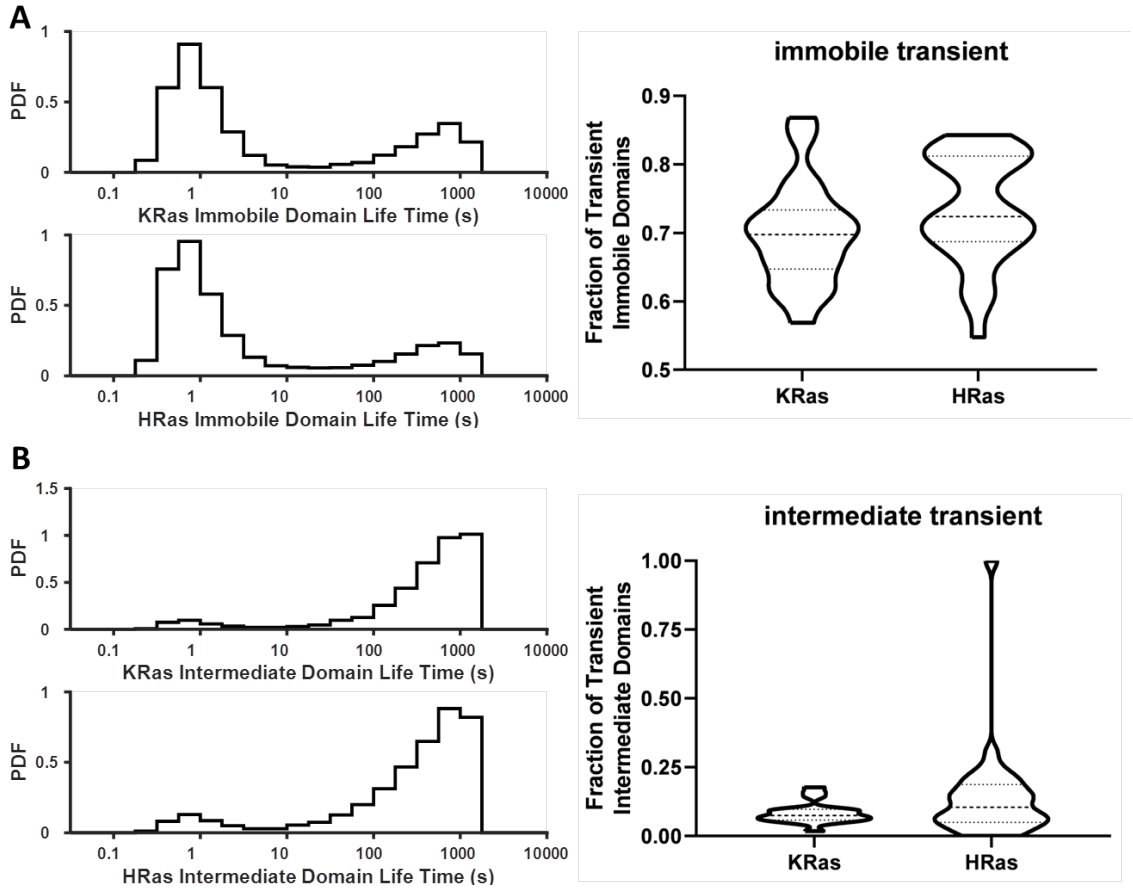

Figure 4.3.13: Both K and HRas have transient and stable domains. The histogram of log transformed domain life times for both immobile (A) and intermediate (B) domains show two peaks representing short lived domains with peak ∼1s and long lived domains with life times on the order of minutes.

Trajectory interval was calculated by measuring the time interval between domain trajectories for every domain with minimum of two trajectories. We assumed that the stable domains were real, defined as domains with life times >20 seconds

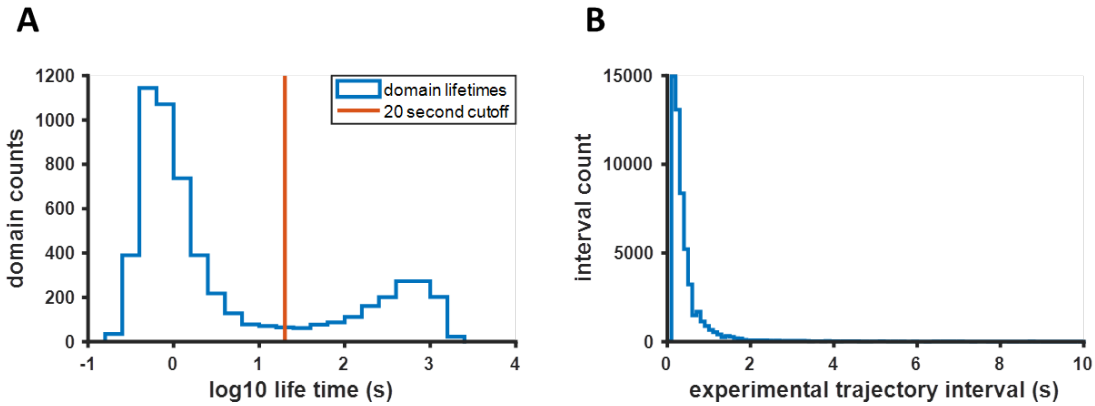

Figure 4.3.14: Empirical distribution of the log transformed domain life times (A) and trajectory intervals (B)

(2nd peak in the log transformed life time histogram), and ran simulations to determine whether the simulated fraction of stable domains that has been visited only once matched the experimental fraction of transient domains. Since we suspected that some of the shorter intervals in the experimental trajectory interval histogram could be cases of single trajectory misidentified as two trajectories, we truncated the experimental trajectory interval distribution at multiple values (0 - 10 s). At the start of the simulation, the domain life time was constructed by sampling with replacement from the experimental distribution of the domain life life time with minimum of 20 seconds (right of the red line in Figure 4.3.14), and a random number, drawn with replacement from the truncated experimental trajectory interval, was added to generate the true domain life time. The additional step of adding a random number from the truncated experimental trajectory interval was necessary since the experimentally acquired distribution of domain life time is underestimated, and that underestimation is dependent on the trajectory interval. For each domain, a random number was sampled from the truncated experimental trajectory interval to simulate the time that it took for a trajectory to visit the domain. The first time interval was halved, since the movie acquisition starts from a random point in time and not since the last visit, and trajectories were continually drawn until the total interval exceeded the true domain life time. The life time of any domain that only

had a single visit was mapped to 1 second, corresponding to the transient life time. The simulated life time was calculated using the same method as the experimentally acquired domain life time (last domain trajectory - first domain trajectory). The number of simulated domains are equal to the number of experimentally identified immobile domains so that the results can be compared side by side. As Figure 4.3.15 shows, simulations using just the stable domains could not replicate the observed fraction of transient domains even using the entire experimental trajectory interval distribution. Therefore, we determined that transient domains are in fact real and not artifacts of stable domains defined by single trajectories.

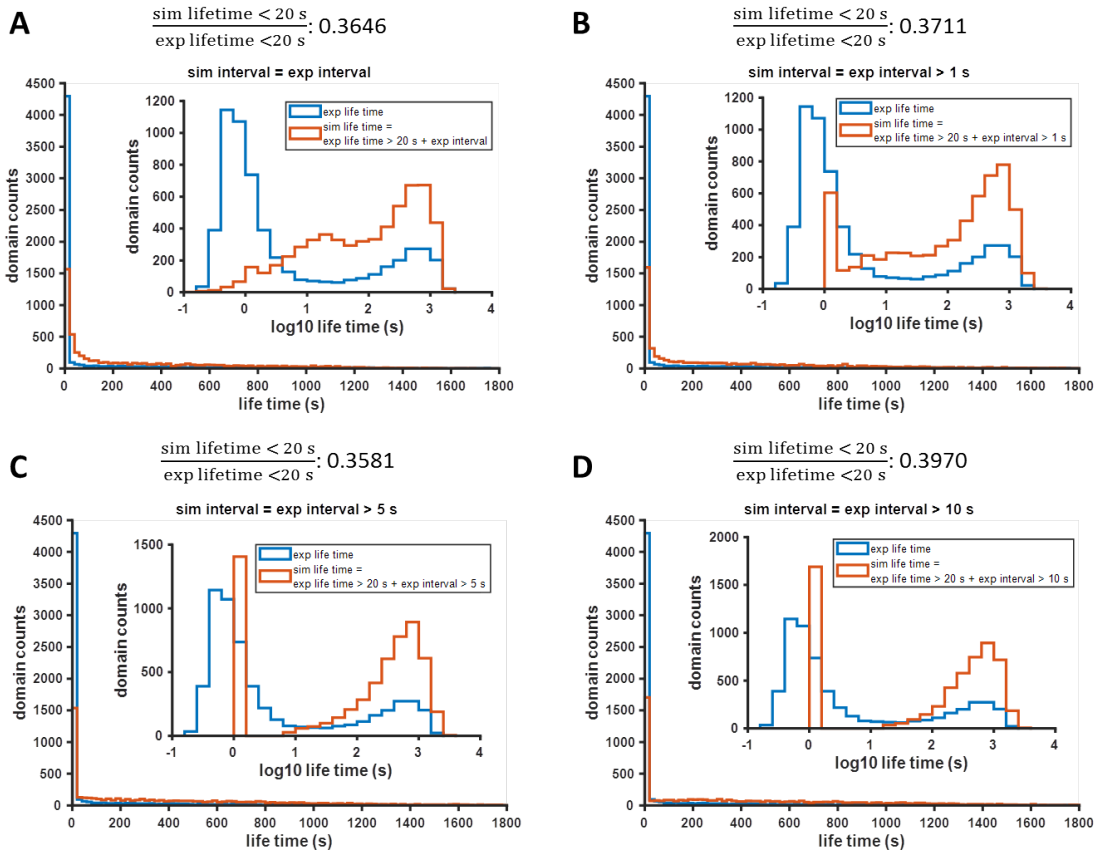

Figure 4.3.15: Validating the presence of transient domains with simulations. Simulated life time histogram only for stable domains at various trajectory interval (the full experimental trajectory interval distribution (A), experimental trajectory intervals greater than 1 s (B), 5 s (C), and 10 s (D)) is plotted against the experimental life time to show that stable domains cannot produce enough transient life times to account for the large fraction of immobile transient domains observed in experiments. The inset shows the same data as log transformed life time.

As Figure 4.3.13 shows, although the total range of the transient fraction is similar for both isoforms, KRas tends to have slightly lower fraction of transient domains for both immobile and intermediate domains. The size distributions of the transient and stable domains are similar between H and KRas (Figure 4.3.16). Although the stable domains tend to be slightly larger than the transient counterpart, this may be due to smearing of the positions over time. As expected, the number of trajectories per domain is higher for stable domains, most likely due to the fact that stable domains exist for significantly longer period than the transient domains (Figure 4.3.17).

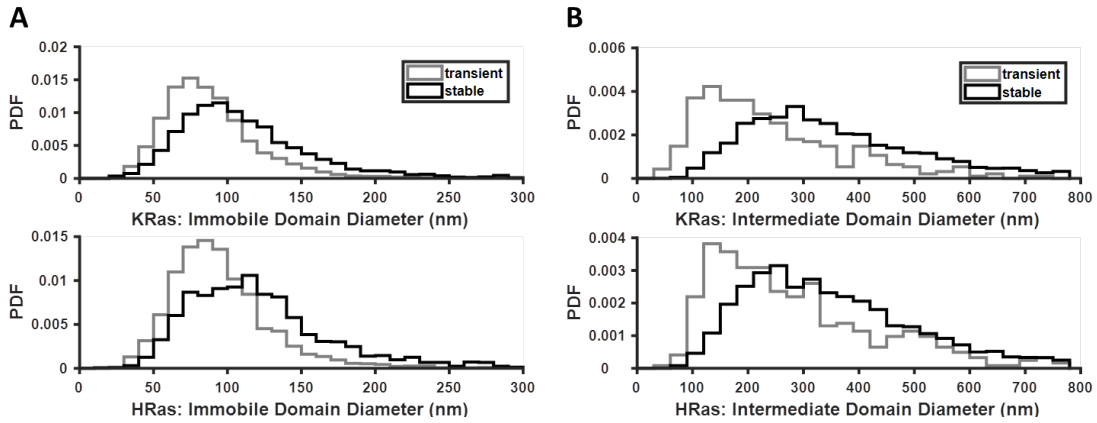

Figure 4.3.16: Distribution of the transient and the stable domain diameters for immobile (A) and intermediate (B) domains.

4.3.5 Visualizing H and KRas localizations to various RANDs using correlative microscopy

In order to directly image the membrane environments that Ras inhabits, we turned to correlated light and electron microscopy (CLEM) which can reveal cellular ultrastructures and the positions of the individual Ras proteins tagged with PAm-Cherry1, based on EM and super-resolution imaging respectively. Since Ras resides in the inner membrane, cells were grown on coverslips and the apical membrane was ripped off and imaged [103]. The CLEM images were acquired by Dr. Ying Zhang and the CLEM figures are taken from our joint paper [103].

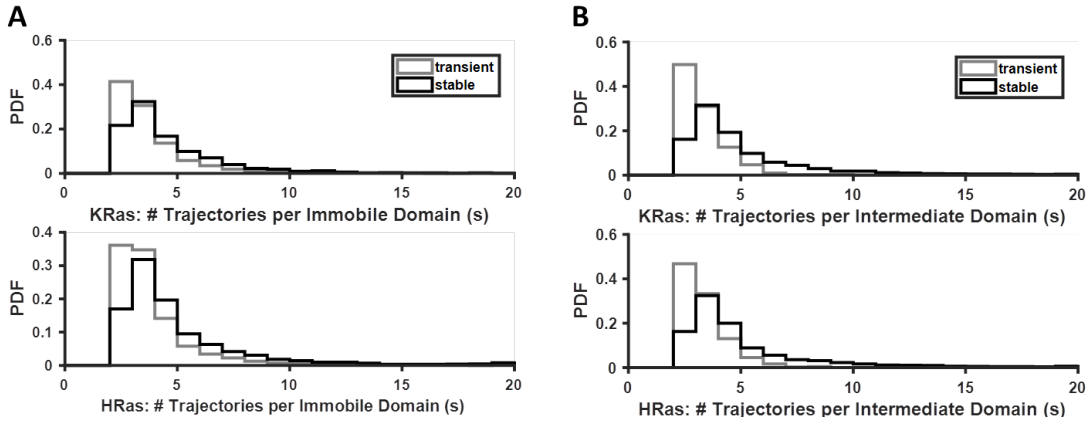

Figure 4.3.17: Distribution of the number of trajectories for the transient and the stable domains for immobile (A) and intermediate (B) domains.

Through the use of CLEM, we observed two main membrane structures, filaments and vesicles, and determined that there are differences in the preference for those structures between H and KRas (Figure 4.3.18). Vesicles are heavily stained structures about 50-200 nm in diameter while filaments were lightly stained. Membrane features were defined as filament or vesicle based on intensity thresholding and dilation to further improve the segmentation (Figure 4.3.18). Once filaments and vesicles were segmented, Ras molecules were categorized as either filament or vesicle associated if they were within 20 nm to either one of the structures (Figure 4.3.18). Therefore, some Ras molecules were not assigned to either compartment if they were further than 20 nm from both structures and those that were within the threshold to both compartments were added to both filaments and vesicles.

The KRas molecules showed above random localization to filaments while more HRas molecules were found in vesicles than random distribution (Figures 4.3.19 & 4.3.20). Further, this partitioning was similar for just the C-terminal membrane targeting motif of each isoform, demonstrating that the tail is the main source of the dissimilar compartmentalization between H and KRas.

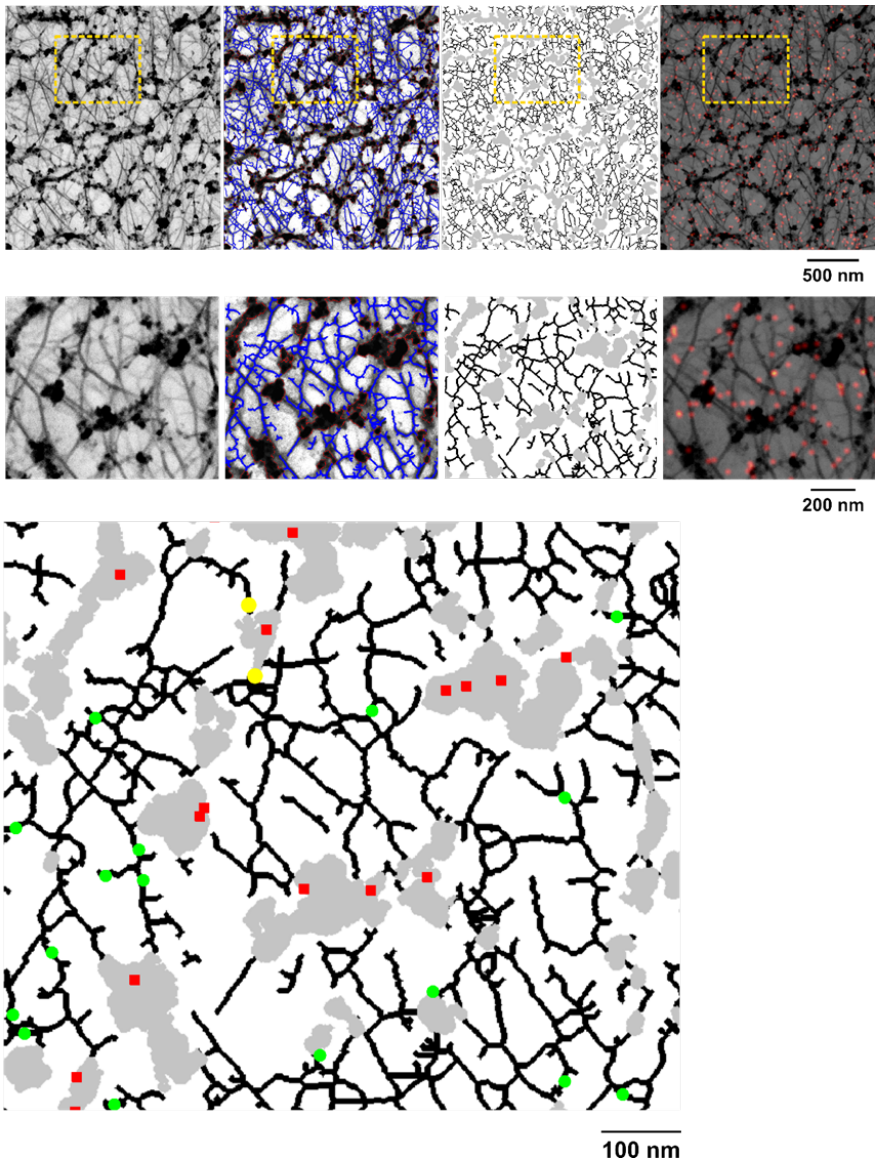

Figure 4.3.18: CLEM images show actin and vesicles along with KRas locations. Segmentations of scanning electron microscopy images show actin in black and vesicles in gray. Red, green, and yellow dots represent Ras molecules within 20 nm distance to membrane filaments, vesicles, or two both features. Reprinted from [103].

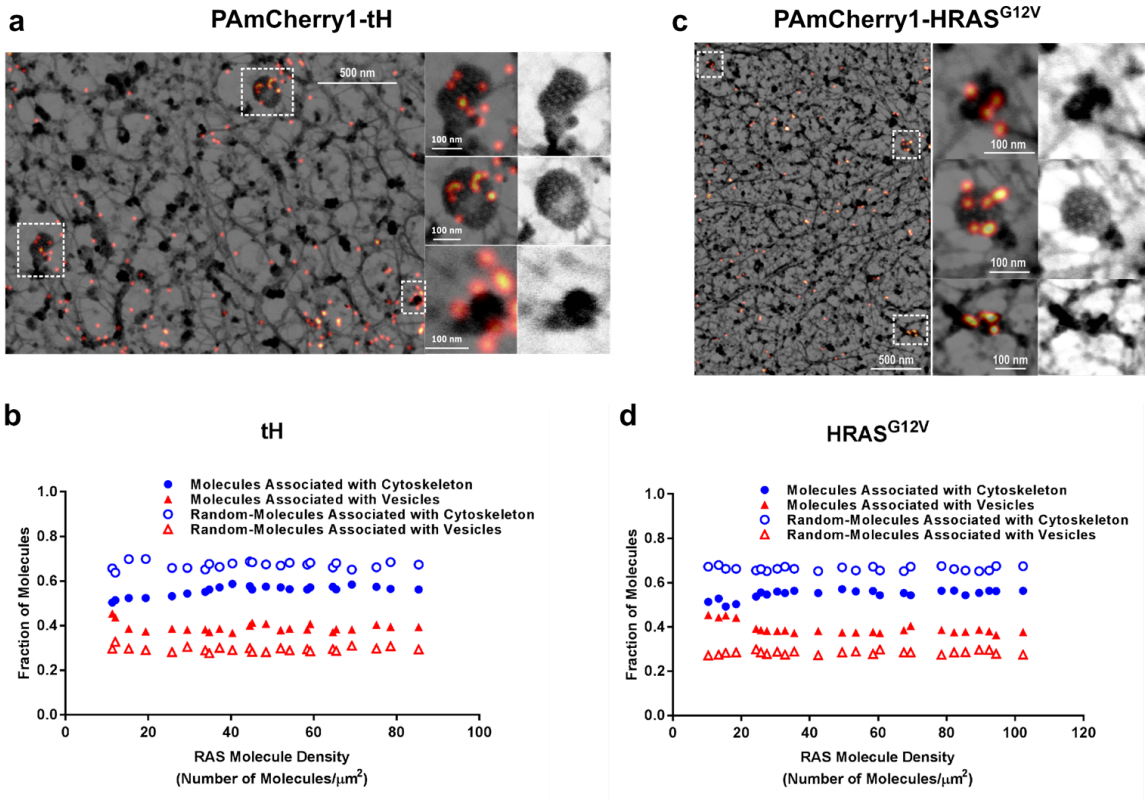

Figure 4.3.19: Preferential localization of tH and HRASG12V to membrane vesicles and CCPs. (a) Correlative SRM and SEM images showed strong preference of tH localization of membrane vesicles and CCPs. (b) Quantitative analysis of proximity of tH to membrane vesicles and filament network at tH densities from ∼10 to ∼90 molecules/μm^2. (c) Correlative SRM and SEM imaging of HRASG12V showed its high localization preference to membrane vesicles and CCPs. (d) Quantitative analysis of proximity of HRASG12V to membrane vesicles and filament network at HRASG12V densities ranging from ∼10 to ∼100 molecules/μm^2. Reprinted from [103].

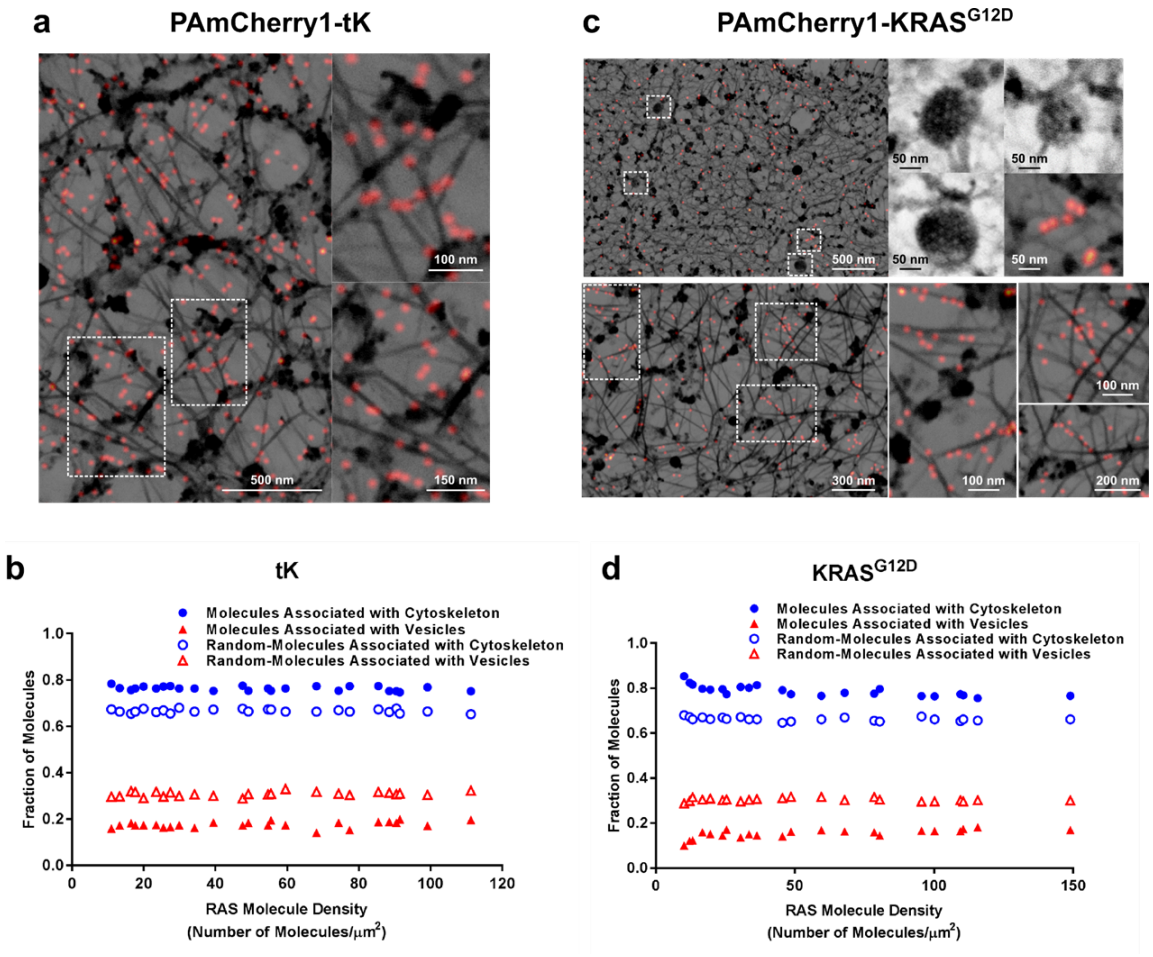

Figure 4.3.20: Preferential localization of tK and KRASG12D to the vicinity of cortical cytoskeleton. (a) Correlative SRM and SEM images showed tK localizing to vicinity of cortical actin network; (b) Quantitative analysis of the spatial proximity between tK and the membrane vesicles or the cortical filaments, at expression levels from $\sim$10 to $\sim$110 molecules/μm^2; (c) Correlative SRM and SEM imaging of KRASG12D showed its localization is excluded from vesicles and CCPs. Instead, localization of KRASG12D showed high preference to filamentous network. (d) Quantitative analysis of proximity of KRASG12D to membrane vesicles and filament network at molecule densities ranging from $\sim$10 to $\sim$150 molecules/μm^2. Reprinted from [103].

Interestingly, for both isoforms, dimers were mostly associated with filaments while larger multimers were found predominantly in vesicles (Figure 4.3.21). However, KRas tended to form dimers while HRas formed larger multimers [103]. In conjunction with higher affinity to filaments for KRas and HRas localization to vesicles, this implies that the membrane compartments dictate the size of multimers and it is the isoform affinities to the compartments that generate the different distribution of cluster sizes. Consistent with the isoform dependent cluster formation hypothesis, K and HRas differed in cluster density in addition to the size of the clusters. Cluster density, defined as the number of Ras multimers (two or more Ras molecules) per area, showed clear deviation between the isoforms as a function of Ras expression (Figure 4.3.22). KRas cluster density linearly increased with Ras expression while HRas cluster density reached a plateau around 60 molecules/μm^2. Thus, these observations support the hypothesis for minimum of two independent mechanisms for Ras multimer formation.

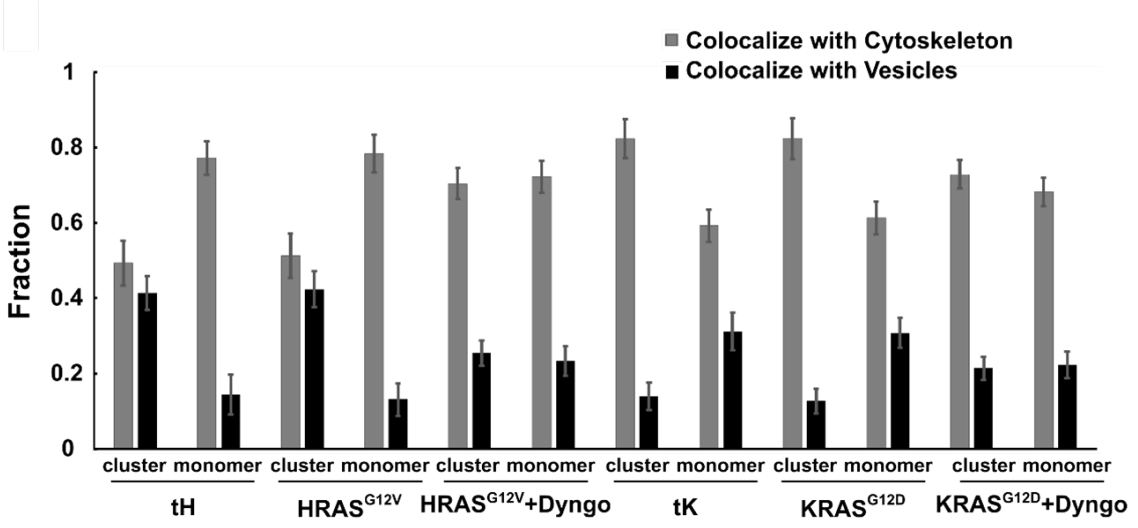

Figure 4.3.21: Ras dimers preferentially localize to the cytoskeleton while larger multimers (3 or more Ras molecules) colocalize with the vesicles. Dynamin inhibition with dyngo treatment results in partial reversal of the isoform specific association with actin and vesicles. Reprinted from [103].

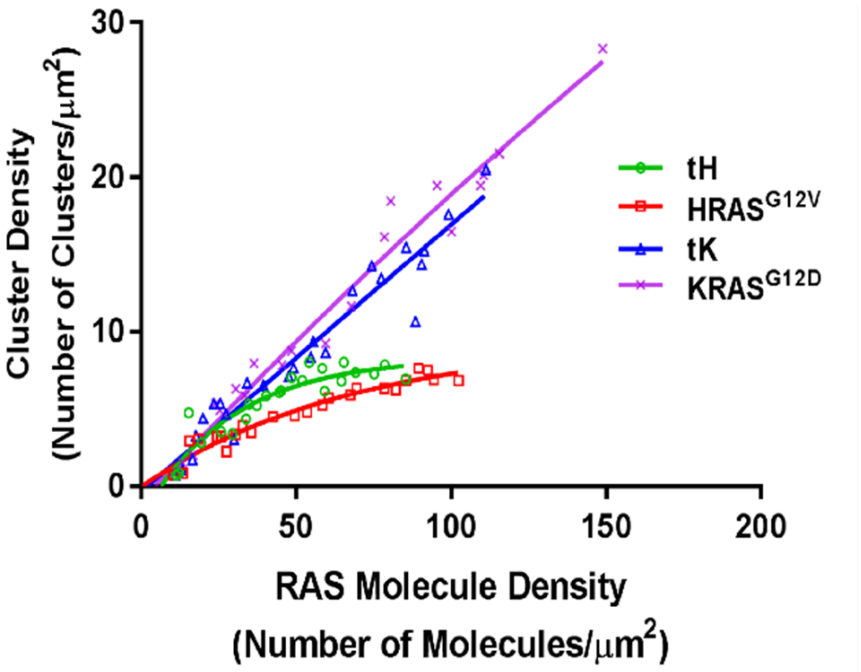

Figure 4.3.22: The density of KRas clusters increases linearly with Ras density while HRas reaches a limit around 60 molecules/μm^2. Reprinted from [103].

4.3.6 Perturbation studies suggest potential identities of RANDs associated with H and KRas

Thus far we have shown the importance of the two membrane structures in H and KRas segregation. We perturbed the membrane by eliminating membrane vesicles through Dyngo 4a, a dynamin inhibitor that prevents the membrane fission required for endocytosis. Dyngo treatment resulted in the accumulation of both H and KRas at the membrane and significantly reduced the number of vesicles at the cell membrane [103]. In addition, it also resulted in the random distribution of both isoforms, resulting in decreased localization of HRas and KRas to vesicle and filament respectively (Figure 4.3.21). However, the impact on the Raf-MAPK signaling was opposite for the two isoforms. HRas showed reduced ppERK signaling after dynamin inhibition while KRas showed increased signaling.

Given that dyngo treatment in the CLEM work resulted in reversal of isoform

specific preference (Figure 4.3.21), we examined the effect of dyngo treatment on the RANDs. To our surprise, dyngo treatment resulted in significant differences between K and HRas diffusion on the membrane. Dynamin inhibition with dyngo resulted in almost complete immobilization of KRas molecules while HRas still retained a 3 state model, albeit at slower diffusion coefficients for the two mobile states (Figure 4.3.23).

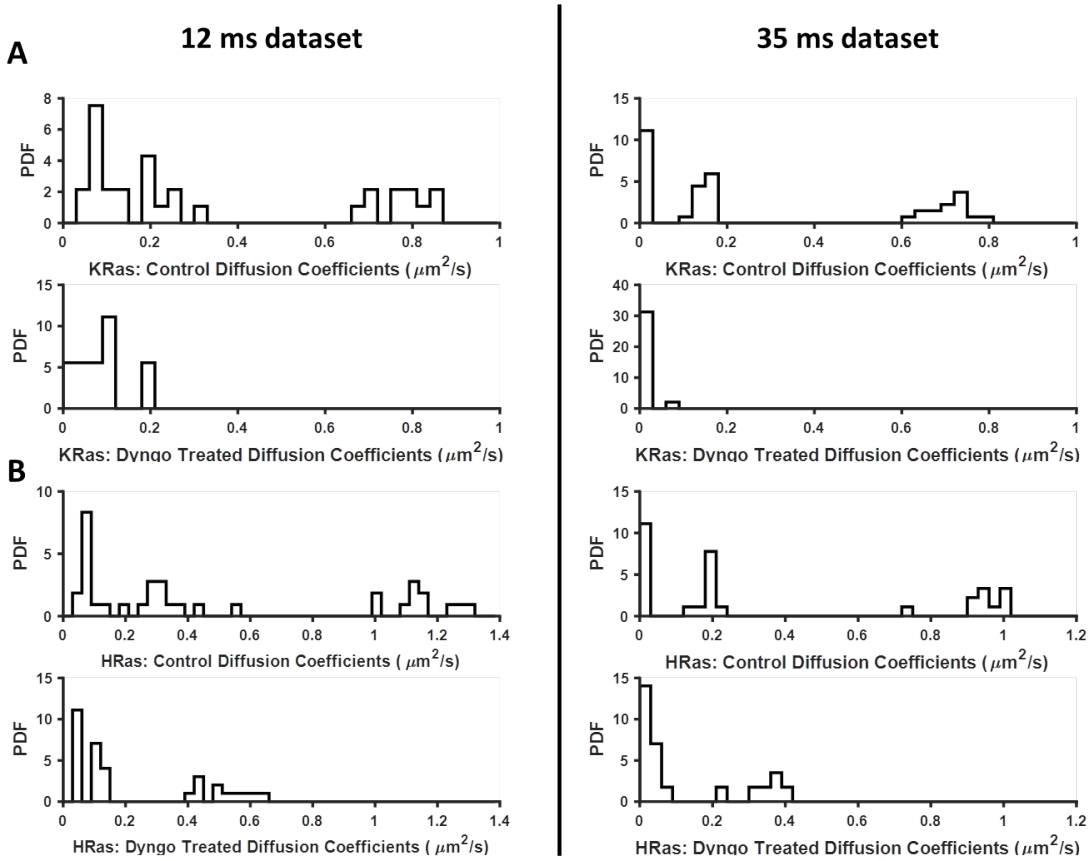

Figure 4.3.23: Impact of dynamin inhibition on K and HRas lateral diffusion. KRas (A) molecules became immobilized upon dynamin inhibition while HRas (B) still retained mobility albeit decreased diffusion after Dyngo 4a treatment.

4.4 Discussions/Conclusions

In this chapter, we extended the study of KRas G12D (GTP bound state) lateral diffusion from the previous chapter to KRas WT (GDP bound state) and HRas, and characterized the Ras associated membrane domains. These domains were observed to capture multiple Ras over the duration of their life times. To this end, we developed a clustering algorithm to identify and characterize the immobile and the intermediate domains. Domain analysis allowed us to estimate the minimum duration of these domains (life time), their abundance, and their size.

Interestingly, KRas G12D, KRas WT, and HRas all displayed a three state diffusion model on the membrane with the same nested domain structure and trafficking through the domains. Further, KRas lateral diffusion did not appear to be effected by the nucleotide bound state; the diffusion model between KRas G12D and KRas WT did not appear to be significantly different. However, it is difficult to make any conclusions given that there is insufficient data for KRas WT with high trajectory density. In contrast, there were significant isoform differences. In addition to displaying a faster diffusion coefficient for the fast state, GTP bound HRas also had significantly higher fraction of its population in the fast state and less in the intermediate state compared to GTP bound KRas. Since HRas has the most divergent tail from KRas, this is in line with the hypothesis that the Ras tail is the primary driver of Ras membrane behavior.

Based on live cell single particle experiments, the distribution of the Ras associated membrane domains showed two general classes of domains based on their life time; transient and stable. Concurrently, CLEM work has revealed that there are two broad categories of membrane structures, actin filaments and membrane vesicles, with differential affinities for H and KRas. We hypothesize that the transient and stable immobile domains identified from live cell single particle tracking are in fact associated with the cytoskeleton and membrane vesicles observed in EM images. Further, we hypothesized that the membrane compartments (actin and vesicles) generate Ras clusters and that isoform specific affinity to one of those compartments results in the observed differences in Ras multimer size.

The most striking difference between the Ras isoforms was in the abundance of the immobile and intermediate domains. KRas had significantly more immobile domains than HRas while the intermediate domain density are similar between the two isoforms. This finding is corroborated by CLEM, where live cell SPT and CLEM showed remarkable similarity in cluster density and immobile domain density as a function of Ras expression. Both imaging methods showed that KRas cluster density (CLEM) and immobile density (live cell SPT) grew linearly while HRas reached a limit. The density of immobile domains and clusters for HRas plateaus around 100 trajectories/μm^2 while KRas immobile and cluster densities increase with Ras density. This implies that immobile domains are involved in cluster formation for both isoforms. This hypothesis is further validated by the CLEM finding that the size of the clusters are compartment dependent. Regardless of the isoform, dimers were associated with actin while larger clusters tended to be found in membrane vesicles. The differential affinities for actin and membrane vesicles resulted in higher dimer fraction for KRas and larger clusters for HRas. Thus, evidence suggests immobile domains are correlated with cluster formation, and the type of immobile domain dictates the size of the cluster.

The unequal ratio of the number of immobile to intermediate domains implies distinct membrane organization between the isoforms. The ratio of the immobile to intermediate domain density was slightly greater than one for KRas and less than one for HRas. This indicates that there is not a one to one relationship between immobile and intermediate domains. Some HRas intermediate domains have no immobile domains within them while some KRas have more than one immobile domain for a given intermediate domain. Coupled with the fact that that virtually all intermediate domains are stable for both isoforms, this implies that stable intermediate domains contain multiple KRas immobile domains while some intermediate HRas domains lack immobile domains.

The size of the domains and the life time histograms are similar for both isoforms. This suggests that both H and KRas sample the membrane equally, if we assume that both molecules are under Brownian motion. However, the difference in their affinity for the two membrane structures implies that KRas spends more time with

actin filaments while HRas spends more time in vesicles.

A potential confounding variable for the observed isoform differences could be due to the differences in the cell line and not the Ras isoforms themselves. Although we tried to address this issue by using the same parental U2OS-tetR cell line, genetic drift results in divergence between the same cell line as they are independently passaged. A potential experiment to mitigate this factor would be to simultaneously image both isoforms in the same cell. This would ensure that the observed differences were due to the isoforms themselves and not due to the cell line.

Dynamin inhibition with Dyngo 4a resulted in the elimination of the membrane vesicles and in the accumulation of Ras at the membrane. We determined in the previous chapter that Ras is removed from the membrane through the immobile domain. Thus, the accumulation of membrane Ras by the loss of endocytic vesicles supports the idea that at least a subset of the immobile domains are endocytic vesicles. The link between membrane vesicles as the potential identity of the stable immobile domain comes from work by Gaidarove et al. Gaidarov et al showed that clathrin coated pits form at defined sites on the membrane [104]. Consistent with our measurement of stable domain life time, they found that clathrin coated pits will reappear in the same location over 9 minutes of observation. Together with CLEM static images, it seems that actin and membrane vesicles may represent the underlying structures involved in transient and stable immobile domains. However, this does not exclude the possibility that the transient immobile domain may also be composed of clathrin coated pits that did not reform in the same location at a later time.

Dyngo 4a treatment decreased the isoform specific localization to the cytoskeleton and membrane vesicles but had remarkably different effects on the diffusion model. KRas was virtually immobilized while HRas still retained a 3 state model, albeit with slower states. Naively, one might think that KRas immobilization upon dynamin inhibition might be due to the blocking of endocytic vesicles and the accumulation of KRas molecules inside of the membrane vesicles. However, it is difficult to attribute this change in the diffusion model solely to the elimination of the membrane vesicles. Dyngo 4a is known to have multiple off target effects such as inhibition of membrane

ruffling, destabilization of F-actin, as well as depletion of cholesterol from the plasma membrane [105, 106]. In addition, there is no reason to assume that the Dyngo 4a treated HRas states are the same states as the untreated HRas. Since the diffusion coefficients are different, that would indicate that the membrane environment has changed. This would imply that the Dyngo 4a treated diffusion model is not directly comparable to the untreated cells.

Chapter 5

Potential roles of membrane nanodomains in Ras multimer formation and signaling

5.1 Introduction

In the previous chapter, we characterized the Ras associated nanodomains (RANDs) that organize membrane Ras. However, their function and role in Ras signaling is yet unknown. While the importance of Ras dimers and clusters in signaling is documented in the literature, the mechanism for Ras cluster formation on the membrane remain obscure. Here we present some preliminary work in determining the role of RANDs in Ras clustering and signaling.

The hypothesis to be tested was whether RANDs facilitate dimer formation. Since Ras clusters have been shown to be necessary for downstream signaling, if RANDs are necessary to generate the number of Ras dimers observed in experiments, it would indicate that RANDs have a direct role in Ras signaling. To understand the role of RANDs in Ras cluster formation, two different membrane simulations were created to compare the formation of Ras clusters: 1) a free membrane model with a freely diffusing, homogeneous Ras population with a single speed, and 2) an

anchored membrane model to reflect experimental findings of a heterogeneous Ras population with two different speeds, free and trapped. The simulation was run until the membrane system reached an equilibrium and the fraction of various cluster sizes were compared to determine the impact of RANDs in Ras cluster formation.

In order to determine the role of RANDs in Ras signaling, we simultaneously imaged KRas G12D and CRaf WT to verify that Raf also had RANDs. Since Raf is the downstream effector of KRas G12D, if RANDs are involved in Ras signaling, it implies that Raf must also interact with RANDs.

5.2 Experimental, data analysis, and simulation methods

5.2.1 Membrane Simulations

We compared the equilibrium Ras cluster fraction between two simulations that assume different cell membrane environments (Figure 5.2.1). The free diffusion model assumes that the membrane is homogeneous and all of the Ras proteins freely diffuse on the membrane, resulting in a single speed with a normal distribution. The anchor model takes membrane heterogeneity into account. Instead of allowing all of the Ras molecules to freely diffuse in the membrane, there are regions on the membrane that trap Ras for a given period. Trapped Ras molecules have reduced diffusion and are only allowed to move within the anchor while they are trapped. Thus, the anchor model separates the Ras molecules into two populations with different speeds: freely diffusing Ras and trapped Ras. The anchored model represents a simplified scenario where the Ras molecules were separated into two diffusion states instead of three.

The following inputs are necessary for both models: the size of the membrane, Ras membrane density, diffusion rate, Ras radius, and Ras cluster life time (how long a Ras stays with another Ras). The anchor model requires additional parameters, such as the size and the concentration of the anchors, as well as the duration of the Ras-anchor interaction.

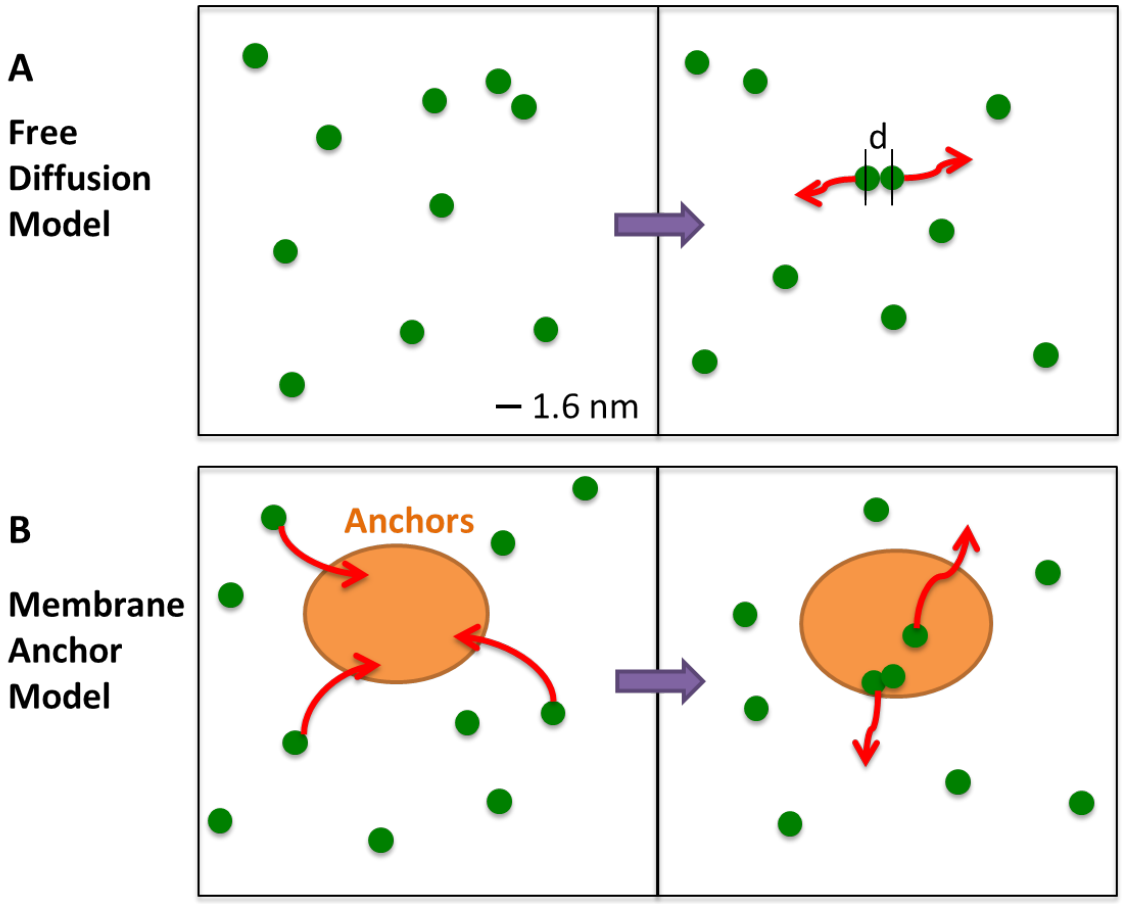

Figure 5.2.1: A diagram of the membrane simulation. The green dots, representing Ras molecules, diffuse and form clusters when two molecules are within 1.6 nm. In the membrane anchor model (B), anchors (80 nm orange circles) are randomly placed on the membrane that temporarily trap green Ras molecules. In the free diffusion model (A), there are no mechanisms that facilitate Ras cluster formation.

5.2.2 Two Color Single Particle Tracking

In order to concurrently track KRas G12D and CRaf WT in the same cell, we used the U2OS cell line stably expressing doxycycline inducible PAmCherry1-KRas G12D (described previously) and transiently transfect CRaf WT tagged with PA GFP. This allowed us to acquire two color sptPALM using both colors, PAmCherry1 and PA GFP, to observe Ras and Raf at the same time.

5.2.3 RAND Detection Method

We developed an analysis method for single particle trajectories to systematically identify and characterize RANDs with low false positive rates (Figure 5.2.2). The accuracy of this anchor detection algorithm was validated on simulated dataset. Since anchors are defined as regions that trap Ras and restrict its mobility, anchors were identified by filtering for trajectory that displayed restricted mobility, defined as moving less than 100 nm for minimum of 3 points. We used the following method to locate RANDs for analysis (Figure 5.2.2 A): 1. screen for trajectories with at least 3 positions less than 100 nm displacement from one of the positions in the trajectory, 2. apply Density - Based Spatial Clustering of Applications with Noise (DBSCAN), a well-established clustering algorithm, to determine the RAND position and radius, and 3. apply a Poisson threshold to determine that the amount of time spent inside of the RAND is higher than expected from complete spatial randomness. We validated the detection method by running Matlab simulations of freely diffusing particles (with experimental derived diffusion parameters from the live cell single particle tracking experiments) that were transiently trapped in randomly placed circular regions with 50 nm radius (Figure 5.2.2 B). In order to replicate the experiment as closely as possible, the simulated trajectory length was kept the same as the experimental trajectory length. The RAND detection method was applied to the simulated trajectories to measure the detection efficiency of the hidden anchors. Since this was a simulation, the total number of the hidden anchors were known, and the detection efficiency using only the simulated trajectories could be calculated. The efficiency of the detection method depended on two factors, the trajectory density and

the RAND density. RANDs are only detected when two events happen concurrently: RAND must trap a Ras with a fluorophore in the on state. The red lines indicate trajectories with anchors that were observed and dotted blue circles indicate anchors that were never detected because trajectories did not happen to fall into them (Figure 5.2.2 B). Consequently, RAND detection efficiency increases with trajectory density (Figure 5.2.2 C). The detection method successfully detected most RANDs at high trajectory densities. Importantly, regardless of the condition, the false positive rate was extremely low for all cases (Figure 5.2.2 D). While only a fraction of anchors can be detected, the true number of anchors can be estimated since the Ras trajectory density is known.

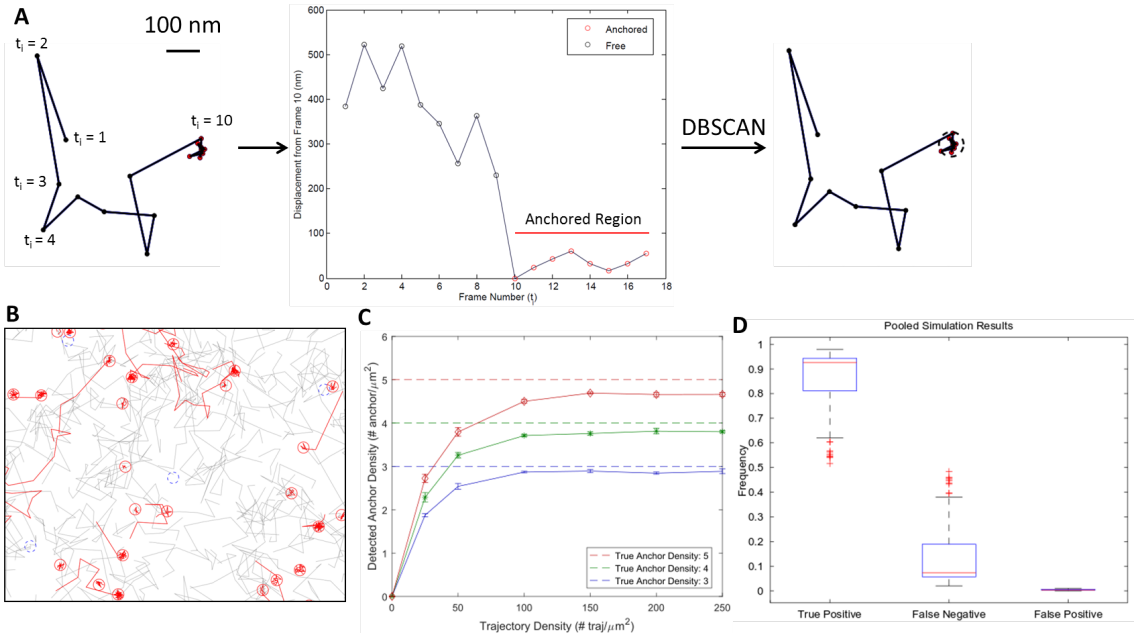

Figure 5.2.2: Anchor detection using trajectories with limited mobility. For every trajectory with a minimum length of 5, the displacement from each coordinate in the trajectory is calculated (A). If there are at least 3 points less than 100 nm from any other point in the region, the trajectory is determined to be anchored (A). All spatially overlapping anchored trajectories are grouped and DBSCAN is used to finalize the anchors (A). We validated our anchor detection method with simulations of freely diffusing particles that were temporarily trapped by hidden circular regions (B). The red lines indicate detected anchors and the corresponding simulated trajectories that defined them, while dotted blue circles indicate anchors that were never observed (B). Since anchors are only indirectly observed when a trajectory is trapped within them, the detect efficiency increases and reaches a limit with increasing trajectory density (C). Although our detection efficiency relied on the density of the trajectories, the parameters that we used in our anchor detection method always had a very low false positive rate (D).

5.3 Results

5.3.1 RANDs in Ras multimer formation

Simulations suggest that cluster formation is enhanced with anchors, compared to the free membrane model. The free membrane simulation was run with the following parameters: cell membrane size (10 μm by 10 μm), Ras membrane density (50 Ras molecules/μm^2, diffusion rate (4000 nm/s), Ras radius (0.8 nm) and cluster life time (1 s). In addition to the basic membrane parameters, the anchor membrane model had 5 anchors/μm^2 with 80 nm anchor diameter, and a range of Ras-anchor life times from 1 to 10 seconds 5.2.1. As Figure 5.3.1 shows, free membrane generated virtually no clusters, with the membrane anchor model generating up to ∼12% Ras dimers, depending on the parameters. As expected, the generation of nanoclusters depends on multiple parameters, such as the number of anchors and the Ras-Ras life time. Some membrane anchor model parameters enhanced dimer formation while others generated more nanoclusters. Interestingly, Figure 5.3.2 shows that in some cases, there is an optimal concentration of anchors to maximize the fraction of clustered Ras. This is due to the fact that if there are too many anchors, each anchor only captures a single Ras, preventing cluster formation. However, these simulation results are based on simulation parameters that were unknown at the time, such as the Ras cluster duration, the size and the density of the anchors, and the membrane anchor model represents a simplistic two-state model even though in reality the membrane Ras behavior is a three-state model with two nested domains (Chapter 3). Hence, the findings here should be viewed with reservation.

5.3.2 RANDs in Ras signaling to Raf

We analyzed the two color live cell single particle tracking of KRas mutant and CRaf WT to determine if Raf was also recruited to RANDs. A map of the two color tracking shows that not only do CRaf anchors exist, but that a subset of the Raf and Ras anchors overlap (Figure 5.3.3). However, based on this data alone, one cannot distinguish whether CRaf was recruited to Ras at the anchors or if Raf diffusion

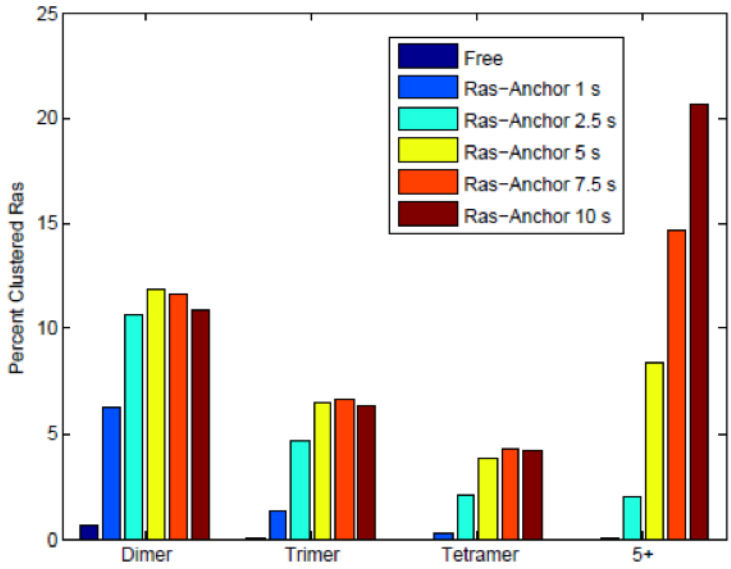

Figure 5.3.1: Simulation suggests that anchors facilitate dimer and cluster formation. For the given simulation parameters, experimentally observed dimer and cluster fraction was only achieved with the membrane anchor model. The free diffusion model resulted in almost no dimer or cluster formation.

is just mirroring Ras diffusion. Figure 5.3.4 shows that CRaf anchor domains are very similar to KRas mutant anchors, in terms of size distribution, density, life time, and mobility, except that CRaf anchor population is heavily skewed to the transient anchor population. The fraction of stable anchors is significantly reduced for CRaf. Interestingly, Raf has more anchors with multiple Raf visits.

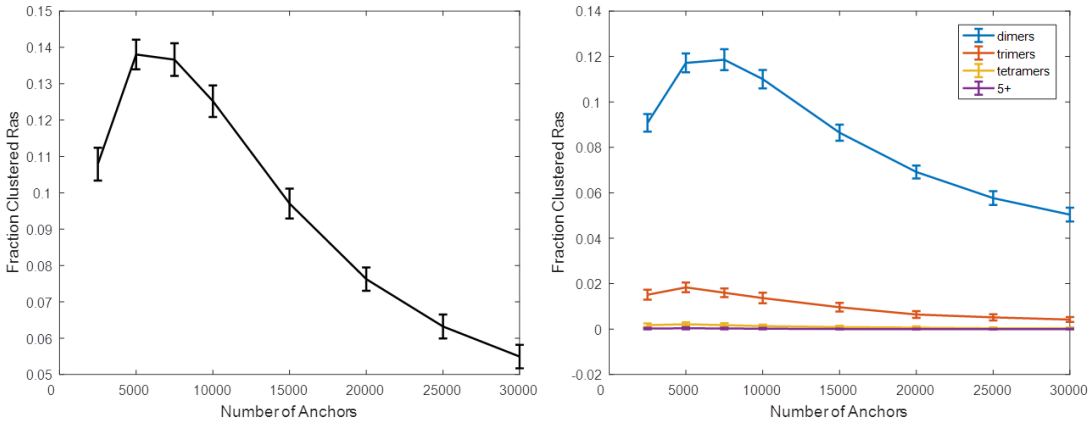

Figure 5.3.2: There is an optimum anchor density for maximum dimer and cluster formation. Contrary to the naive assumption, the relationship between Ras cluster fraction and anchor density is not linear. The Ras cluster formation peaks and decreases with increasing anchor density. This suggests that there is an anchor density that produces the maximum Ras clusters. The simulation used the following parameters: 10 μ m by 10 μm membrane, 20 nm anchor diameter, 100 Ras/μm^2, Ras-Ras life time of 1 s, and Ras-anchor life time of 10 s.

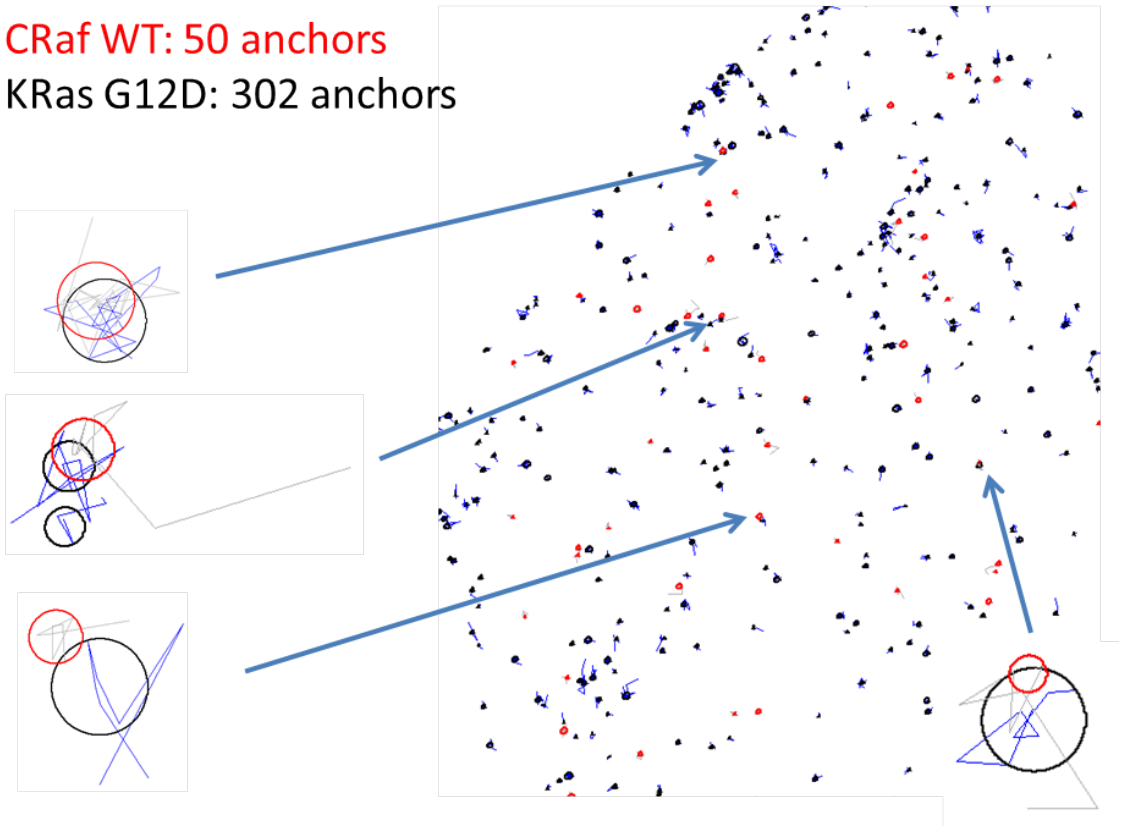

Figure 5.3.3: Ras and Raf anchors overlap. An example two color live cell tracking with PAmCherry1 tagged KRas G12D and PA GFP tagged CRaf WT shows that Raf also have anchors. In this particular cell, 50 CRaf anchors and 302 KRas G12D anchors were identified.

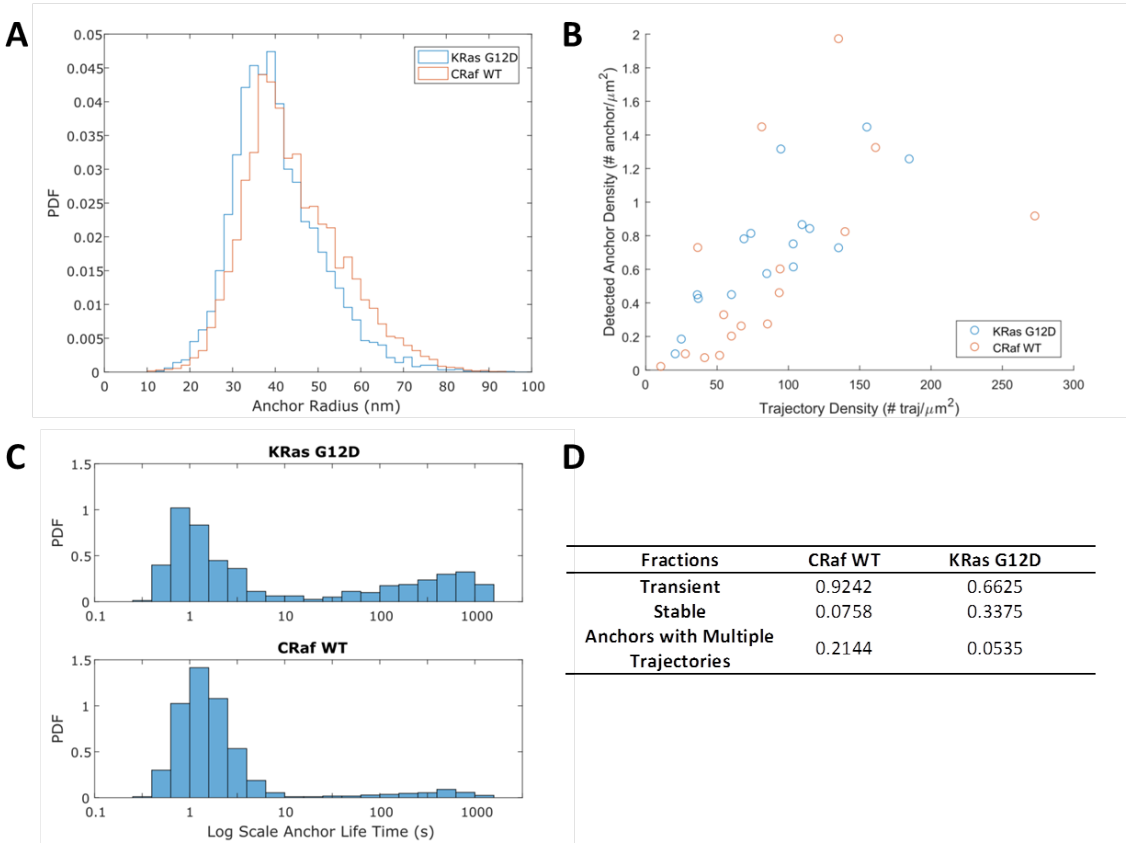

Fractions	CRaf WT	KRas G12D
Transient	0.9242	0.6625
Stable	0.0758	0.3375
Anchors with Multiple Trajectories	0.2144	0.0535

Figure 5.3.4: Ras and Raf anchors have similar properties. The empirical distribution of Ras and Raf anchor sizes (A), detected anchor concentration (B), log transformed anchor life time (C), and anchor life time summary (D) shows that Ras and Raf anchors are not significantly different. In conjunction with results from Figure 5.3.3, this supports the notion that Ras and Raf anchors are the same.

5.4 Discussions/Conclusions

This chapter attempted to address the functional roles of the Ras associated nanodomains (RANDs), as characterized in previous chapters, in Ras membrane biology. Preliminary results suggest that immobile domains, a subset of the RANDs, have potential roles in facilitating Ras cluster formation and signaling. We compared the number of clusters formed between the 2D simulation with and without immobile domains, and as expected, the results showed that immobile domains facilitated Ras cluster formation. In addition, there was virtually no dimer formation with the absence of any mechanism to segregate Ras molecules on the membrane. If immobile domains are responsible for generating Ras clusters and clustering is a requirement for Ras signaling, this would imply that these membrane structures directly control Ras signaling. However, the results discussed in this chapter are limited. While the simulation results show that the presence of RANDs significantly increase Ras clustering at some optimal RAND density, the two-state model is too simplistic and some of the parameters used at the time were unknown and had to be speculated. In the simplified two-state model, the intermediate state was aggregated into the fast state. If the intermediate domains also facilitate Ras multimer formation, the simulation cluster results using the two-state model would be an underestimate of the true cluster fraction. Although the simulation results are encouraging, more work needs to be done using a three-state model with nested immobile and intermediate domains and correct model parameters. However, direct observation of Ras cluster formation in the immobile domains would be preferable. Ras-Ras FRET would be an ideal imaging method to observe both features. This approach is live cell compatible, which allows the identification of immobile domains through Ras diffusion, and is also sensitive to protein-protein interactions.

In line with the hypothesis that the immobile domains are sites of Ras signaling, two color tracking of Ras and Raf show that Raf also interacts with RANDs as well, and that Raf and Ras are often trapped by the same membrane domain. However, there is insufficient data to make any conclusions. One explanation is that RANDs are potential sites of Raf membrane recruitment. However, it is also possible that

Raf is only a cargo that is passively experiencing the membrane environment that Ras is traveling through. Further work needs to be done in order to address whether RANDs are involved in Raf membrane recruitment. Another interesting observation is that membrane domains that trap Raf show short (transient) and long lasting (stable) anchors. The two different anchor domains may have different functional roles. A potential hypothesis to be tested is whether Ras and Raf proteins overlap in the transient or the stable Raf anchor domains. If Ras and Raf preferentially immobilized in the transient anchors, that would indicate that transient anchors have a greater role in Ras-Raf signaling than the stable anchors. One potential explanation besides Ras binding is that some of the Raf anchor domains could represent non-Ras mediated interaction with the membrane.

The compartmentalization of the membrane into nested domains may not only be responsible for dimer and cluster formation, but may also be responsible for segregating pathway specific downstream effectors. Isoform specific activation of different pathways could be achieved by regulating the access of Ras proteins to its downstream effectors through structurally heterogeneous membrane nanodomains with varying preferences for Ras isoforms. The different interaction of Ras tails with different RANDs may affect its interaction with different GEFs and downstream effectors. Therefore, RANDs could act as either transient or stable functional signaling platforms. These membrane nandomains could be formed from many different membrane components, such as lipid rafts, consisting of highly ordered and densely packed structures of sphingolipids and cholesterol, or actin.

Chapter 6

Concluding remarks and future directions

Although it has recently been established that the cell membrane is required for Raf activation [8, 9, 35, 22, 32], its role in Ras biology is still unclear. Therefore, multiple studies have attempted to address this gap in knowledge [22, 23, 24, 25, 26, 38]. From biochemical assays to high resolution imaging, multiple lines of evidence show the importance of Ras cluster formation and membrane segregation as requirements for Ras signaling [35, 32, 36]. Not only does Raf activation require Ras dimers and clusters, Ras membrane segregation is also a critical factor in Ras signaling. More specifically, Ras isoforms occupy distinct membrane domains. Ras GTPases are known to activate over 20 different effectors, but the mechanism of isoform specific activation of Ras pathways is unknown [8]. The main difference between the different Ras isoforms is in their membrane targeting domain, and Ras isoform dependent membrane segregation is a necessary step in downstream signaling. Several pieces of evidence suggest that Ras isoforms have different affinities with different membrane components, such as phosphatidylserine, caveolin, actin, and lipid rafts [8]. In agreement with the literature, we observed differences in H- and KRas localization to two broad categories of membrane structures: actin and vesicle. However, expanding beyond the known literature, our findings suggest that Ras multimer formation is

dependent on the membrane structure, i.e. actin vs. membrane vesicle. We found that dimers tended to colocalize with actin filaments, while large clusters were more likely to be found in vesicles. Hence, this implies that the membrane structures are responsible for Ras multimer formation, where vesicles generate large clusters and actin filaments generate dimers. Therefore, the tendency for HRas to form larger clusters is likely due to its higher affinity for vesicles while KRas preferences for actin could explain the higher fraction of KRas dimers. Our findings support the hypothesis that Ras is organized on the membrane via interactions with multiple membrane components, and the different membrane compartments are responsible for distinct Ras isoform signaling.

Given that Ras resides in the plasma membrane, changes in Ras interaction with membrane components could affect Ras lateral diffusion. Thus, any mechanisms of Ras spatial regulation on the membrane may result in observable changes to its diffusion, which is tied to Ras trafficking, clustering, and signaling. In order to detect and understand the role of the membrane in Ras biology, we used single particle tracking with photoactivated localization microscopy (sptPALM) [51]. We determined that the membrane is composed of at least three distinct membrane regions that interact with Ras and change its mobility. The membrane contains $\sim$70 nm membrane domains nested within a larger domain ($\sim$200 nm) where Ras exhibits immobile and intermediate diffusions, respectively. These nested membrane domains were identified through its effect on Ras mobility, hence termed intermediate and immobile domains. Outside of these domains, Ras freely diffuses, corresponding to fast diffusion. These membrane regions are implicated in Ras endocytosis and trafficking; Ras is removed from the membrane through a subset of the immobile domains while Ras is deposited to the membrane in the fast diffusing region, likely coupled to internalization and recycling. Importantly, both the diffusion and trafficking properties of Ras remain invariant over a broad range of protein expression levels. In addition, we showed that both H and KRas isoforms have a nested membrane organization composed of fast, intermediate and immobile domains but with varying preferences. KRas had significantly more immobile domains than HRas, while the intermediate domain densities were similar between the two isoforms. This further supports the

hypothesis that Ras isoforms have unequal affinities for distinct membrane components which lead to the observed differences in isoform signaling and cluster sizes. Although the molecule identities and the role of these Ras associated nanodomains (RANDs) are not understood, preliminary results show that RANDs have a role in cluster formation and Ras signaling. Our results reveal how membrane organization dictates Ras diffusion and trafficking and offer insight into how Ras signaling may be regulated through spatial mechanisms.

There are a limited number of high resolution tools with the ability to probe protein dynamics in real time. High-throughput SPT is one of the few techniques that can quantify molecular interactions and kinetics in live cells [47, 48, 14, 49, 50, 40]. This powerful technique can measure both spatial and temporal information about the target protein, such that it can detect different diffusion states for a given molecule, and the transient molecular interactions via diffusion state transitions. Further, this approach can infer interaction between a target protein and the membrane through the combination of the molecule's spatial location and its diffusion state. Thus, it becomes possible to infer membrane organization through spatial analysis of diffusion trajectories and their state transitions. Since sptPALM collects individual measurements, it is possible to observe rare, transient events that are missed entirely by other static or bulk measurements. Multi-color sptPALM could even directly observe interplay between Ras and its effectors, or to investigate any membrane protein. sptPALM is a powerful tool that can be used to examine the interplay between the dynamic cell membrane and its resident proteins.

Although sptPALM is an ideal technique for observing membrane proteins in live cells, many factors in the experimental and post-acquisition processing can lead to artifacts. For example, we found that the frame rate, construction of the single particle trajectories, and particle density in each frame were all factors that heavily influenced the diffusion model inference, leading to divergent and non-reproducible results. In order to probe Ras membrane biology, we developed a novel pipeline to rigorously process and analyze single particle tracking movies. By optimizing experimental and image processing parameters based on 2-dimensional diffusion simulations (e.g. frame interval and particle density per frame), we obtained a stable and

reproducible diffusion model by minimizing false trajectory connections. Compared to other studies that attempt to address the same issue [85], our method is a simple and robust solution that does not require extensive refinement of various parameters specific to imaging and experimental conditions.

Given the complexity of the membrane and its role as a key regulator of Ras activation, this study opens the door to understanding exactly how Ras is regulated on the membrane. We have demonstrated that there is a complex interplay between Ras and the membrane components, and that the membrane environment is a dynamic structure that changes over time. Further, Ras signaling pathway is dynamically regulated via multiple feedback loops that control Ras activation via Ras effectors such as GEFs and GAPs. Hence, Ras signaling is a complex process that depends on spatial and temporal elements (i.e. the membrane environment and the transmission of signal from receptor tyrosine kinases (RTKs) and recruitment of downstream effectors, respectively). Given that both spatial and temporal information are necessary to fully understand Ras regulation, the work here shows that live cell single particle tracking is an ideal technique to answer the remaining questions in the field.

Our findings prompt new questions. We found that there are three different regions of the membrane, and that the immobile and intermediate domains may be composed of multiple membrane structures. Of note, our data implies that the immobile and intermediate domains are composed of at least two different membrane components, whereby the Ras tail facilitates the interaction with these membrane structures. Further, preliminary data indicate that immobile domains facilitate Ras cluster formation. However, the direct observations of these findings are lacking. We can now address these hypotheses through a combination of live cell compatible imaging approaches which enable direct observations of the immobile and intermediate domains and locations of multimer formation. For example, FRET can be used to quantify protein interactions, while multi-color imaging can simultaneously observe multiple membrane components and proteins involved in Ras signaling pathways. In addition, these imaging approaches will enable tagging of multiple protein and membrane components. Simultaneous imaging of multiple tags can be used to answer questions such as the molecular composition of the immobile and intermedi-

ate domains. This can be extended to investigate whether the immobile domains are Ras signaling platforms by tagging upstream and downstream Ras effectors, such as RTKs and Rafs. Although we have discovered the existence of the intermediate domain, its function in Ras membrane biology and its composition are unknown. Since the larger intermediate domain generally contains immobile domains, the intermediate domains may potentially act as transition zones that contain the molecular machinery necessary for the formation of immobile domains.

Particle based simulations in Chapter 5 provided some evidence that RANDs facilitated Ras dimers, a necessary step for Ras signaling. Although the preliminary simulation results seem promising, the simulations were too simplistic and did not entirely reflect all of the experimental findings in Chapter 3. However, spatial and particle based simulations are highly valuable in exploring some of the mechanistic details of Ras membrane regulation that cannot be tested experimentally. Therefore, to accurately determine the role of RANDs in Ras signaling, the simulation needs to be expanded to include both immobile and intermediate domains with transient and stable life times, as well as the endocytosis and trafficking to and from the membrane. A more accurate simulation can be used to determine the function of the intermediate domains by comparing the rate of dimer or cluster formation in intermediate and immobile domains. Further, the addition of life times to the domains will allow further exploration of the role of transient and stable immobile domains in Ras cluster formation and signaling. Incorporation of downstream factors, such as Raf, will be helpful for determining whether intermediate domains may play a role in recruiting Raf to the membrane.

This research was only enabled through tightly coupled experimental and computational approaches. One of the main challenges of single particle tracking experiments is the lack of ground truth when assigning trajectories to individual particles. Since the data is unlabeled, it is difficult to determine the accuracy of the data processing pipeline to construct finalized trajectories from the movies. We were able to solve this problem through the use of simulations to generate data with known diffusion parameters. Simulated datasets allowed us to test and refine both the experimental parameters, such as the frame rate and the maximum particle density

per frame, and the trajectory construction method. Our combined approach was highly valuable since it allowed us to draw conclusions from otherwise unlabeled data. Therefore, we recommend the use of simulations to validate data analysis for similar future work. In addition to informing the experiment, simulations were utilized to test hypothesis generated by the experiment. Simulations results shown in Chapter 5 provided some evidence that RANDs facilitate Ras dimer formation. Overall, this tightly coupled experimental and computational research program enabled multiple orthogonal approaches where simulations and experiments informed each other.

The work presented here focuses on Ras, but there are many other signaling proteins that reside on the plasma membrane, such as RTKs. The different membrane environments that Ras molecules experience are not unique to Ras; the membrane organization that governs Ras must also impact other membrane proteins. Consequently, the importance of the membrane features in Ras signaling may not be a mechanism that is specific only to Ras, but for other signaling proteins that reside on the membrane as well. Although the RANDs discovered here may be unique to Ras, membrane segregation is likely a general mechanism that governs all membrane proteins. Other studies have demonstrated the role of the plasma membrane through endocytosis and subsequent lysosomal receptor degradation and endosomal recycling in maintaining and propagating a signal [65]. Further, protein clustering is emerging to be a common requirement for signaling among membrane proteins [65]. Thus, this is an additional mechanism for further regulation ofsignaling proteins. Therefore, plasma membrane can govern membrane proteins through various ways. Consequently, being able to understand the dynamic and transient interplay between the cellular membrane and its resident proteins is going to be a critical step to fully understanding membrane protein signaling.

Bibliography

[1] H. R. Bourne, D. A. Sanders, and F. McCormick, "The GTPase superfamily: a conserved switch for diverse cell functions," *Nature*, vol. 348, pp. 125–132, Nov 1990.

[2] A. G. Stephen, D. Esposito, R. K. Bagni, and F. McCormick, "Dragging ras back in the ring," *Cancer Cell*, vol. 25, pp. 272–281, Mar 2014.

[3] A. A. Samatar and P. I. Poulikakos, "Targeting ras–erk signalling in cancer: promises and challenges," *Nature Reviews Drug Discovery*, vol. 13, pp. 928–942, Dec 2014.

[4] A. E. Karnoub and R. A. Weinberg, "Ras oncogenes: split personalities," *Nature Reviews Molecular Cell Biology*, vol. 9, pp. 517–531, Jul 2008.

[5] A. S. Dhillon, S. Hagan, O. Rath, and W. Kolch, "MAP kinase signalling pathways in cancer," *Oncogene*, vol. 26, pp. 3279–3290, May 2007.

[6] A. M. Rojas, G. Fuentes, A. Rausell, and A. Valencia, "The ras protein superfamily: Evolutionary tree and role of conserved amino acids," *The Journal of Cell Biology*, vol. 196, pp. 189–201, Jan 2012.

[7] K. Wennerberg, "The ras superfamily at a glance," *Journal of Cell Science*, vol. 118, pp. 843–846, Feb 2005.

[8] T. S. Chavan, S. Muratcioglu, R. Marszalek, H. Jang, O. Keskin, A. Gursoy, R. Nussinov, and V. Gaponenko, "Plasma membrane regulates ras signaling networks," *Cellular Logistics*, vol. 5, Dec 2015.

[9] J. F. Hancock, "Ras proteins: different signals from different locations," *Nature Reviews Molecular Cell Biology*, vol. 4, pp. 373–385, May 2003.

[10] J. Yan, S. Roy, A. Apolloni, A. Lane, and J. F. Hancock, "Ras isoforms vary in their ability to activate raf-1 and phosphoinositide 3-kinase," *Journal of Biological Chemistry*, vol. 273, pp. 24052–24056, Sep 1998.

[11] L. Brunsveld, H. Waldmann, and D. Huster, "Membrane binding of lipidated ras peptides and proteins — the structural point of view," *Biochimica et Biophysica Acta (BBA) - Biomembranes*, vol. 1788, pp. 273–288, Jan 2009.

[12] G. W. Reuther and C. J. Der, "The ras branch of small gtpases: Ras family members don't fall far from the tree," *Current Opinion in Cell Biology*, vol. 12, pp. 157–165, Apr 2000.

[13] S. Eisenberg and Y. I. Henis, "Interactions of Ras proteins with the plasma membrane and their roles in signaling," *Cellular Signalling*, vol. 20, pp. 31–39, Jan 2008.

[14] A. Kusumi, C. Nakada, K. Ritchie, K. Murase, K. Suzuki, H. Murakoshi, R. S. Kasai, J. Kondo, and T. Fujiwara, "Paradigm shift of the plasma membrane concept from the two-dimensional continuum fluid to the partitioned fluid: High-speed single-molecule tracking of membrane molecules," *Annual Review of Biophysics and Biomolecular Structure*, vol. 34, pp. 351–378, Feb 2005.

[15] K. Simons and E. Ikonen, "Functional rafts in cell membranes," *Nature*, vol. 387, no. 6633, pp. 569–572, 1997.

[16] A. J. Laude and I. A. Prior, "Plasma membrane microdomains: Organization, function and trafficking (review)," *Molecular Membrane Biology*, vol. 21, pp. 193–205, Feb 2004.

[17] D. Murray, N. Ben-Tal, B. Honig, and S. Mclaughlin, "Electrostatic interaction of myristoylated proteins with membranes: simple physics, complicated biology," *Structure*, vol. 5, pp. 985–989, Aug 1997.

[18] J. G. Kay, M. Koivusalo, X. Ma, T. Wohland, and S. Grinstein, "Phosphatidylserine dynamics in cellular membranes," *Molecular Biology of the Cell*, vol. 23, pp. 2198–2212, Apr 2012.

[19] T. Fujiwara, K. Ritchie, H. Murakoshi, K. Jacobson, and A. Kusumi, "Phospholipids undergo hop diffusion in compartmentalized cell membrane," *The Journal of Cell Biology*, vol. 157, pp. 1071–1082, Jun 2002.

[20] K. Murase, T. Fujiwara, Y. Umemura, K. Suzuki, R. Iino, H. Yamashita, M. Saito, H. Murakoshi, K. Ritchie, A. Kusumi, and et al., "Ultrafine membrane compartments for molecular diffusion as revealed by single molecule techniques," *Biophysical Journal*, vol. 86, pp. 4075–4093, Jun 2004.

[21] K. Simons and W. L. Vaz, "Model systems, lipid rafts, and cell membranes," *Annual Review of Biophysics and Biomolecular Structure*, vol. 33, pp. 269–295, Jun 2004.

[22] I. A. Prior and J. F. Hancock, "Ras trafficking, localization and compartmentalized signalling," *Seminars in Cell & Developmental Biology*, vol. 23, pp. 145–153, Apr 2012.

[23] I. A. Prior, C. Muncke, R. G. Parton, and J. F. Hancock, "Direct visualization of ras proteins in spatially distinct cell surface microdomains," *The Journal of Cell Biology*, vol. 160, pp. 165–170, Jan 2003.

[24] N. Ariotti, M. Fernandez-Rojo, Y. Zhou, M. Hill, T. Rodkey, K. Inder, L. Tanner, M. Wenk, J. Hancock, R. Parton, and et al., "Caveolae regulate the nanoscale organization of the plasma membrane to remotely control ras signaling," *The Journal of General Physiology*, vol. 143, Feb 2014.

[25] S. J. Plowman, C. Muncke, R. G. Parton, and J. F. Hancock, "H-ras, K-ras, and inner plasma membrane raft proteins operate in nanoclusters with differential dependence on the actin cytoskeleton," *Proceedings of the National Academy of Sciences*, vol. 102, pp. 15500–15505, Oct 2005.

[26] I. A. Prior, A. Harding, J. Yan, J. Sluimer, R. G. Parton, and J. F. Hancock, "GTP-dependent segregation of H-ras from lipid rafts is required for biological activity," *Nature Cell Biology*, vol. 3, pp. 368–375, Mar 2001.

[27] Y. Zhou, C.-O. Wong, K.-J. Cho, D. V. D. Hoeven, H. Liang, D. P. Thakur, J. Luo, M. Babic, K. E. Zinsmaier, M. X. Zhu, and et al., "Membrane potential modulates plasma membrane phospholipid dynamics and k-ras signaling," *Science*, vol. 349, pp. 873–876, Aug 2015.

[28] Y. Zhou, P. Prakash, H. Liang, K.-J. Cho, A. A. Gorfe, and J. F. Hancock, "Lipid-sorting specificity encoded in K-Ras membrane anchor regulates signal output," *Cell*, vol. 168, Jan 2017.

[29] T. Yeung, G. E. Gilbert, J. Shi, J. Silvius, A. Kapus, and S. Grinstein, "Membrane phosphatidylserine regulates surface charge and protein localization," *Science*, vol. 319, pp. 210–213, Jan 2008.

[30] M. F. Garcia-Parajo, A. Cambi, J. A. Torreno-Pina, N. Thompson, and K. Jacobson, "Nanoclustering as a dominant feature of plasma membrane organization," *Journal of Cell Science*, vol. 127, pp. 4995–5005, Dec 2014.

[31] J. Schlessinger, "Ligand-induced, receptor-mediated dimerization and activation of egf receptor," *Cell*, vol. 110, pp. 669–672, Sep 2002.

[32] T. Tian, A. Harding, K. Inder, S. Plowman, R. G. Parton, and J. F. Hancock, "Plasma membrane nanoswitches generate high-fidelity ras signal transduction," *Nature Cell Biology*, vol. 9, pp. 905–914, Jul 2007.

[33] R. Shalom-Feuerstein, S. J. Plowman, B. Rotblat, N. Ariotti, T. Tian, J. F. Hancock, and Y. Kloog, "K-Ras nanoclustering is subverted by overexpression of the scaffold protein galectin-3," *Cancer Research*, vol. 68, pp. 6608–6616, Aug 2008.

[34] X. Nan, T. M. Tamgüney, E. A. Collisson, L.-J. Lin, C. Pitt, J. Galeas, S. Lewis, J. W. Gray, F. McCormick, S. Chu, and et al., "Ras-GTP dimers activate

the mitogen-activated protein kinase (MAPK) pathway," *Proceedings of the National Academy of Sciences*, vol. 112, pp. 7996–8001, Jun 2015.

[35] K. Inouye, S. Mizutani, H. Koide, and Y. Kaziro, "Formation of the ras dimer is essential for raf-1 activation," *Journal of Biological Chemistry*, vol. 275, pp. 3737–3740, Feb 2000.

[36] R. Spencer-Smith, A. Koide, Y. Zhou, R. R. Eguchi, F. Sha, P. Gajwani, D. Santana, A. Gupta, M. Jacobs, E. Herrero-Garcia, and et al., "Inhibition of RAS function through targeting an allosteric regulatory site," *Nature Chemical Biology*, vol. 13, pp. 62–68, Nov 2016.

[37] A. J. Koster and J. Klumperman, "Electron microscopy in cell biology: integrating structure and function.," *Nature reviews. Molecular cell biology*, vol. Suppl, pp. SS6–10, 2003.

[38] I. A. Prior, R. G. Parton, and J. F. Hancock, "Observing cell surface signaling domains using electron microscopy," *Science Signaling*, vol. 2003, Apr 2003.

[39] L. Ying, W. Wang, S. Wang, F. Zhang, S. Zhang, and N. Tao, "How does fluorescent labeling affect the binding kinetics of proteins with intact cells?," *Biosensors & bioelectronics*, 2015.

[40] A. von Diezmann, Y. Shechtman, and W. E. Moerner, "Three-dimensional localization of single molecules for super-resolution imaging and single-particle tracking," *Chemical reviews*, Jun 2017.

[41] R. B. Sekar and A. Periasamy, "Fluorescence resonance energy transfer (fret) microscopy imaging of live cell protein localizations," *The Journal of Cell Biology*, vol. 160, pp. 629–633, Mar 2003.

[42] M. J. Rust, M. Bates, and X. Zhuang, "Sub-diffraction-limit imaging by stochastic optical reconstruction microscopy (storm)," *Nature Methods*, vol. 3, pp. 793–796, Aug 2006.

[43] E. Betzig, G. H. Patterson, R. Sougrat, O. W. Lindwasser, S. Olenych, J. S. Bonifacino, M. W. Davidson, J. Lippincott-Schwartz, and H. F. Hess, "Imaging intracellular fluorescent proteins at nanometer resolution," *Science*, vol. 313, pp. 1642–1645, Sep 2006.

[44] M. G. L. Gustafsson, "Surpassing the lateral resolution limit by a factor of two using structured illumination microscopy. short communication," *Journal of Microscopy*, vol. 198, pp. 82–87, Dec 2001.

[45] S. W. Hell and J. Wichmann, "Breaking the diffraction resolution limit by stimulated emission: stimulated-emission-depletion fluorescence microscopy," *Optics Letters*, vol. 19, no. 11, p. 780, 1994.

[46] R. Jungmann, M. S. Avendaño, J. B. Woehrstein, M. Dai, W. M. Shih, and P. Yin, "Multiplexed 3d cellular super-resolution imaging with dna-paint and exchange-paint," *Nature Methods*, vol. 11, pp. 313–318, Feb 2014.

[47] T. Schmidt, G. J. Schutz, W. Baumgartner, H. J. Gruber, and H. Schindler, "Imaging of single molecule diffusion.," *Proceedings of the National Academy of Sciences*, vol. 93, pp. 2926–2929, Apr 1996.

[48] M. J. Saxton and K. Jacobson, "Single-particle tracking: Applications to membrane dynamics," *Annual Review of Biophysics and Biomolecular Structure*, vol. 26, no. 1, pp. 373–399, 1997.

[49] S. T. Low-Nam, K. A. Lidke, P. J. Cutler, R. C. Roovers, P. M. P. V. B. E. Henegouwen, B. S. Wilson, and D. S. Lidke, "Erbb1 dimerization is promoted by domain co-confinement and stabilized by ligand binding," *Nature Structural & Molecular Biology*, vol. 18, pp. 1244–1249, Oct 2011.

[50] C. Manzo and M. F. Garcia-Parajo, "A review of progress in single particle tracking: from methods to biophysical insights," *Reports on Progress in Physics*, vol. 78, p. 124601, Oct 2015.

[51] S. Manley, J. M. Gillette, G. H. Patterson, H. Shroff, H. F. Hess, E. Betzig, and J. Lippincott-Schwartz, "High-density mapping of single-molecule trajectories with photoactivated localization microscopy," *Nature Methods*, vol. 5, pp. 155–157, Jan 2008.

[52] D. M. Zuckerman, "Physical lens on the cell."

[53] F. Yang, T.-Y. Chen, Ł. Krzemiński, A. G. Santiago, W. Jung, and P. Chen, "Single-molecule dynamics of the molecular chaperone trigger factor in living cells," *Molecular Microbiology*, vol. 102, pp. 992–1003, Sep 2016.

[54] G. Schütz, H. Schindler, and T. Schmidt, "Single-molecule microscopy on model membranes reveals anomalous diffusion," *Biophysical Journal*, vol. 73, pp. 1073–1080, Aug 1997.

[55] M. Vrljic, S. Y. Nishimura, S. Brasselet, W. Moerner, and H. M. Mcconnell, "Translational diffusion of individual class ii mhc membrane proteinsin cells," *Biophysical Journal*, vol. 83, pp. 2681–2692, Nov 2002.

[56] P. J. Bosch, J. S. Kanger, and V. Subramaniam, "Classification of dynamical diffusion states in single molecule tracking microscopy," *Biophysical Journal*, vol. 107, pp. 588–598, Aug 2014.

[57] R. Castro, "The empirical distribution function and the histogram," *Lecture Notes, 2WS17-Advanced Statistics. Department of Mathematics, Eindhoven University of Technology*, vol. 4, 2015.

[58] F. Persson, M. Lindén, C. Unoson, and J. Elf, "Extracting intracellular diffusive states and transition rates from single-molecule tracking data," *Nature Methods*, vol. 10, pp. 265–269, Feb 2013.

[59] C. M. BISHOP, *PATTERN RECOGNITION AND MACHINE LEARNING*. SPRINGER-VERLAG NEW YORK, 2016.

[60] P. H. Lommerse, K. Vastenhoud, N. J. Pirinen, A. I. Magee, H. P. Spaink, and T. Schmidt, "Single-molecule diffusion reveals similar mobility for the lck, h-ras, and k-ras membrane anchors," *Biophysical Journal*, vol. 91, pp. 1090–1097, Aug 2006.

[61] H. Murakoshi, R. Iino, T. Kobayashi, T. Fujiwara, C. Ohshima, A. Yoshimura, and A. Kusumi, "Single-molecule imaging analysis of ras activation in living cells," *Proceedings of the National Academy of Sciences*, vol. 101, pp. 7317–7322, May 2004.

[62] P. H. Lommerse, G. A. Blab, L. Cognet, G. S. Harms, B. E. Snaar-Jagalska, H. P. Spaink, and T. Schmidt, "Single-molecule imaging of the h-ras membrane-anchor reveals domains in the cytoplasmic leaflet of the cell membrane," *Biophysical Journal*, vol. 86, pp. 609–616, Jan 2004.

[63] A. S. Hansen, M. Woringer, J. B. Grimm, L. D. Lavis, R. Tjian, and X. Darzacq, "Robust model-based analysis of single-particle tracking experiments with spot-on," *eLife*, vol. 7, Jan 2018.

[64] Y. Lee, C. Phelps, T. Huang, B. Mostofian, L. Wu, Y. Zhang, K. Tao, Y. H. Chang, P. J. Stork, J. W. Gray, D. M. Zuckerman, and X. Nan, "High-throughput single-particle tracking reveals nested membrane domains that dictate KRasG12D diffusion and trafficking," *eLife*, 2019.

[65] H. E. Grecco, M. Schmick, and P. I. Bastiaens, "Signaling from the living plasma membrane," *Cell*, vol. 144, pp. 897–909, Mar 2011.

[66] S. Staubach and F.-G. Hanisch, "Lipid rafts: signaling and sorting platforms of cells and their roles in cancer," *Expert Review of Proteomics*, vol. 8, no. 2, pp. 263–277, 2011.

[67] K. Simons and D. Toomre, "Lipid rafts and signal transduction," *Nature Reviews Molecular Cell Biology*, vol. 1, pp. 31–39, Oct 2000.

[68] R. Varma and S. Mayor, "Gpi-anchored proteins are organized in submicron domains at the cell surface," *Nature*, vol. 394, pp. 798–801, Aug 1998.

[69] M. Schmick and P. I. Bastiaens, "The interdependence of membrane shape and cellular signal processing," *Cell*, vol. 156, pp. 1132–1138, Mar 2014.

[70] Y. Zhou and J. F. Hancock, "Ras nanoclusters: Versatile lipid-based signaling platforms," *Biochimica et Biophysica Acta (BBA) - Molecular Cell Research*, vol. 1853, pp. 841–849, Apr 2015.

[71] D. Abankwa, A. A. Gorfe, K. Inder, and J. F. Hancock, "Ras membrane orientation and nanodomain localization generate isoform diversity," *Proceedings of the National Academy of Sciences*, vol. 107, pp. 1130–1135, Jan 2010.

[72] D. K. Simanshu, D. V. Nissley, and F. Mccormick, "Ras proteins and their regulators in human disease," *Cell*, vol. 170, pp. 17–33, Jun 2017.

[73] A. D. Cox and C. J. Der, "Ras history," *Small GTPases*, vol. 1, pp. 2–27, Jul 2010.

[74] J. Güldenhaupt, T. Rudack, P. Bachler, D. Mann, G. Triola, H. Waldmann, C. Kötting, and K. Gerwert, "N-ras forms dimers at popc membranes," *Biophysical Journal*, vol. 103, pp. 1585–1593, Oct 2012.

[75] C. Ambrogio, J. Köhler, Z.-W. Zhou, H. Wang, R. Paranal, J. Li, M. Capelletti, C. Caffarra, S. Li, Q. Lv, and et al., "Kras dimerization impacts mek inhibitor sensitivity and oncogenic activity of mutant kras," *Cell*, vol. 172, Feb 2018.

[76] J. K. Chung, Y. K. Lee, J.-P. Denson, W. K. Gillette, S. Alvarez, A. G. Stephen, and J. T. Groves, "K-ras4b remains monomeric on membranes over a wide range of surface densities and lipid compositions," *Biophysical Journal*, vol. 114, pp. 137–145, Jan 2018.

[77] L. Belanis, S. J. Plowman, B. Rotblat, J. F. Hancock, and Y. Kloog, "Galectin-1 is a novel structural component and a major regulator of h-ras nanoclusters," *Molecular Biology of the Cell*, vol. 19, pp. 1404–1414, Apr 2008.

[78] A. Benke, N. Olivier, J. GunzenhGäuser, and S. Manley, "Multicolor single molecule tracking of stochastically active synthetic dyes," *Nano Letters*, vol. 12, pp. 2619–2624, Apr 2012.

[79] T. Huang, C. Phelps, J. Wang, L.-J. Lin, A. Bittel, Z. Scott, S. Jacques, S. L. Gibbs, J. W. Gray, X. Nan, and et al., "Simultaneous multicolor single-molecule tracking with single-laser excitation via spectral imaging," *Biophysical Journal*, vol. 114, pp. 301–310, Jan 2018.

[80] S. Basu, L.-M. Needham, D. Lando, E. J. R. Taylor, K. J. Wohlfahrt, D. Shah, W. Boucher, Y. L. Tan, L. E. Bates, O. Tkachenko, and et al., "Fret-enhanced photostability allows improved single-molecule tracking of proteins and protein complexes in live mammalian cells," *Nature Communications*, vol. 9, Jun 2018.

[81] B. P. English and R. H. Singer, "A three-camera imaging microscope for high-speed single-molecule tracking and super-resolution imaging in living cells," *Biosensing and Nanomedicine VIII*, Aug 2015.

[82] P. J. Cutler, M. D. Malik, S. Liu, J. M. Byars, D. S. Lidke, and K. A. Lidke, "Multi-color quantum dot tracking using a high-speed hyperspectral line-scanning microscope," *PLoS ONE*, vol. 8, May 2013.

[83] Z. Liu, L. D. Lavis, and E. Betzig, "Imaging live-cell dynamics and structure at the single-molecule level," *Molecular Cell*, vol. 58, pp. 644–659, May 2015.

[84] K. Jaqaman, D. Loerke, M. Mettlen, H. Kuwata, S. Grinstein, S. L. Schmid, and G. Danuser, "Robust single-particle tracking in live-cell time-lapse sequences," *Nature Methods*, vol. 5, pp. 695–702, Jul 2008.

[85] N. Chenouard, I. Smal, F. D. Chaumont, M. Maška, I. F. Sbalzarini, Y. Gong, J. Cardinale, C. Carthel, S. Coraluppi, M. Winter, and et al., "Objective comparison of particle tracking methods," *Nature Methods*, vol. 11, pp. 281–289, Jan 2014.

[86] H. Shen, L. J. Tauzin, R. Baiyasi, W. Wang, N. Moringo, B. Shuang, and C. F. Landes, "Single particle tracking: From theory to biophysical applications," *Chemical Reviews*, vol. 117, pp. 7331–7376, May 2017.

[87] N. Monnier, Z. Barry, H. Y. Park, K.-C. Su, Z. Katz, B. P. English, A. Dey, K. Pan, I. M. Cheeseman, R. H. Singer, and et al., "Inferring transient particle transport dynamics in live cells," *Nature Methods*, vol. 12, pp. 838–840, Jul 2015.

[88] Y. Ito, K. Sakata-Sogawa, and M. Tokunaga, "Multi-color single-molecule tracking and subtrajectory analysis for quantification of spatiotemporal dynamics and kinetics upon t cell activation," *Scientific Reports*, vol. 7, Aug 2017.

[89] M. Lindén and J. Elf, "Variational algorithms for analyzing noisy multistate diffusion trajectories," *Biophysical Journal*, vol. 115, pp. 276–282, Jul 2018.

[90] J. M. Newby, A. M. Schaefer, P. T. Lee, M. G. Forest, and S. K. Lai, "Convolutional neural networks automate detection for tracking of submicron-scale particles in 2d and 3d," *Proceedings of the National Academy of Sciences*, vol. 115, pp. 9026–9031, Aug 2018.

[91] F. V. Subach, G. H. Patterson, S. Manley, J. M. Gillette, J. Lippincott-Schwartz, and V. V. Verkhusha, "Photoactivatable mcherry for high-resolution two-color fluorescence microscopy," *Nature Methods*, vol. 6, pp. 153–159, Jan 2009.

[92] M. Schmick, N. Vartak, B. Papke, M. Kovacevic, D. C. Truxius, L. Rossmannek, and P. I. Bastiaens, "Kras localizes to the plasma membrane by spatial cycles of solubilization, trapping and vesicular transport," *Cell*, vol. 157, pp. 459–471, Apr 2014.

[93] M. Schmick, A. Kraemer, and P. I. Bastiaens, "Ras moves to stay in place," *Trends in Cell Biology*, vol. 25, pp. 190–197, Apr 2015.

[94] K. Gowrishankar, S. Ghosh, S. Saha, R. C., S. Mayor, and M. Rao, "Active remodeling of cortical actin regulates spatiotemporal organization of cell surface molecules," *Cell*, vol. 149, pp. 1353–1367, Jun 2012.

[95] R. Nussinov, C.-J. Tsai, and H. Jang, "Is nanoclustering essential for all oncogenic kras pathways? can it explain why wild-type kras can inhibit its oncogenic variant?," *Seminars in Cancer Biology*, vol. 54, pp. 114–120, Feb 2019.

[96] K.-J. Cho, D. V. D. Hoeven, Y. Zhou, M. Maekawa, X. Ma, W. Chen, G. D. Fairn, and J. F. Hancock, "Inhibition of acid sphingomyelinase depletes cellular phosphatidylserine and mislocalizes k-ras from the plasma membrane," *Molecular and Cellular Biology*, Nov 2015.

[97] S. Roy, B. Wyse, and J. F. Hancock, "H-Ras signaling and K-Ras signaling are differentially dependent on endocytosis," *Molecular and Cellular Biology*, vol. 22, pp. 5128–5140, Jul 2002.

[98] O. Rocks, "An acylation cycle regulates localization and activity of palmitoylated ras isoforms," *Science*, vol. 307, pp. 1746–1752, Mar 2005.

[99] A. Lu, F. Tebar, B. Alvarez-Moya, C. López-Alcalá, M. Calvo, C. Enrich, N. Agell, T. Nakamura, M. Matsuda, O. Bachs, and et al., "A clathrin-dependent pathway leads to KRas signaling on late endosomes en route to lysosomes," *The Journal of Cell Biology*, vol. 184, pp. 863–879, Mar 2009.

[100] S. Mayor, R. G. Parton, and J. G. Donaldson, "Clathrin-independent pathways of endocytosis," *Cold Spring Harbor Perspectives in Biology*, vol. 6, Jun 2014.

[101] M. Kaksonen, C. P. Toret, and D. G. Drubin, "A modular design for the clathrin- and actin-mediated endocytosis machinery," *Cell*, vol. 123, pp. 305–320, Oct 2005.

[102] P. Sharma, R. Varma, R. Sarasij, Ira, K. Gousset, G. Krishnamoorthy, M. Rao, and S. Mayor, "Nanoscale organization of multiple gpi-anchored proteins in living cell membranes," *Cell*, vol. 116, pp. 577–589, Feb 2004.

[103] Y. Zhang, Y. Lee, L. Wu, K. Tao, B. Mostofian, D. Zuckerman, X. Song, Y. H. Chang, and X. Nan, "Diverse plasma membrane compartments regulate isoform-specific ras multimer formation and signaling," *Manuscript In Preparation*, 2019.

[104] I. Gaidarov, F. Santini, R. A. Warren, and J. H. Keen, "Spatial control of coated-pit dynamics in living cells," *Nature Cell Biology*, vol. 1, pp. 1–7, May 1999.

[105] G. Preta, J. G. Cronin, and I. M. Sheldon, "Dynasore - not just a dynamin inhibitor," *Cell Communication and Signaling*, vol. 13, Apr 2015.

[106] R. J. Park, H. Shen, L. Liu, X. Liu, S. M. Ferguson, and P. D. Camilli, "Dynamin triple knockout cells reveal off target effects of commonly used dynamin inhibitors," *Journal of Cell Science*, vol. 126, pp. 5305–5312, Nov 2013.